Measurement of Elliptic Flow in p+Au Collisions at $\sqrt{s_{_{NN}}}$ = 200 GeV using the PHENIX Detector at RHIC

by

Theodore Koblesky

B.S., University of Illinois, 2011

A thesis submitted to the

Faculty of the Graduate School of the

University of Colorado in partial fulfillment

of the requirements for the degree of

Doctor of Philosophy

Department of Physics

2017

This thesis entitled:
Measurement of Elliptic Flow in p+Au Collisions at $\sqrt{s_{NN}} = 200$ GeV using the PHENIX Detector at RHIC
written by Theodore Koblesky
has been approved for the Department of Physics

Professor James Nagle

Prof. Standin

Ms. Standin

Date

The final copy of this thesis has been examined by the signatories, and we find that both the content and the form meet acceptable presentation standards of scholarly work in the above mentioned discipline.

Koblesky, Theodore (Ph.D., High Energy Nuclear Physics)

Measurement of Elliptic Flow in p+Au Collisions at $\sqrt{s_{NN}} = 200$ GeV using the PHENIX Detector at RHIC

Thesis directed by Professor James Nagle

Quark Gluon Plasma (QGP), a hot and dense state of matter in which quarks are not confined inside hadrons, is thought to be the same as the universe approximately one microsecond after the big bang. In Au+Au collisions at $\sqrt{s_{NN}} = 200$ GeV at the Relativistic Heavy Ion Collider (RHIC) and Pb+Pb collisions at $\sqrt{s_{NN}} = 2.76$ TeV at the Large Hadron Collider (LHC), QGP has been discovered to have unique properties, such as its opacity to color charges and the fact it behaves like a near-perfect fluid. Collective behavior in the form of a substantial elliptical azimuthal anisotropy (v_2) in the momentum distribution of final state particles has been observed, indicating a strongly-coupled, hydrodynamically flowing medium. Recently, features of collectivity have been detected in high-multiplicity, small collision systems thought to be too small to produce QGP, such as ^{3}He+Au and d+Au at $\sqrt{s_{NN}} = 200$ GeV, p+Pb at $\sqrt{s_{NN}} = 5$ TeV, and in p+p at $\sqrt{s} = 13$ TeV events. In order to constrain models seeking to describe this phenomena, collision systems with distinct initial collision geometries were run at RHIC: ^{3}He+Au for triangular geometry, d+Au for elliptical geometry, and p+Au for circular geometry. This thesis is the completion of that set of three measurements, by measuring v_2 in the p+Au. Comparisons of v_2 in the three collision systems and various theoretical models are made.

Dedication

Acknowledgements

People

Contents

Tables

Table

Figures

Figure

Chapter 1

Physics Overview

In order to give the proper context for the measurement shown in this thesis, an overview of the physical theory relevant to the measurement is given in this chapter. We start with the SM (Standard Model of particle physics), narrow the focus down to QCD (Quantum Chromodynamics), and then narrow the focus even more to a specific state of matter governed by QCD known as the QGP (Quark Gluon Plasma). Properties of the QGP are discussed including energy loss and elliptic flow. A more comprehensive discussion on the topic of elliptic flow and small collision systems will be presented in Chapter 2.

1.1 The Standard Model

The SM is the best understanding of the fundamental building blocks reality and how they interact. The SM as we know it today has evolved over many years, including the unification of the electromagnetic and weak forces in the late 1960s [**?**]. The present day SM includes four fundamental forces, listed in Table 1.1, and the fundamental particles, listed in Figure 1.1.

Table 1.1: All four of the fundamental forces and the effective strengths of each relative to gravity. Gravity is not covered by the SM but is included for completeness.

Force	Current Theory	Relative Strength	Range [m]	Force Carriers
strong	Quantum Chromodynamics (QCD)	10^{41}	10^{-15}	gluon (g)
electromagnetic	Quantum Electrodynamics (QED)	10^{38}	∞	photon (γ)
weak	Electroweak	10^{25}	10^{-18}	Z^0,$W^{+/-}$
gravity	General Relativity	1	∞	graviton (hypothetical)

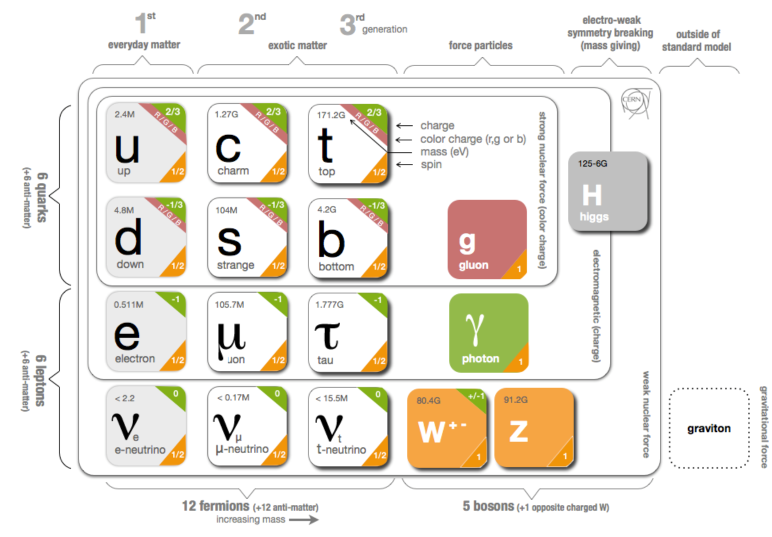

Figure 1.1: The fundamental particles of the SM arranged to highlight flavor (horizontal) and charge (vertical) patterns among the particles. These are thought to be the smallest discrete pieces of matter which make up everything else in the universe [13].

The SM has the capability of making quantifiable predictions which have been shown to be in agreement with experimental measurements to many decimal places. The SM has endured decades of meticulous experimental testing without the need for major revisions, a notable exception being neutrino oscillations. The mathematical framework underpinning the SM is formally known as QFT (Quantum Field Theory). which combines the continuous nature of field physics with the discrete nature of quantum physics. The fundamental symmetries of the SM are given by the combination of the $SU(3) \times SU(2) \times U(1)$ groups as defined in group theory. Each symmetry group represents the symmetry of each of the fundamental forces in the SM such that $SU(3)$, $SU(2)$, and $U(1)$ represent the strong, weak, and electromagnetic forces respectively. As shown in table 1.1, each of the fundamental forces has a quantized theory associated with it. The electromagnetic and weak forces combine into a single theory at high energy, known as the Electroweak Theory. No similar theory which has been experimentally verified has combined strong and electroweak upon writing of this thesis.

Any given interaction described by the SM starts with an initial set of particles, a series of interactions between those particles (which is represented by an exchange of virtual particles), and then a set of final state output particles. Experimentally, the only information available to the experimenter is the list of input particles and output particles. The in-between step of the interaction of the particles is where QFT is used. Theoretical physicists use QFT to calculate the probabilities of each possible interaction diagram given a set of input particles or a set of output particles or both. To complicate things, there are infinite possible interaction diagrams for any given set of inputs and outputs; however, there are always leading diagrams which have the highest probability of occurring. Generally the simpler the interaction diagram, the higher the probability.

In order to make predictions about physical systems dominated by the strong force, like the heavy ion collision systems studied in this thesis, we turn to QCD.

1.1.1 Quantum Chromodynamics

Of the fundamental particles which make up the SM, the only ones which interact through the strong force are quarks and gluons. These particles have a unique quantum number named color charge which can be one of three values referred to as red (r), green (g), and blue (b), in an analogy to three colors commonly used to form the basis of light in the visible spectrum. Like the electric charge in QED, each color has a negative value referred to as anti-red ($\bar{\mathrm{r}}$), anti-green ($\bar{\mathrm{g}}$), and anti-blue($\bar{\mathrm{b}}$), making six possible states for the quantum number in total. Gluons have two color charge quantum numbers, one charge and one anti-charge. This fact means gluons interact with themselves, which produces two important effects in QCD: confinement and asymptotic freedom.

In QED, electromagnetic fields decrease with distance away from a point charge. This functional form allows electromagnetically bound states to separate. However in QCD, the self interaction of the gluon means that as two quarks separate, the energy between them grows proportionally to the distance between them. As a quark-antiquark ($\mathrm{q\bar{q}}$) pair separates, each quark in the pair has so much potential energy that quarks are pulled from the vacuum to bind to each quark to form two new pairs. The outcome of this effect is that solitary quarks can never be observed in a vacuum, by the time we try to observe them they will have found another particle in the vacuum with which to bind. This means that quarks are confined to zero color charge (or color neutral) bound states. Color neutral bound states are defined as a color and anti-color state (ex. $r\bar{r}$, $g\bar{g}$, $b\bar{b}$), known as mesons, or a tricolor state (ex. rgb or $\bar{r}\bar{g}\bar{b}$), known as baryons. The list of the two or three quarks which make up color neutral bound state are known as valence quarks. Valence quarks determine the quantum number for the hadron in contrast to sea quarks which are $q\bar{q}$ pairs made from gluon annihilation. Quarks and gluons found in hadrons are known as partons, and partons carry a fraction of the hadron's total momentum x. Partons can have any momentum fraction of the total momentum, but it is most probable that valence quarks have on average a large of the total momentum where as gluons and sea quarks are more likely to have a much smaller momentum fraction. Figure **??** shows measured parton distribution functions in the proton, illustrating the difference of the average x for valence quarks in contrast to sea quarks.

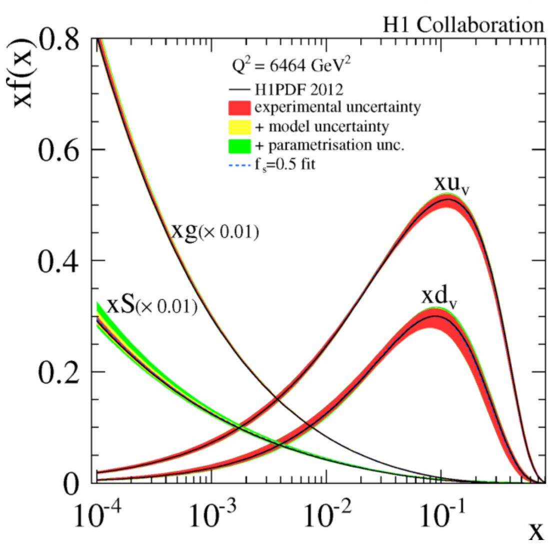

Figure 1.2: Parton distribution functions (PDF) of the the momentum fraction x in the proton extracted from the data taken by the H1 Collaboration. The curves xS, xg, xu_v, and xd_v correspond to PDFs of sea quarks, gluons, up valence quarks, and down valence quarks in the proton. The gluon g and sea S distributions are scaled by a factor 0.01. The uncertainties include experimental (inner) and model (middle) uncertainties and the parametrization variations (outer) [4].

Color neutrality can arise from other combinations of quarks; from combinations of quarks and gluons; or even arrangements of gluons with no valence quarks. The first mentioned combinations are theoretical color neutral states of four or more quarks, of which tetra and penta quarks have observed [?]. The second and third mentioned combinations are known as exotic mesons or glueballs and there are experiments searching for their signatures.

Another related effect of the self-interaction of the gluon is known as the screening of bare color charges. Once again it is helpful to compare to the familiar effects in QED. In QED, electrically charged pairs from the vacuum screen out the bare electric charge, causing the effective charge to decrease. This effect increases as the distance to the electric charge increases because there is a larger quantity of electrically charged pairs between the observer and the charge. Back to QCD, q$\overline{q}$ pairs produce the same effect, providing a screening effect on the bare color charge, however short-lived the bare color charges are. Further complications arise when the color-carrying gluon in turn creates an anti-screening effect, which is the larger of the two effects. As one approaches a solitary color charge, the density of gluons becomes so large that the strong force counter-intuitively grows weaker. These screening effects alter the strong coupling constant known as α_s; Figure 1.1.1, which depicts the α_s as a function of energy scale, shows the reduction of α_s at large energies. This behavior is known as asymptotic freedom because the smaller α_s is, the more quarks can move freely. Thus, there is an energy threshold where the strong force is weak enough where perturbative calculations are valid. The ability to make valid perturbative calculations for QCD is important for being able to make any in-depth QCD calculations of complex systems. Apart from perturbative QCD calculations, lattice QCD is a non-perturbative approach which is formulated on a lattice of space-time points. Although lattice QCD calculations are computationally complex, physical phenomena such as quark confinement can be treated numerically.

In addition to understanding the unique effects of QCD, understanding the phases of QCD matter is important. Figure 1.1.1 is a phase diagram for quark matter with temperature and net baryonic density on the axes. The type of quark matter which makes up the elements of normal matter is found in the figure under the heading of "Nuclear Matter" which is the state of quarks and gluons for complex, relatively stable bound states known as nuclei. The "hadronic phase" indicates a state of quark matter where bound states of quarks form hadrons but those hadrons behave like a weakly coupled gas. At very large baryonic density, the "color superconductivity"

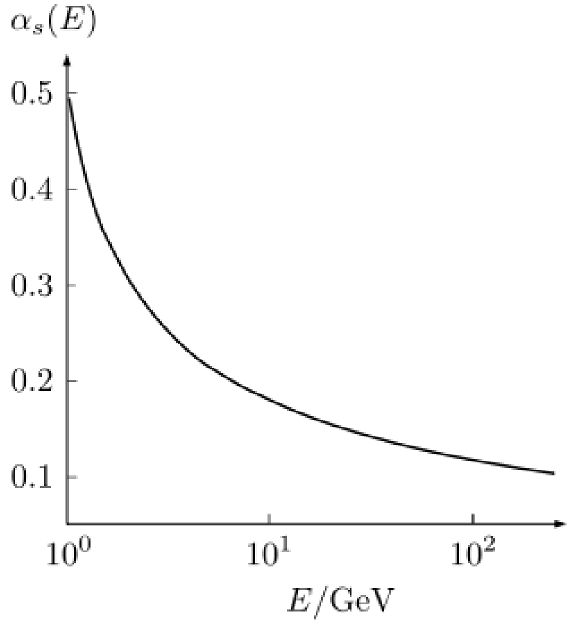

Figure 1.3: The strong coupling α_s as a function of energy of the square root of the energy or momentum transfer Q [14].

phase is where the possible quantum states of quarks and gluons are so full that a neutron star is possible example of such a state of matter. Finally, under extreme conditions of temperature and bayonic density, quarks may be deconfined and exist as solitary color charges in a plasma. This phase of matter, known as the QGP, provides a medium where screening effects are dominant and α_s becomes small enough to allow quarks and gluons to move with relative freedom. Although the QGP has been observed by multiple at RHIC (Relativistic Heavy Ion Collider) and LHC (Large Hadron Collider) facilities, the critical temperature at which the phase of quark matter is achieved is still unknown. One lattice QCD calculation estimates the temperature to be at 160–180 MeV or 1.7–1.9$\times 10^{12}$ kelvin, which is much hotter than the center of our sun [?].

Lattice QCD calculations have been done to examine the relationship of the number of massless degrees of freedom and the temperature of the medium as which provide insight in how QGP and the early universe transition into normal matter. Figure 1.1.1 shows a curve of a quantity inversely proportional to the number of massless degrees of freedom. As the temperature drops, the less massive particles annihilate and disappear from the thermal universe, reducing the degrees

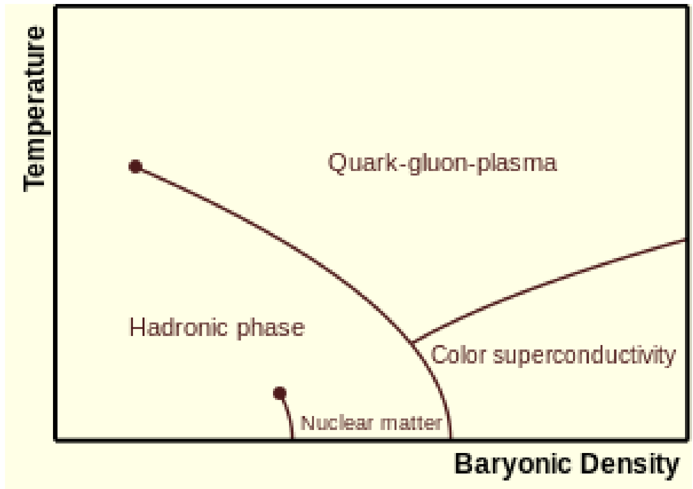

Figure 1.4: QCD phase diagram of with temperature on the y-axis and net baryonic density on the x-axis [15].

of freedom. The points on Figure 1.1.1 are the numerical results from a lattice QCD calculation of the Equation of State (EoS). The y-axis for the points on this plot is the energy density divided the temperature to the fourth power $\frac{\epsilon}{T^4}$ which has been shown to be inversely proportional to the number of massless degrees of freedom [17]. It is noteworthy that the points increase around the transition indicating the emergence of new degrees of freedom around the transition temperature of the medium.

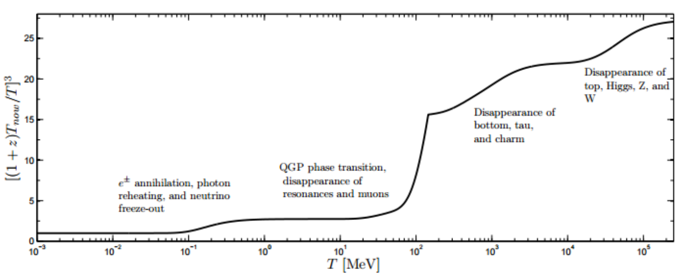

Figure 1.5: Disappearance of degrees of freedom through the evolution of the Universe in time and how this affects the fractional drop of temperature compared to red-shift [47].

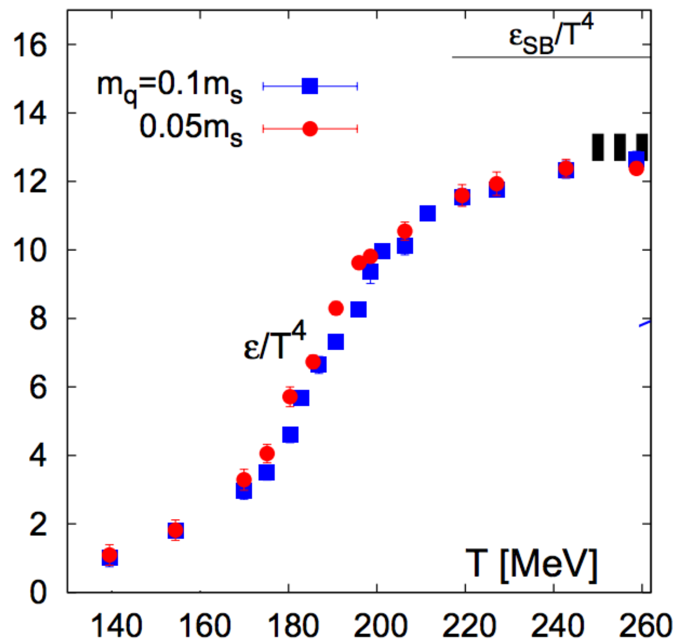

Figure 1.6: The energy density ϵ divided by T^4 vs temperature T at the physical value of the light quark mass [17].

1.2 Quark Gluon Plasma

the QGP is a new state of matter created in laboratories and is thought to be the same as the entire early universe approximately one microsecond after the big bang [46]. Thus, studying QGP and its properties in the laboratory can help cosmologists understand the state of the early universe.

The idea of hot hadronic matter was developed in the early 1950s by various physicists including Enrico Fermi [24]. This concept of applying statistical and hydrodynamical models to a strongly interacting particle ensemble ultimately evolved into the theory of the QGP. Since then, systematic studies of hot hadronic matter systems have produced a greater understanding of the state of matter hypothesized to be the QGP and contributed to its approximate location on the nuclear matter phase diagram in Figure 1.1.1. Many unique properties about this new state of matter have been discovered: for example, QGP behaves like a nearly perfect fluid and is opaque to color charges [10]. Enough research has been done to assemble a probable timeline of how the

QGP evolves.

1.2.1 The QGP Evolution Timeline

The timeline overview of the QGP as made in the laboratory always begins with a high-energy heavy ion collision (Au+Au for example), thus the QGP timeline is embedded in the laboratory timeline. The beginning of QGP starts with initial state observable particles and ends with final state observable particles, although the final state particles may have been produced at different points during the QGP evolution. Although only lasting $\sim 10^{-23}$ seconds or $\sim 10 fm/c$, several distinct stages occur during this time period and long after the evolution has ceased the final state particles are detected in the experiment one quadrillion QGP lifetimes or one nanosecond later.

At the moment when heavy ions collide relativistically ($\tau = 0$), they are length contracted down to flat disks in the lab frame, as seen in Figure 1.2.1. Then, the initial geometry resulting from the shape of the collision overlap region and fluctuations within the nuclei are transformed into the initial energy density of the medium ($\tau \approx 1$ fm/c). At that moment, the hot hadronic matter is thought to be made up of deconfined quarks and gluons. The system then evolves hydrodynamically, expanding along the pressure gradients present in the initial energy density. At a certain point during this expansion, the medium has cooled down enough in order to form baryons and mesons out of the quark gluon soup in a process hadronization. It is important to note that the medium is still in thermal equilibrium at this point although it is no longer a QGP but instead a hadron gas. Once the medium has cooled down and expanded sufficiently, kinetic freeze-out occurs and the hadron gas becomes a group of particles which have ceased interacting ($\tau \approx 10$ fm/c). It is this group of final state particles which can be detected much later. Although detectable particles escape the medium at all times, the vast majority of particles detected are decoupled at kinetic freeze-out.

Even though all of these phases are of interest to the study of QGP, of particular interest to physcists is the thermal equilibrium phase when the QGP state is first achieved. It is during this phase where quarks are deconfined, the only phase where this occurs. In this environment, features of QCD can be studied, such as how color charges experience energy loss and to what degree is collective behavior observed.

As is referred to in Figure 1.2.1, many types of particles are emitted during the QGP evolution, some of which are emitted before the kinetic freeze-out time. The most common type of particle produced from heavy ion collisions are baryons and mesons made of up, down, and strange quarks (pions, Kaons, and nucleons), which are in abundant supply during and after the collision. Another type of particle produced from these collisions are photons. The QGP being an extremely hot ball of matter, blackbody radiation in the form of thermal photons are emitted and their spectrum can be used to estimate the temperature of the medium. These thermal photons escape the medium due to their lack of interaction with the strong force. Heavy quarks are produced primarily from initial hard parton-parton scatterings, "hard" meaning here that there is a large momentum transfer in the collision. These heavy quarks, such as bottom or charm quarks, often fragment into a shower of lower energy particles known as jets as they propagate through space.

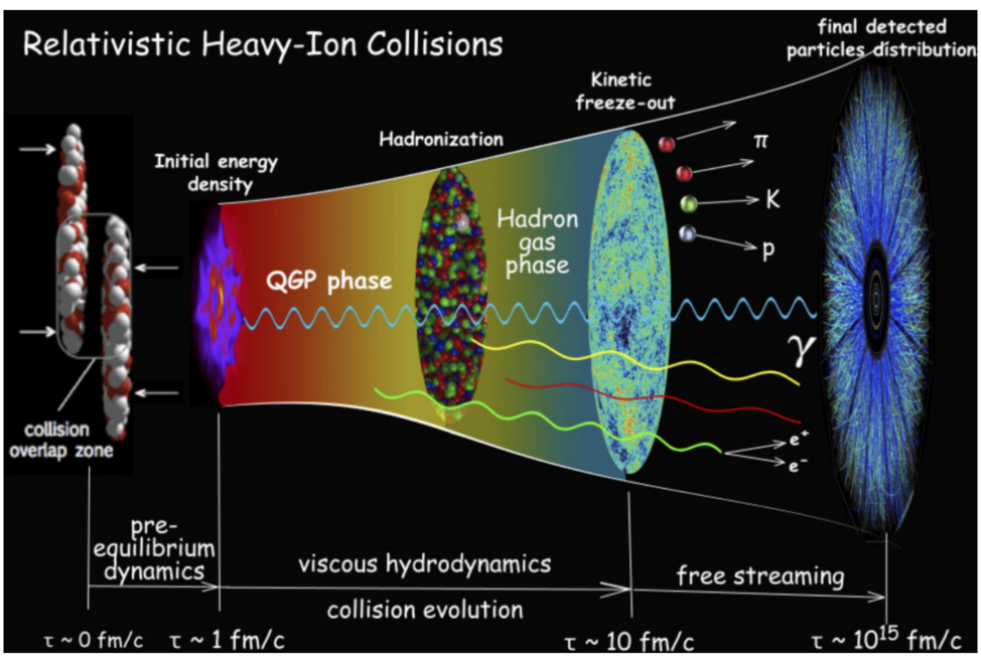

Figure 1.7: Relativistic heavy ion collision evolution timeline starting. Three distinct phases and their times are shown as well as the particles produced [29].

1.2.2 Emergent Properties of the QGP

Now that the foundation of the QGP timeline has been established, properties of the medium can be discussed in context. Up to this point in this document, the label of QGP has been applied to state of matter produced from heavy ion collisions, but what evidence is there that this state of matter is a strongly coupled medium made of deconfined quarks and gluons?

Taking into account that the field of high-energy heavy ion collision physics is still evolving, several measured properties of this state of matter have come together to make the QGP the prevailing explanation. Among the best observations indicating QGP formation are particle energy loss and elliptic flow. The observation of hadrons at large p_T measured at much lower yields than expected imply that the hadrons are experiencing energy loss when interacting with a strongly coupled medium. An elliptic symmetry in the angular distribution of final state particles when viewed with respect to the beam axis has been observed. The translation of initial geometry into long-range angular correlations indicates collectivity in a strongly coupled medium.

1.2.2.1 Particle Energy Loss

In order to study the new medium, it is useful to measure things about the QGP relative to a more well known collision system such as p+p. By measuring the relative number of hadrons produced at various transverse momentums in both p+p and heavy ion collisions, QGP medium effects can be teased out.

After the quarks are produced in p+p collisions, they will hadronize and freely travel to the experiment's detector. In heavy ion collisions, the quarks propagate through, and interact with, the QGP, exchanging energy and momentum with the medium along the way. The effect of energy loss on these quarks will modify their yield relative to the yield in p+p collisions. The nuclear modification factor R_{AA} is the observable used is to quantify this modification which is defined for a given particle as:

$$R_{\mathrm{AA}}(p_T) = \frac{dN_{A+A}/dp_T}{\langle N_{\mathrm{coll}}\rangle \times dN_{p+p}/dp_T}, \tag{1.1}$$

where dN_{A+A}/dp_T and dN_{p+p}/dp_T is the yield of a given particle vs p_T (transverse momentum) in heavy ion collisions and p+p collisions respectively and $\langle N_{\mathrm{coll}}\rangle$ is the average number of binary collisions for a given class of events. In summary, the R_{AA} is a ratio for how many particles are produced for the same system with a normalization factor of $\langle N_{\mathrm{coll}}\rangle$ to account for the differences in system size. The $\langle N_{\mathrm{coll}}\rangle$ value is usually determined using Monte Carlo Glauber simulations and will be discussed in more detail in Chapter 2. If the particles do not interact with the medium, the R_{AA} should be equal to 1.0. A value above 1.0 is interpreted as an enhancement of particles and a value below 1.0 is interpreted as a suppression of particles.

Figure 1.2.2.1 shows a significant suppression in the R_{AA} vs p_T of π^0 mesons produced in Au+Au collisions at $\sqrt{s_{NN}}$ = 200 GeV at RHIC for large and small sized QGP events, 0-10% centralilty and 80-92% centralilty events respectively (centrality will be discussed in Chapter 2). This large suppression across all p_T of the π^0 for central events as compared to peripheral events indicate energy loss of quarks due to the medium, which is consistent with a strongly coupled medium.

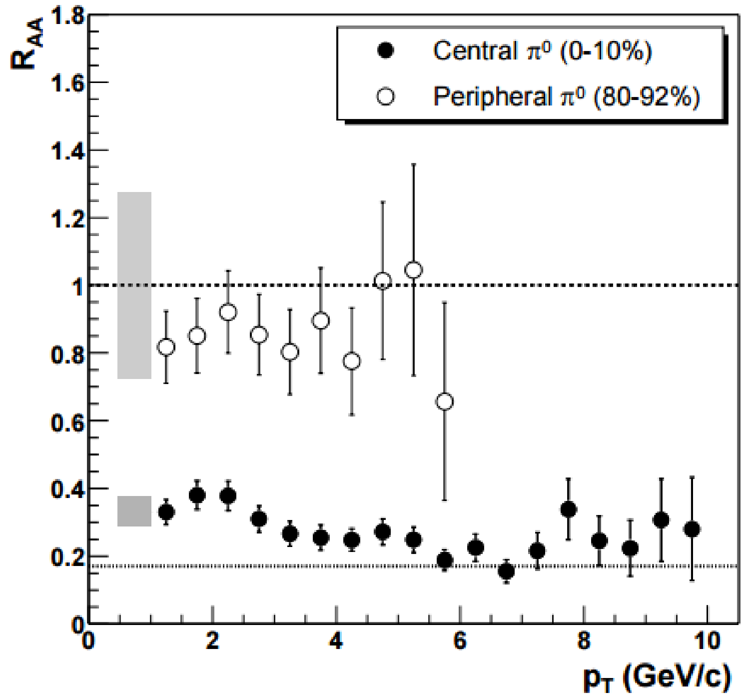

Figure 1.8: The R_{AA} vs p_T of π^0 mesons produced in Au+Au collisions at $\sqrt{s_{NN}}$ = 200 GeV at RHIC for two different collision multiplicity classes. [8]

1.2.2.2 Collective Flow and Azimuthal Anisotropy

Another signal of a strongly coupled medium is collective behavior amongst the constituent particles which make up the medium. By analyzing patterns in the spray of particles emitted from heavy ion collisions, systematic effects can be determined. Nominally there should be no preference in direction for final state particles from a heavy ion collision, the presence of such a preference can indicates correlations among the particles in the medium which can be measured by looking at the azimuthal anisotropy.

Consider the collision of two heavy nuclei as depicted in Figure 1.2.2.2. The overlap region between the two nuclei form an almond shaped region oriented to the plane of the initial collision geometry. After the collision the two nuclei remnants (the blue shapes) no longer participate and the yellow overlap region forms the QGP medium and starts to expand. This energy density distribution gives rise to a larger pressure gradient in the shorter direction. The larger the pressure gradient, the more momentum the particles will gain once the medium finishes evolving. This variation in the momentum of final state particles produces effects in the azimuthal (relative to the collision axis) distribution of particles. Therefore, by measuring the azimuthal anisotropy of the final state particles, long-range angular correlation like those present in Figure 1.2.2.2 can be measured. The initial state collision geometry being transformed into final state momentum anisotropy indicates collective behavior and elliptical flow of the particles.

In order to quantify the azimuthal anisotropy, the final state particle distribution is Fourier transformed:

$$C(\Delta\phi) \propto 1 + \sum_{n=1} 2v_n \cos(n\Delta\phi) \tag{1.2}$$

where $C(\Delta\phi)$ is the correlation function defined by the distribution of the differences between the azimuth of particles from the event relative to other particles in the same event, and v_n are flow coefficients. The flow coefficients v_n are proportional to the degree of anisotropy for each harmonic order n. A v_n of 0.0 would indicate there is no azimuthal anisotropy. More detailed information about the correlation function and other methods for quanitfying the azimuthal anisotropy are

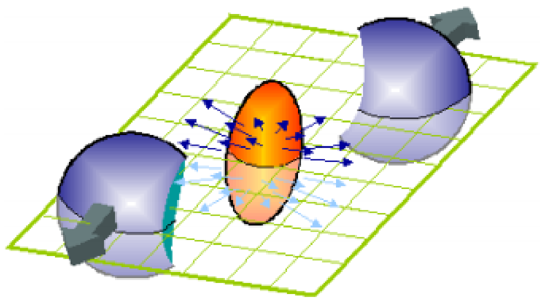

Figure 1.9: A diagram of a heavy ion collision. The blue shapes are the two colliding nuclei and the elliptical yellow shape is the collision overlap region which forms the medium. In the next instant of time the two nuclei would travel father along the collision axis (into and out of the page) and the medium would expand along the direction of the arrows [45].

given in Chapter 2.

In addition to measuring the v_n for various systems, a relativistic hydrodynamic calculation can be compared to the data. Figure 1.2.2.2 shows v_n vs p_T for both RHIC and LHC energy heavy ion collisions for mid-peripheral events, such as those depicted in Figure 1.2.2.2. The very good agreement with hydrodynamic calculations curves suggests a medium which flows.

All of the discussion and results shown in this section have been referring to large collision systems such as Au+Au or Pb+Pb. Small collision systems such as p+A, d+Au, or p+p were thought to be too small to produce a QGP, and thus were ideal as the control experiment to measure background effects of cold nuclei which may obscure the true signal of the QGP. However, recent results have shown that small collision systems show signs of QGP formation. Chapter 2 will delve into small collision systems properties and measurements, as well as give a more in-depth discussion in calculating initial conditions and flow coefficients.

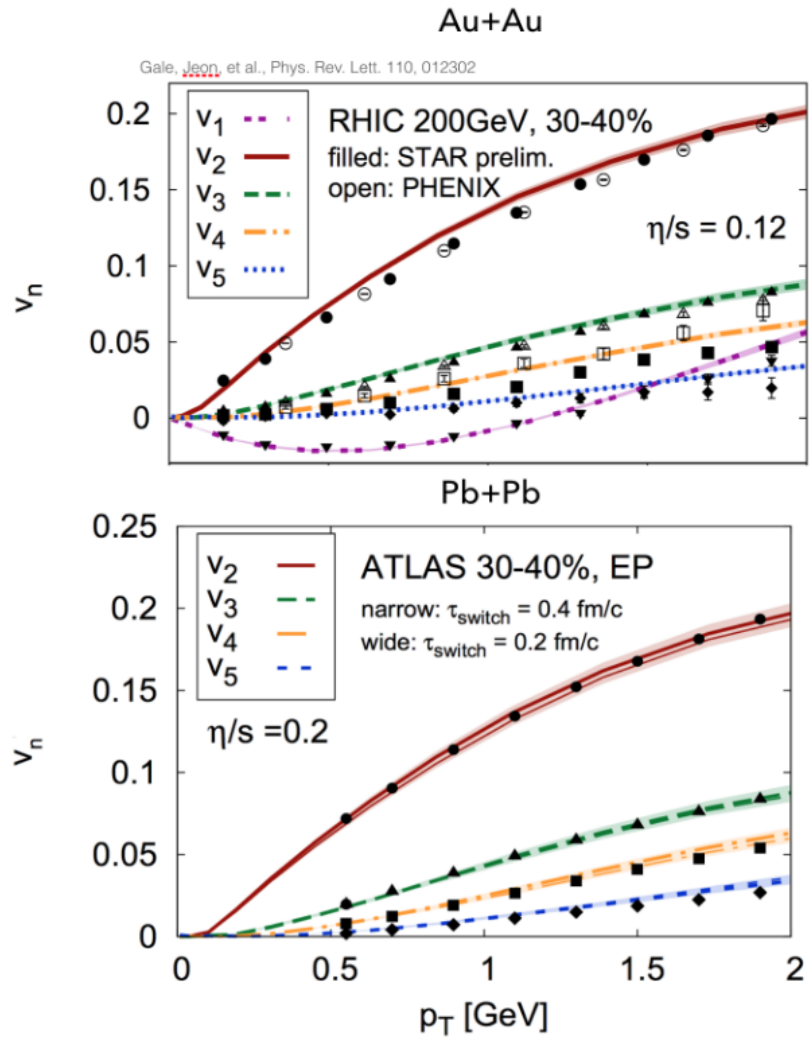

Figure 1.10: v_n vs p_T for RHIC Au+Au at $\sqrt{s_{NN}}$ = 200 GeV and for LHC Pb+Pb at $\sqrt{s_{NN}}$ = 2.76 TeV for mid-peripheral events for harmonic orders n up to five. The colored curves are the hydrodynamic calculations. The η/s is the viscosity parameter used in the calculations [26].

Chapter 2

Collectivity and Flow in QCD Systems

2.1 A Conceptual Understanding of Collectivity and Flow

The observation of collectivity in matter can be a powerful indicator of fundamental properties in that matter. Collectivity means many discrete structures are interacting together to form a whole otherwise known as highly correlated behavior. In high energy heavy ion physics, a common interpretation of this behavior, although not the only interpretation[1] , is of a locally equilibrated medium with bulk properties instead of a group of individually weakly interacting constituent particles. In this case, the medium would be QGP and the bulk properties would be that of a hydrodynamically described fluid: viscosity, density, temperature, etc. The term collectivity is often synonymous with the term hydrodynamic flow or simply flow. In this thesis, the terms will be used synonymously except in specific cases where the distinction is important.

It is important to note that although collectivity has a distinct signal, there are possible sources that can produce such a signal which do not involve collective behavior. These sources are called "non-flow" to differentiate them from sources of collectivity, such as flow. Especially true in small collision systems, non-flow is the largest background component when measuring collectivity. Thus, when making measurements, often non-flow must be taken into account as either a systematic uncertainty or as a systematic error correction. Sources of non-flow will be discussed more in Chapter 4 Section 4.5.4.

[1] Although it is common to think of collectivity as hydrodynamic behavior, observations of collectivity do not necessarily imply any specific interpretation. Later we will discuss some alternative interpretations such as glasma correlations.

To assist in the discussion of flow, we will briefly describe how it is measured. Generally flow can be observed in heavy ion collisions by looking for long-range angular correlations between the spray of final state particles that come out of the collision. “Long-range angular correlations” in this case refers to correlations in particles with trajectories that have a large separation in pseudorapiditiy η. When looking for correlations, this separation in η ensures that we are measuring something other than just local correlations, which are often due to non-flow.

Conceptually, the story of flow is that patterns in the initial conditions of the medium will be carried through the medium evolution and be observable in the final state particles. Figure 2.1 demonstrates the key events in the story: initial state geometry becomes transformed into a final state momentum anisotropy. The consideration of initial collision geometry will be a reoccurring theme when interpreting results in this thesis because the initial state geometry is one of the few independent variables over which we have experimental control.

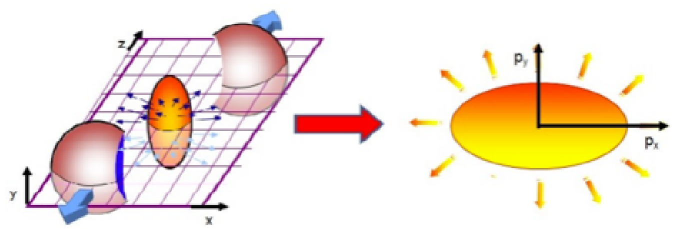

Figure 2.1: A diagram demonstrating the relation between initial state geometry being transformed into final state momentum anisotropy. The left depicts two spherical nuclei colliding parallel to the z-axis. The pair of nuclei leave behind an ellipsoidal shaped medium. This ellipsoid hydrodynamically evolves such that it expands along the steepest pressure gradient which corresponds to the transverse direction. The right depicts the elliptical pattern present in transverse momentum distribution of the final state particles after the medium has finished evolving [26].

2.1.1 Initial Conditions

Before proceeding to describing flow mathematically, it is useful to talk about the initial conditions of heavy ion collisions. When talking about collisions of spherically symmetric bodies, one of the most relevant parameters in characterizing collisions is known as the impact parameter.

The impact parameter is the distance between the center of mass of each collision body, the larger the impact parameter, the more peripheral the collision. For heavy ion collisions, it is useful to consider peripheral collisions along with other types, as shown in Figure 2.2. The degree in which the colliding nuclei overlap is known as the "centrality." A small value for centrality, for example 0-10%, corresponds to more central collision events, while a large value for centrality, for example 60-100%, corresponds to more peripheral collisions. The method for quantifying the event's centrality is discussed in Chapter 3.

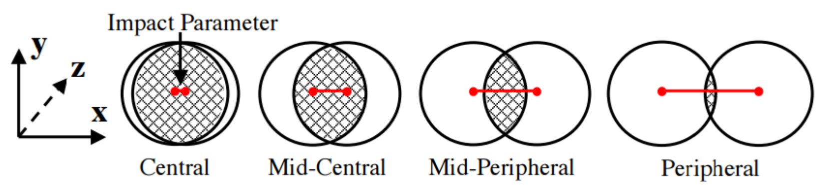

Figure 2.2: A diagram of the possible initial conditions of heavy ion collisions. The impact parameter is the red line. The language used in heavy ion physics is as follows: the larger the overlap between the colliding nuclei, the more central it is, the smaller the overlap, the more peripheral it is. Adapted from [48].

2.2 Mathematical Introduction to Measuring and Quantifying Flow

As discussed above, looking for long-range angular correlations is a way to measure flow. Measuring the azimuthal anisotropy is a way to quantify the extent of long-range angular correlation present in the medium evolution. Azimuthal anisotropy is the degree to which measured particles are non-uniform in the transverse plane. There are a number of ways to measure the azimuthal anisotropy. We will start by creating a correlation function.

2.2.1 Two-Particle Correlations

A correlation function is dependent on the difference in particles' trajectories, rather than the trajectories of the particles themselves. Let us consider the two-particle correlation function which uses **pairs** of particles from a collision event in order to create a correlation function. For each pair in an event, a $\Delta\phi = \phi_1$ - ϕ_2, and a $\Delta\eta = \eta_1$ - η_2, value is obtained which makes up the signal $S(\Delta\phi, \Delta\eta)$ for a single event:

$$S(\Delta\phi, \Delta\eta) = \sum_{j=1}^{N_{\text{particles}}} \left(\sum_{i=j+1}^{N_{\text{particles}}} s(\phi_i - \phi_j, \eta_i - \eta_j) \right) = \sum_{k=1}^{N_{\text{pairs}}} s(\Delta\phi_k, \Delta\eta_k), \tag{2.1}$$

where $s(\phi_i - \phi_j, \eta_i - \eta_j) = s(\Delta\phi_k, \Delta\eta_k)$ is a single pair in an event, $N_{\text{particles}}$ is the number of particles in an event, and N_{pairs} is the number of unique pairs in an event. This pair counting scheme ensures that no pair will be double counted and that a particle can not form a pair with itself.

Ideally, this $S(\Delta\phi, \Delta\eta)$ would be the correlation function; however, there are artificial correlations due to detector acceptance and other sources which would distort this distribution. In order to correct for these effects, a mixed event background distribution $M(\Delta\phi, \Delta\eta)$ is created, whereby pairs are produced by particles from two different events. The correlation function can be defined as follows:

$$C(\Delta\phi, \Delta\eta) = \frac{S(\Delta\phi, \Delta\eta)}{M(\Delta\phi, \Delta\eta)} \frac{\int M(\Delta\phi, \Delta\eta)\, d\Delta\phi d\Delta\eta}{\int S(\Delta\phi, \Delta\eta)\, d\Delta\phi d\Delta\eta}, \tag{2.2}$$

where the integration is over the full $\Delta\phi, \Delta\eta$ range in order to normalize the correlation function. Substantial variations in this $C(\Delta\phi, p_T)$ are usually seen as long-range angular correlations which can be attributed to collectivity.

In practice, correlation functions often combine particles from two different p_T ranges. The first p_T range corresponds to the "trigger" particles and the second range to the "associated" particles. In this scheme, the pair function is $s(\phi_i^t - \phi_j^a, \eta_i^t - \eta_j^a)$ where the t superscript indicates trigger particles with a given p_T range and the a superscript indicates associated particles with a given p_T range.

Two examples of 2-D two-particle correlation functions; one for p+p at $\sqrt{s_{NN}} = 7$ TeV with no multiplicity selection, and one for Pb+Pb at $\sqrt{s_{NN}} = 2.76$ TeV high multiplicity events are shown in Figure 2.3. The trigger and associated p_T ranges are given in the figure caption. Plotting the correlation function in terms of both $\Delta\phi$ and $\Delta\eta$ allows one to see the full extent and location of correlations for the collision system. These two correlations were selected to showcase the two extremes of typical correlation functions.

An important feature in the left plot is the large strength of correlations at $(\Delta\phi, \Delta\eta) =$ (0,0), which is known as the nearside[2] "jet peak." As mentioned in Chapter 1, jets are a spray of particle in a cone shape; therefore, the jet peak is at (0,0) because all the particles within the jet have a similar trajectory. The jet peak has been truncated for plotting reasons because it is so large. Another important feature is what is known as the "awayside ridge" or "awayside jet peak" located at $\Delta\phi = \pi$ and extending very far in the $\Delta\eta$ variable. This feature arises when back-to-back dijets are produced; all of the particles from one of the jets will be roughly π radians apart in trajectory with respect to the other jet and spread out in $\Delta\eta$. Apart from these main features which come from jets and dijets, there are no other major sources of correlations between particles for minimum bias p+p events, such that p+p events are taken to be the representation of the non-flow background. Minor sources of additional non-flow are in pure decays, Coulomb interactions, and momentum interference. Thus, correlation function features present in regular p+p events are taken to be present at some level in the correlation function of every heavy ion collision system.

Conversely, the right panel of Figure 2.3 depicts the correlation function of high multiplicity Pb+Pb events which exhibit characteristics of flow. While the non-flow features of the nearside jet peak and the awayside peak are present, a new feature known as the "nearside ridge" is located at $(\Delta\phi, \Delta\eta) = (0,|\Delta\eta| >\sim 1.0)$. This ridge exists in contrast to the lack of any correlations in the p+p correlation function at that location. It should be noted that the awayside jet ridge has also been modified. The nearside ridge and the awayside ridge modification are due to particles with long-range angular correlations. Thus, by quantifying the magnitude of these effects, the degree to which flow is present in the system can be measured.

[2] For correlation functions, $\Delta\phi \sim$0 is known as "nearside" and $\Delta\phi \sim \pi$ is known as "awayside."

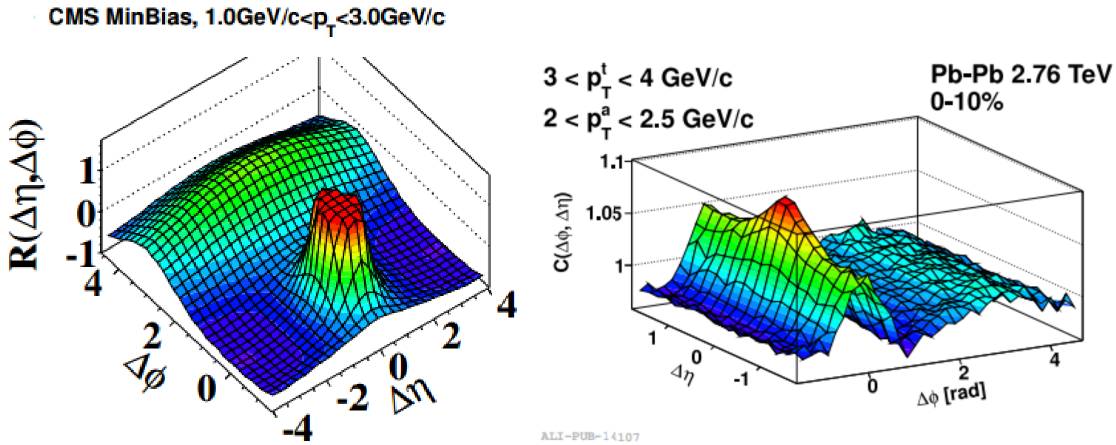

Figure 2.3: The right plot is 2-D two-particle correlation function for p+p collisions at $\sqrt{s_{NN}}$ = 7 TeV for hadrons with the same trigger and associated p_T range of $1.0 < |p_T| < 3.0$ GeV/c for all events [32]. The left plot is 2-D two-particle correlation function for Pb+Pb collisions at $\sqrt{s_{NN}}$ = 2.76 TeV 0-10%centrality events for trigger hadrons with $3 < p_T^t < 4$ GeV/c and associated hadrons with $2 < p_T^t < 2.5$ GeV/c measured by ALICE [32].

2.2.2 Flow Harmonics

At this point, it useful to narrow our focus to the region of the correlation function which has long-range angular correlations by taking a projection in $\Delta\phi$ away from the jet peak at $\Delta\eta = 0$. This 1-D two-particle correlation function slice contains the azimuthal anisotropy which should correspond to the degree of flow present in the system. Figure 2.4 depicts this correlation function $C(\Delta\phi)$ for central Pb+Pb events. In order to quantify the azimuthal anisotropy, $C(\Delta\phi)$ is cosine Fourier expanded:

$$C(\Delta\phi) \propto 1 + \sum_{n=1} 2v_n \cos(n[\Delta\phi]), \tag{2.3}$$

where v_n are known as flow coefficients or flow harmonics and n is the harmonic order [57]. The colored curves in Figure 2.4 are the first five components of the Fourier decomposition and their amplitudes show their relative strength. The green curve, which peaks at $\Delta\phi = 0$ and π, corresponds to the second order harmonic, which is related to the second order flow coefficient v_2. The reason v_2 is singled out is because it corresponds to elliptic flow and because it is the observable measured in this thesis. In order to extract v_2 from this, one must calculate c_2 defined as:

$$c_2^{t,a} = \langle \cos(2(\phi_1^t - \phi_2^a)\rangle, \tag{2.4}$$

where $\langle\rangle$ is defined as the average over all events and all particle pairs and where ϕ_1^t and ϕ_1^a is the trigger and associated particles' ϕ, respectively. If the trigger and associated particles sets are the same then $\sqrt{c_2} = v_2$; however, if the trigger and associated particle sets are not the same then $c_2^{t,a}{=}v_2^t \times v_2^a$, where v_2^t is the v_2 for the set of trigger particles alone and the same with v_2^a. This ability to resolve c_2 into the two distinct v_2 components is only true if factorization holds, which only occurs when the non-flow component of the measurement is small. This coefficient v_2 directly characterizes the elliptic flow of the number of particles emitted along the direction of the steepest pressure gradient in the initial ellipsoid shown in Figure 2.1.

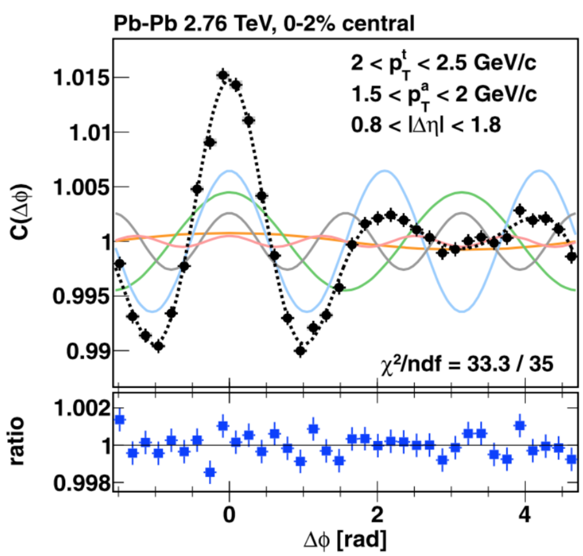

Figure 2.4: The 1-D correlation function in Pb+Pb at $\sqrt{s_{NN}}$ = 2.76 TeV for the most central events for for trigger hadrons with $2 < p_T^t < 2.5$ GeV/c and associated hadrons with $1.5 < p_T^t < 2$ GeV/c. The 1-D two-particle correlation function is a projection in $0.8 < |\Delta\eta| < 1.8$ from the 2-D correlation function, the 2-D correlation function being similar to that of the right panel of Figure 2.3. The black dotted points are the values of the correlation function and the colored lines are the first five cos Fourier decomposition components. The black dotted line is the sum of these five components [3].

2.2.3 Cumulants

Although two-particle correlations are useful, four-particle correlations or more can be used to better understand the flow measurement. In a multi-particle cumulant treatment, $c_n\{k\}$ measures the nth harmonic from groups of k particles while explicitly subtracting correlations from $< k$ particles. In this formulation, two-particle cumulants are treated the same way as in two-particle correlation functions:

$$v_2\{2\} = \sqrt{c_2\{2\}} = \sqrt{\langle \cos(2(\phi_1 - \phi_2)) \rangle}, \tag{2.5}$$

whereas four-particle cumulants are defined as:

$$v_2\{4\} = (-c_2\{4\})^{1/4} = (2\,\langle \cos(2(\phi_1 - \phi_2)) \rangle)^2 - \langle \cos(2(\phi_1 + \phi_2 - \phi_3 - \phi_4)) \rangle)^{1/4}, \tag{2.6}$$

where the term with four ϕ indices corresponds to the four-particle correlation and the term with two ϕ indices corresponds to the subtracted off two-particle correlation term. Multi-particle cumulants are well defined for larger groupings of particles, $v_2\{6\}$, $v_2\{8\}$, and up. Comparing v_2 measured by two and four-particle cumulants is useful when estimating the level of fluctuations present in the system, something which will be discussed more in Section 2.4.3.

2.2.4 Event Plane Formulation

Another mathematical treatment for determining flow coefficients involves measuring a mathematical object known as an “event plane.” Conceptually, the event plane method is an attempt to measure the reaction plane angle, which defines the plane to which it is aligned with the orientation of the initial state collision geometry. Figure 2.5 is a geometric diagram defining the reaction plane angle Ψ_{RP}.

The event plane method uses final state particles to calculate the event plane angle from the data. A different event plane angle is defined for each harmonic, and is denoted as Ψ_n where n is the harmonic number. For an event with N particles, define the flow vector $\vec{Q}$ as follows:

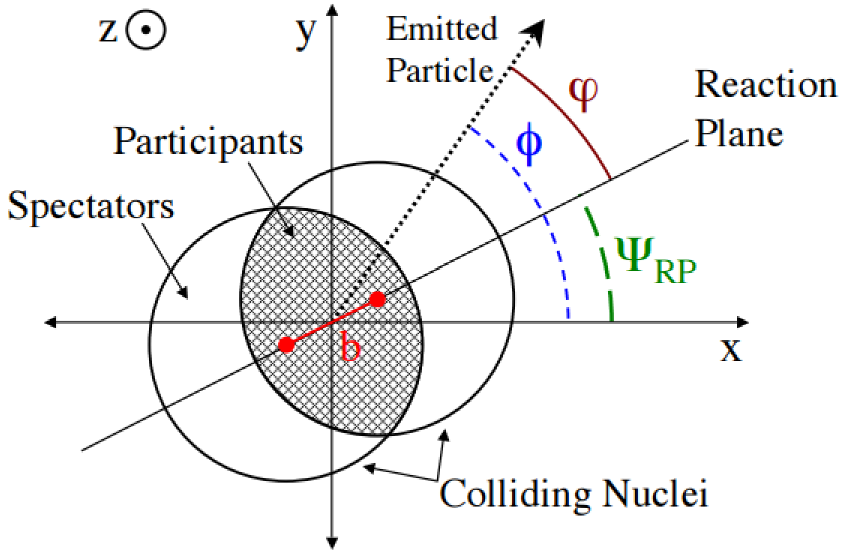

Figure 2.5: Diagram showing from the beams point of view several variables used to characterize events. The spectators are the nucleons which do not participate in the collision, as opposed to the participants which do participate in the collision. The impact parameter denoted as b and Ψ_{RP} is the reaction or participant plane angle. ϕ is the standard azimuthal and $\varphi = \phi$ - Ψ_{RP}. Adapted from [48].

$$Q_x = \sum_{i}^{N}(w_i * \cos(n * \phi_i)) \tag{2.7}$$

$$Q_y = \sum_{i}^{N}(w_i * \sin(n * \phi_i)) \tag{2.8}$$

$$Q_w = \sum_{i}^{N}(w_i) \tag{2.9}$$

where i is the ith particle in the event, ϕ_i is the azimuthal angle of the particle, w_i is the weight factor, and n is the harmonic number.

We define the nth order event plane as $\Psi_n = \arctan\left(\frac{Q_y}{Q_x}\right)$

Once the event plane has been calculated, the flow harmonics (v_n) are defined as

$$v_n = \frac{\langle\langle\cos(n(\phi - \Psi_n))\rangle\rangle}{Resolution(\Psi_n)}, \tag{2.10}$$

where $\langle\langle\rangle\rangle$ indicates that $\cos(2\phi - \psi)$ is averaged over all particles in the same event, and the resulting v_2 must be averaged over many events [44].

The event plane resolution is calculated using the standard 3-sub event method [44]. The strategy of this method is to measure Ψ_n with three different detectors in the same event, in order to better constrain the overall measurement of Ψ_n. The event plane resolution is defined as

$$Res(\Psi_n^A) = \sqrt{\frac{\langle \cos(n(\Psi_n^A - \Psi_n^B))\rangle \langle \cos(n(\Psi_n^A - \Psi_n^C))\rangle}{\langle \cos(n(\Psi_n^B - \Psi_n^C))\rangle}}, \tag{2.11}$$

where A,B, and C are three detectors measuring the same event. In this context, the term "sub-event" refers to the specific subset of particles measured by a given detector [44].

2.3 An Overview of Heavy Ion Collectivity Models

Throughout the discovery phase of the Quark Gluon Plasma and beyond into precision measurements, simulations based on theoretical descriptions of heavy ion collisions have been developed and have been successful in describing and predicting physics results. From the initial state of the colliding nuclei to the final state particles produced, every phase of heavy ion collisions are modeled. First the initial condition models will be discussed and then the medium evolution models will be discussed. It is necessary when calculating observables like v_n to choose an initial state model and a medium evolution model to chain together. The output of the initial state model will be the input to the medium evolution model; therefore, even if the medium evolution model describes the physics well, an initial state model which does not do so would cause the final v_n calculation to be inconsistent with the data.

2.3.1 Initial Condition Models

Initial condition models use a variety of methods to simulate the colliding nuclei. These models calculate quantities for characterizing initial collision conditions, such as the number of participating nucleons (N_{part}), the impact parameter (b), and the participant eccentricity (ε). The N_{part} is the total number of neutrons and protons from the nuclei that suffer at least one inelastic collision, and is thought to be related to the size of the medium produced. The ε_n categorizes the

nth order anisotropy in the initial collision geometry which is given by:

$$\varepsilon_n = \frac{\sqrt{< r^2 \cos(n\phi) >^2 + < r^2 \sin(n\phi) >^2}}{< r^2 >} \tag{2.12}$$

where r is the radius of the participant nucleon, relative to the center of mass. This quantity is important because $v_n \propto \varepsilon_n$ in the limit of ideal hydrodynamics [11].

A key part in simulating initial the conditions of heavy ion collisions is understanding event-to-event fluctuations. An important source of fluctuations, generic to all models of quantum fluctuations, are fluctuations in the distributions of nucleons in the nuclear wavefunctions. In addition, there are fluctuations in the color charge distributions inside a nucleon. This, combined with Lorentz contraction, results in lumpy transverse projections of color charge configurations that vary event to event. There are more sophisticated models where there are simple constituent quark models with the three color charge centers in the nucleon [58]. The scale of this lumpiness is given on average by the nuclear saturation scale Q_s which corresponds to distance scales smaller than the nucleon size . For each such configuration of color charges, the Quantum Chromo-Dynamics (QCD) parton model predicts dynamical event-by-event fluctuations in the multiplicities, the impact parameters, and the rapidities of produced gluons [51].

2.3.1.1 Monte-Carlo Glauber

There are two main Glauber models: the so called "optical" Glauber model which assumes a smooth density described by a Fermi distribution in the radial direction; and the Monte-Carlo-based Glauber model where individual nucleons are stochastically distributed on an event basis and collision properties are determined by averaging over multiple events. The optical form of Glauber does not locate nucleons at specific spatial coordinates like the Monte Carlo form of Glauber. While both models give consistent results for determining simple quantities such as $\langle N_{part} \rangle$ and b, the impact parameter, the more statistical Monte-Carlo approach has given ε_n values that are necessary for the described experimental data. One benefit of the Monte-Carlo approach for quantities like N_{part} is its simplicity and ability to simultaneously simulate experimentally observable quantities, such as charged particle multiplicity distribution.

The Monte-Carlo Glauber (MC Glauber) model calculation is performed in two steps. At first, the nucleon positions in each nucleus are stochastically determined. Then, the two nuclei are collided, assuming the nucleons travel in a straight line along the beam axis (known as the Eikonal approximation), such that nucleons are tagged as wounded (participating) or spectator.

The position of each nucleon in the nucleus is determined according to a probability density function. The probability distribution is typically taken to be uniform in azimuthal and polar angles. The radial probability function is modeled from nuclear charge densities extracted in low-energy electron scattering experiments. The nuclear charge density is usually parameterized by a Fermi distribution with three parameters:

$$\rho(r) = \rho_0 \frac{1 + w(r/R)^2}{1 + exp(\frac{r-R}{a})} \tag{2.13}$$

where ρ_0 is the nucleon density, R is the radius of the nucleus, a is the skin depth, and w corresponds to deviations from a spherical shape.

The impact parameter of the collision is chosen randomly from a distribution dN/db $\propto b$ up to some large maximum bmax with bmax 20 fm $> 2R_A$. The longitudinal coordinate does not play a role in the calculation. The inelastic nucleon-nucleon cross section ($\sigma_{_{NN}}$), which is only a function of the collision energy is extracted from p+p collisions. At the top RHIC energy of $\sqrt{s_{_{NN}}}$ = 200 GeV, $\sigma_{_{NN}}$ = 42 mb, while at the LHC it is expected to be around $\sigma_{_{NN}}$ = 72 mb [38]. The ball diameter is defined as:

$$D = \sqrt{\frac{\sigma_{_{NN}}}{\pi}}. \tag{2.14}$$

Two nucleons from different nuclei are assumed to collide if their relative transverse distance is less than the ball diameter. If no such nucleon-nucleon collision is registered for any pair of nucleons, then no nucleus-nucleus collision occurred. An example Au+Au collision event is show in Figure 2.6. In this thesis, MC-Glauber combined with negative binomial distributions is used to match the charged particle multiplicity distribution in order to map N_{part} to centrality classes. Details for this procedure are given in Chapter 3, Section xxx.

As stated earlier, and important initial condition quantity in simulating flow is the ε of the event. MC Glauber simply calculates the moments of the participants themselves for each event. The eccentricity ε_2 can be calculated along the axis of the participant distribution ε_{part}:

$$\varepsilon_{part} = \frac{\sqrt{(\sigma_x^2 - \sigma_y^2)^2 + 4(\sigma_{xy}^2)^2)}}{\sigma_x^2 - \sigma_y^2} \tag{2.15}$$

where $\sigma_{x,y}^2$ are the x and y variances for participating nucleons and σ_{xy} is the covariance of x and y for pariticipating nucleons.

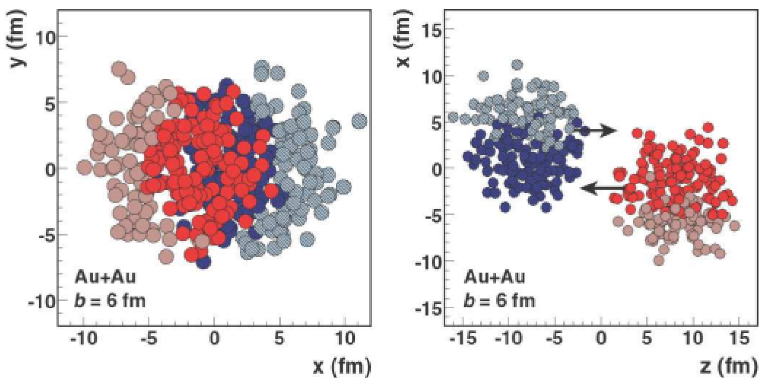

Figure 2.6: Glauber Monte Carlo event (Au+Au $\sqrt{s_{NN}}$ = 200 GeV with impact parameter $b = 6$ fm) viewed in the transverse panel and alone the beam axis in the left and right panels, respectively. The deeper color disks correspond to the participating nucleons [38].

2.3.1.2 IP-Glasma

Another initial state model is known as IP-Glasma. This model calculates the initial conditions within a Color Glass Condensate (CGC) framework by combining the impact parameter dependent saturation model (IP-Sat) with the Classical Yang-Mills (CYM) description of initial Glasma fields. Calculating initial state dynamics by flowing Glasma gluon fields is thought to be an *ab initio*, or from first principles, approach, although some of the parameters of the model are fixed by diffractive e+p DIS data. The IP-Glasma computation starts by sampling the positions of the constituent nucleons from a Fermi distribution. Then the saturation scale $Q^2_{s,(p)}(x, \mathbf{b})$ is obtained from IP-Sat dipole cross section for each nucleus, where b is the impact parameter relative to each participant nucleon's center. Once the saturation scale and the color charge density are obtained, random color charges are sampled from a transverse lattice [51].

A benefit of the IP-Glasma model is that it explicitly includes multiple types of quantum fluctuations, including fluctuations of color charges within the nucleons. It is useful to compare the calculations of IP-Glasma to MC-Glauber in order to gain a greater understanding of both.

2.3.1.3 Comparison between IP-Glasma and MC-Glauber

Figure 2.7 depicts the energy density distributions calculated by the IP-Glasma and MC-Glauber models. It is apparent from the "lumpiness" of both of these distribution that these models capture the complex internal structure of the nuclei at the moment of collision. However, the MC-Glauber distribution is much smoother than the IP-Glasma distribution due to the fact that the IP-Glasma distribution incorporates fluctuations at a much finer length-scale, given by $1/Q_s(x)$, which creates the spikey structures in the energy distribution. Apart from the differences in the length-scale of fluctuations between the models, MC-Glauber includes the energy distribution from every participant nucleon in the collision event, no matter how glancing its individual collision is, with the same parameters of width. Thus, the MC-Glauber model's procedure for incorporating participating nucleons is less sophisticated than a model like IP-Glasma. Note that for MC-Glauber, the width of a nucleon's energy density has been chosen to be 0.4 fm for all nucleons to match the MC-Glauber model to the data, despite the fact there are no *ab initio* calculations which derive such a number.

2.3.2 Medium Evolution Models

Once an energy density distribution is calculated from the initial condition models, it used as the input to a medium evolution model. The most commonly used medium evolution model is the relativistic hydrodynamic model.

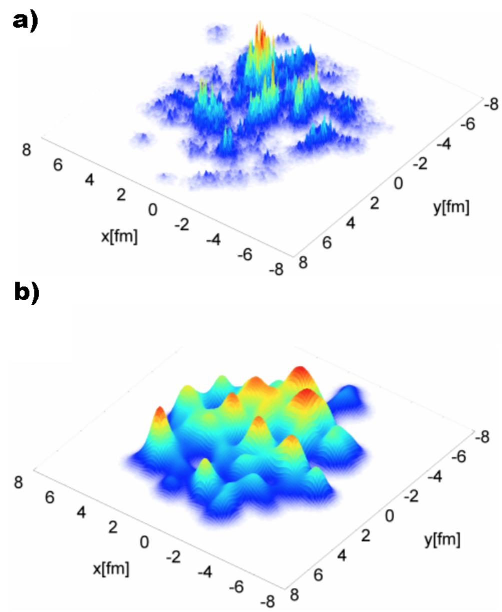

Figure 2.7: Initial energy density distributions (arbitrary units) in the transverse plane in two different heavy-ion collision events for IP-glasma (top) MC-Glauber (bottom) models [51].

2.3.2.1 Hydrodynamic Modeling

Relativistic hydrodynamics is a macroscopic tool to simulate the evolution of a strongly coupled QGP medium. It is based on the foundational physical principles of conservation of energy, momentum, and net charge current which are written as:

$$\delta_\mu T^{\mu\nu}(x) = 0, \tag{2.16}$$

$$\delta_\mu N^{\mu}(x) = 0, \tag{2.17}$$

where $T^{\mu\nu}$ is the energy momentum tensor and N^μ is the net baryon charge current. Ideal hydrodynamics requires that the medium is locally equilibrated, such that we have the perfect fluid energy momentum tensor as $T^{\mu\nu} = (e+p)u^\mu u^\nu + pg^{\mu\nu}$ where e is the relativistic rest energy density, p is the fluid pressure, $g^{\mu\nu}$ is the Minkowski metric, and u^μ is the four-velocity of fluid. Also, the charge current becomes $N^\mu = nu^\mu$ where n_0 is the net baryon density. After asserting an equation of state (EoS) $p = p(n_0, e)$, the system is closed and the equations can be solved numerically.

Viscous hydrodynamics is similar to ideal hydrodynamics except that viscous hydrodynamics applies to a wider variety of systems, such as imperfectly locally equilibrated systems. In order to account for the lack of equilibrium, several new variables must be introduced: $\pi^{\mu\nu}$ is the sheer stress tensor, Π is the bulk pressure, η is the shear viscosity, ζ is the bulk viscosity, V^{μ} is the baryon flow, and τ_{π} and τ_{Π} are the corresponding relaxation times. At RHIC and LHC energies, the net baryon density n_0 is nearly zero and v^{μ} is assumed to be zero. By choosing a proper EoS (equation of state), an initial flow velocity, and an initial entropy/energy density at time τ_0, the medium evolution can be simulated for time $\tau > \tau_0$. Note that in order to simulate very early stages during the QGP formation, modifications to this hydrodynamic formulation must account for pre-equilibrium conditions [54]. An example of a viscous hydrodynamic evolution is shown in Figure 2.8 for a collision of ^{3}He+Au.

To obtain final state hadrons, pure hydrodynamic simulations assume free hadron resonances directly emit from the fluid along a decoupling surface. The Cooper-Frye formula [18] is then implemented to calculate the particle momentum distributions, which is followed by a resonance decay routine to generate final stable hadrons. The decoupling or freeze out surface can be defined by a constant temperature or energy density or other kinetic variables. For the scenario of constant temperature decoupling, T_{dec} is generally set to 150-170 MeV, depending on the EoS and other hydrodynamic inputs, to allow for sufficient evolution time to build up enough radial flow to fit the slopes of the p_T spectra [33].

To simplify numerical simulations, many viscous hydrodynamic calculations assume a specific velocity profile v_z = z/t along the beam directions (Bjorken approximation). This approximation leads to a longitudinal boost invariance and reduces the (3+1)-d hydrodynamics to (2+1)-d hydrodynamics. This approximation has shown that the realistic longitudinal expansion only slightly affects the flow profiles at mid-rapidity [54].

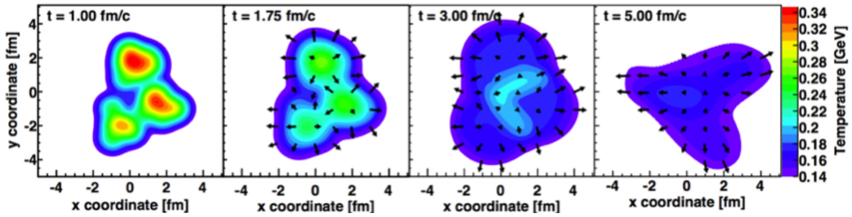

Figure 2.8: An example time evolution of a ^{3}He+Au event from the initial state to final state. The color scale indicates the local temperature and the arrows are proportional to the velocity of the fluid cell from which the arrow originates [40].

2.3.2.2 Hybrid Models: SONIC and superSONIC

Here we detail one specific model, noting that many viable hydrodynamic models have been developed [15]. A hybrid model matches hydrodynamic descriptions of the expanding QGP to microscopic Boltzmann simulations of the evolving hadronic matter. The transition between models is realized by a Monte-Carlo event generator, which transforms the hydrodynamic output into individual hadrons for succeeding hadron cascade propagations.

The "Super hybrid mOdel simulatioN for relativistic heavy-Ion Collisions" (SONIC) combines pre-equilibrium dynamics with hydrodynamics [36] and a late-stage hadronic cascade [39]. In effect, SONIC has only a limited number of parameters, namely those specifying the properties of the incoming nuclei, equation of states as input to from lattice QCD, and shear and bulk viscosities in the QGP. As discussed when describing initial conditions models, fluctuations play a large role in determining the hydrodynamic flow. In order to study the effects of fluctuations in simulation, SONIC is an event-by-event simulation is created by inputing fluctuating initial conditions, evolving each system separately, and then averaging the results.

SuperSONIC is the next generation of the SONIC model, differing from SONIC by incorporating pre-equilibrium dynamics with a calculation in the framework of the AdS/CFT correspondence [49]. The SONIC and superSONIC models agree well with the data within uncertainties.

2.3.3 AMPT

A Multi-Phase Transport (AMPT) model combines partonic and hadronic scattering in a single model. AMPT is the culmination of many models together. It is in an alternative to the hydrodynamic approach of medium evolution by using partonic strings instead of fluid cells as the building blocks of the model. The use of partonic strings preserve discrete particle information throughout the simulation which is useful in dissecting simulations. Despite the fact that AMPT is not a hydrodynamic model, it still is consistent with substantial flow coefficients as will be shown in Chapter 5.

AMPT consists of four main components: the initial conditions, partonic interactions, the conversion from the partonic to the hadronic matter, and hadronic interactions. AMPT uses the Heavy Ion Jet Interaction Generator (HIJING) for generating the initial conditions, Zhang's Parton Cascade (ZPC) for modeling partonic scatterings, the Lund string fragmentation model or a quark coalescence model for hadronization, and A Relativistic Transport (ART) model for treating hadronic scatterings. The HIJING model converts the initial incident energy to the production of hard minijet partons and soft strings, with excited strings further converting to partons in the AMPT model with string melting. Then ZPC is used to model the interactions among partons. An implementation of the Lund string fragmentation converts the excited strings to hadrons. The ART model is used for for describing interactions among hadrons [35].

2.4 A Review of Flow Measurements in Small Collision Systems

As noted at the end of Chapter 1, small collision systems have long been considered too small to create hot and dense matter. These systems were utilized as control experiments which measure how the presence of a nucleus would effect the production of particles relative to p+p collisions. These so called "cold nuclear matter" (CNM) effects were isolated when colliding very low Z nuclei, such as a deuteron or proton, with a large nucleus.[3] Generally accepted CNM effects are:

[3] A side note: the convention in the field of heavy ion physics is to label any such small system collisions as p+A and any large system collisions as A+A

nuclear shadowing, which is the modification of parton distribution functions by a nucleus; gluon saturation, which is the saturation of gluon distribution functions where no gluons can be added; radiative energy loss, which is the modification of the momentum fraction of partons due to multiple soft scatterings; and finally the Cronin effect, which is the broadening of the transverse momentum of emitted particles distribution due to multiple scatterings of initially colliding partons [25].

2.4.1 Nearside Ridge in Small Systems

In 2010, the CMS collaboration published a paper observing a nearside ridge in high multiplicity 7 TeV p+p events in the two-particle correlation function for dihadrons as shown in the left Figure 2.9. The aforementioned nearside ridge is located at $\Delta\phi = 0$ and at $|\Delta\eta| > 2$ in the figure. The ridge is significant in contrast to the p+p correlation function shown in the right panel of Figure 2.9 with an absence of any such ridge.

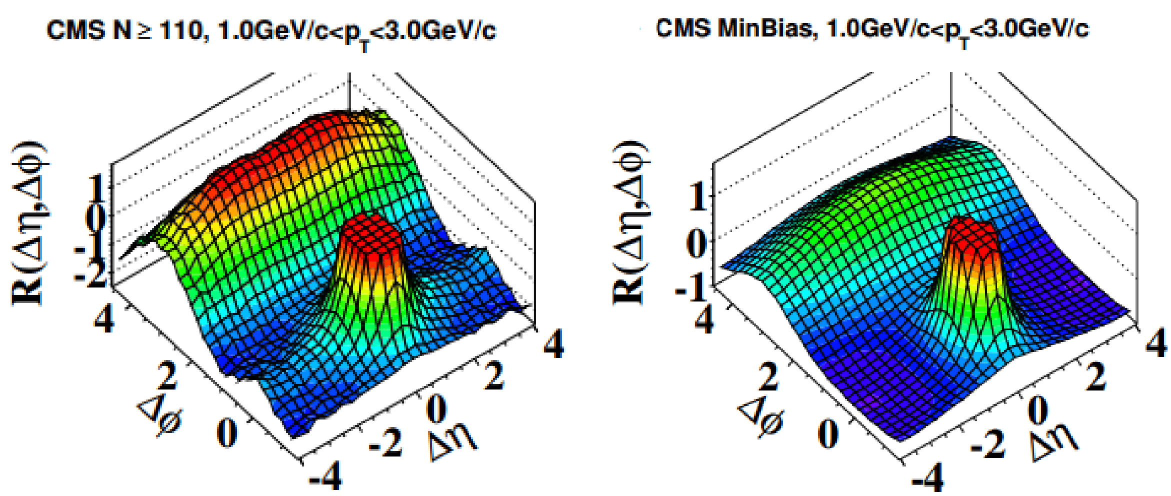

Figure 2.9: 2-D two-particle correlation function for p+p collisions at $\sqrt{s_{NN}} = 7$ TeV for hadrons with $1.0 < |p_T| < 3.0$ GeV/c in high multiplicity events, with greater than 109 charged particles, and for any multiplicity of events are shown in the left and right panels, respectively [32].

What this discovery showed was that collectivity-like effects could be measured in small collisions systems for high-multiplicity events. Thus, p+Pb at $\sqrt{s_{NN}} = 5.02$ TeV events were also analyzed to find flow and a nearside ridge was observed in 0-20% central events. It became apparent over the course of making these measurements that the non-flow contribution to the signal would be much larger for p+p and p+A events then that of A+A events and so perhaps these were not related to flow. However, a procedure to reduce the non-flow component in the flow measurement is demonstrated in Figure 2.10. The procedure measures the same two-particle correlation function for central and peripheral events, in this case 0-20% central and 60-100% central and then subtracts the central correlation function by the peripheral one. The assumption is that the level and shape of the non-flow is mostly consistent across centrality classes, whereas the flow is centrality dependent, such that there is virtually no flow in the peripheral correlation function. Thus, by subtracting the central correlation function by the peripheral, only the common components to both will be subtracted out, which are the non-flow components. As seen in panel three in Figure 2.10, the subtracted correlation function has no dominating jet peak at (0,0) and the nearside and awayside ridges are distinct and clear, with a signal dominated by elliptic flow.

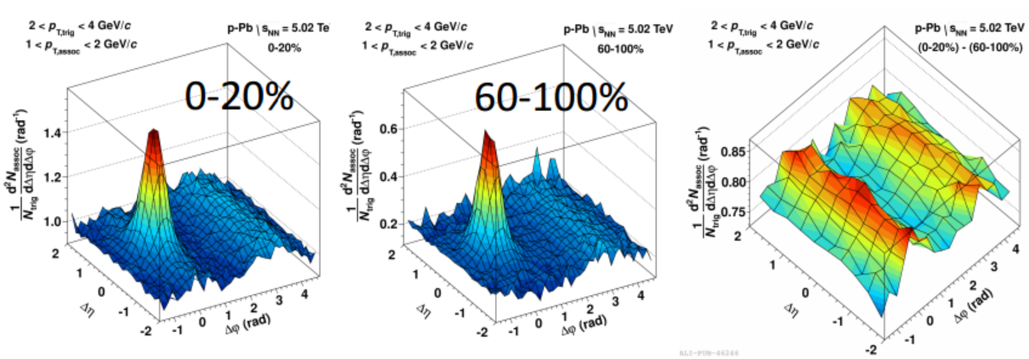

Figure 2.10: 2-D two-particle dihadron correlation function for p+Pb collisions for 0-20% and 60-100% centrality events as measured by the ALICE detector in the left and middle panel, respectively. The rightmost panel shows the subtraction of the left panel by the middle panel to remove background. [?]

2.4.2 Mass Ordering in v_2

A key observation in the determination of real collective flow is a mass ordering in the strength of the flow coefficients. This is due to a common velocity field in the fluid which then results in a larger momentum boost for heavier particles. The left panel of Figure 2.11 depicts the observed mass ordering of particles in Pb+Pb 10-20% centrality events. In the low p_T region of 0 - 2 GeV, there is an ordering in the magnitude of v_2 for hadrons: $\pi^{\pm} > K^{\pm} > p{+}\bar{p}$ and so on for other heavier particles. The $\pi^{\pm}$ v_2 is the largest while the $\pi^{\pm}$ mass is the smallest. Assuming an elliptic flow is present, the steep pressure gradients will efficiently modify the magnitude of p_T for heavy hadrons more than for light hadrons, leading to a reduction in the number of heavy hadrons available at low p_T to produce a low p_T v_2 [30]. Thus, the mass ordering observation is taken to be evidence that the system is creating a medium such that particles will flow in predictable ways.

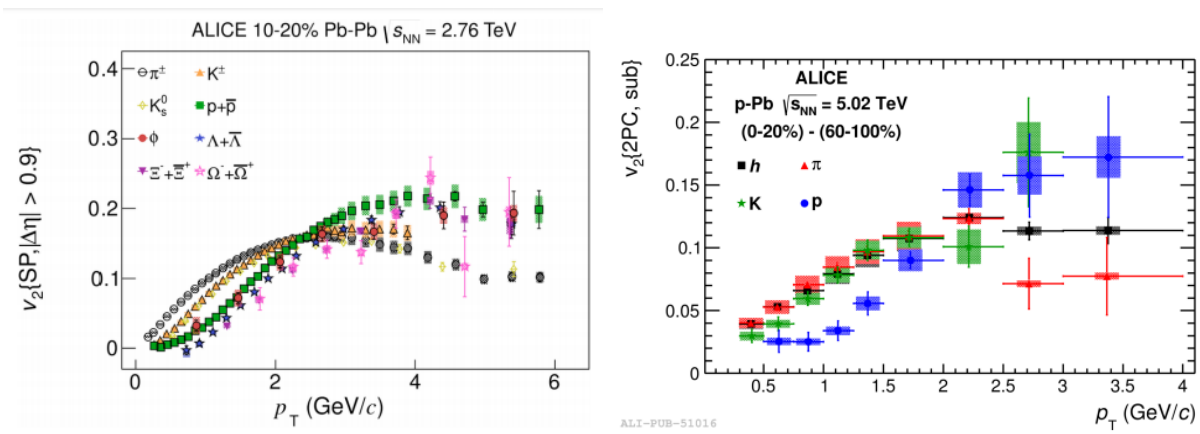

Figure 2.11: $v_2(p_T)$ for different particles (see legend) in Pb-Pb $\sqrt{s_{NN}}$ = 2.76 TeV 10-20% events as measured by the ALICE detector. The $\Delta\eta$ gap at minimum is 0.9 units. The right plot shows the $v_2(p_T)$ for different particles (see legend) in p-Pb $\sqrt{s_{NN}}$ = 5.02 TeV for 0-20% events that were subtracted by peripheral 60-100% events. The v_2 is extracted directly from the two particle correlation function shown in Figure 2.10. **add refs**

The right panel of Figure 2.11 shows a similar plot to the left panel of that figure except for the system p+Pb $\sqrt{s_{NN}}$ = 5.02 TeV. As in the Pb+Pb system, the p+Pb dataset exhibits a the same mass ordering, as well as similar shapes of each $v_2(p_T)$ curve. Thus, the mass ordering effect that is observed in A+A is also observed is small systems, such as p+A. An important note for the result on the right panel is that a central minus peripheral subtraction was done, as demonstrated in Figure 2.10, whereas the result in the left panel needed no such peripheral subtraction. This means it is difficult to compare directly with the A+A result in magnitude, although the similarity of the ordering and the shape of the curves is enough of a comparison to indicate collectivity in the small system.

2.4.3 Multi-Particle Cumulants and Fluctuations

The effects of event-to-event fluctuations in the elliptic flow measurement have been studied in small systems. In this context, fluctuations are differences in the initial collision geometry ε_2 from one event to the next and so v_2 is different from one event to the next. Fluctuations in ε_2 can arise from fluctuations in the impact parameter within a centrality class of events and from fluctuations of the initial positions of the participant nucleons [41].

In order to better understand the effect of fluctuations in our small systems measurements, v_2 was measured in different ways such as, $v_2\{2\}$ and $v_2\{4\}$, which are given by Equations 2.5 and 2.6, respectively. The quantity $v_2\{2\}$ is the same as the two-particle correlation v_2, shown in Figure 2.11, while the quantity $v_2\{4\}$ is a four-particle correlation. This paper referenced here [41], defines a fluctuation term similar in form to standard deviation that is related to flow coefficients defined:

$$\sigma_\nu^2 \equiv \left\langle \nu^2 \right\rangle - \left\langle \nu \right\rangle^2 , \tag{2.18}$$

where ν is the flow coefficient relative to the participant plane. This fluctuation term is related to $v_2\{2\}$ and $v_2\{4\}$ as

$$\nu\{2\}^2 = \left\langle \nu^2 \right\rangle = \left\langle \nu \right\rangle^2 + \sigma_\nu^2, \tag{2.19}$$

and

$$\nu\{4\}^2 = (2 \left\langle \nu^2 \right\rangle^2 - \left\langle \nu^4 \right\rangle)^{1/2} \approx \left\langle \nu \right\rangle^2 - \sigma_\nu^2. \tag{2.20}$$

Thus, $v_2\{2\}$ measures the true elliptical flow plus fluctuations, whereas $v_2\{4\}$ measures the true elliptical flow minus fluctuations. By measuring both $v_2\{2\}$ and $v_2\{4\}$ for the same dataset, an estimate of the size of the fluctuations can be obtained. The difference between the two and four particle cumulants should be $\approx$ twice the size of the fluctuations.

Figure 2.12 shows the measurement of multi-particle cumulants in p+p, p+Pb, and Pb+Pb by the CMS collaboration at the LHC. A key part of this plot is noticing the significant difference between $v_2\{2\}$ and $v_2\{4\}$ in high multiplicity p+Pb and Pb+Pb events, indicating the presence expected geometry and thus flow fluctuations. In the p+Pb and Pb+Pb there is an apparent multiplicity threshold, approximately around $N_{trk}^{offline} = 75$, below which a class of peripheral events have a different kind of behavior than the high multiplicity events.

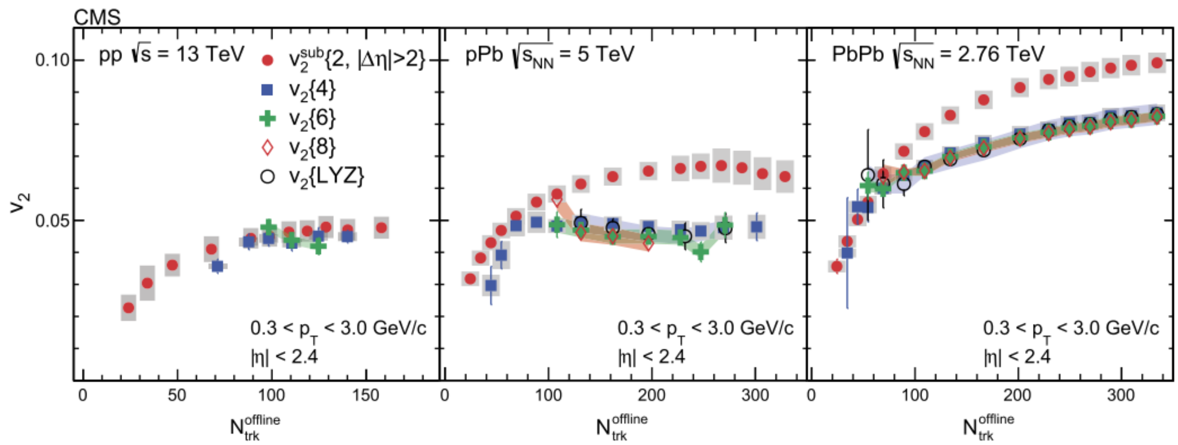

Figure 2.12: Elliptic flow measurements made using the 2nd, 4th, 6th, and 8th multi-particle cumulants, where the 2nd multi-particle is subtracted by peripheral events. Also the Lee Yang zero method non-flow elimination method is shown. These quantities are plotted vs the event multiplicity measured as $N_{trk}^{offline}$, which is the number of charged particle tracks observed during the offline analysis averaged over $0.3 < p_T < 3.0$ GeV/c and over $|\eta| < 2.4$. The left panel is $v_2^{sub}\{2, |\Delta\eta| > 2\}$, $v_2\{4\}$, and $v_2\{6\}$ in p+p collisions at $\sqrt{s} = 13$ TeV. The middle panel $v_2^{sub}\{2, |\Delta\eta| > 2\}$, $v_2\{4\}$, $v_2\{6\}$, $v_2\{8\}$, and $v_2\{LYZ\}$ in p+Pb at $\sqrt{s_{NN}} = 5$ TeV collisions. The right panel is $v_2^{sub}\{2, |\Delta\eta| > 2\}$, $v_2\{4\}$, $v_2\{6\}$, $v_2\{8\}$, and $v_2\{LYZ\}$ in Pb+Pb collisions at $\sqrt{s_{NN}} = 2.76$ TeV. The error bars correspond to the statistical uncertainties, while the shaded regions correspond to the systematic uncertainties [31].

It is also interesting to note that for both systems, the $v_2\{4\}$, $v_2\{6\}$, $v_2\{8\}$, $v_2\{LYZ\}$ are in excellent agreement. The $v_2\{LYZ\}$ is v_2 measured taking into account the Lee-Yang zeros by removing all lower-order correlations. This excellent agreement indicates that p+Pb is similar to Pb+Pb in that it is an N-body correlation, not a two-body decay or back-to-back jets which produces correlations between smaller numbers of particles. Although these types of processes are present, all particles feel the effects of the initial geometry.

2.4.4 Measurements Made at RHIC

Flow measurements in small systems have also be made at the lower energy accelerator, RHIC. Small collision systems, d+Au, ^{3}He+Au, and $p+Au$ at $\sqrt{s_{NN}}$ = 200 GeV per nucleon were taken at RHIC in 2008, 2014, and 2015, respectively. The 2008 d+Au dataset was intended to measure cold nuclear matter effects; however, RHIC experiments such as PHENIX had the capability to go back and measure $v_2(p_T)$. PHENIX was able to measure v_2 for d+Au and for ^{3}He+Au for the 0-5% most central events, as shown in Figure 2.13. A substantial v_2 is observed for both d+Au and ^{3}He+Au events with a strong p_T dependence, which is similar to that seen in p+Pb at the LHC. Instead of subtracting the non-flow component, as was done in Figure 2.10, the non-flow is incorporated as a systematic uncertainty. In addition to the v_2 measurement, a substantial v_3 is measured for the ^{3}He+Au dataset. This measurement is significant because the observation of more than one flow indicates the system is exhibiting complex behavior. A single flow harmonic could be explained by a variety of causes, whereas two flow harmonics from the same system narrow the range of possible explanations.

In addition to measuring the $v_2(p_T)$ for all hadrons, v_2 has been measured for $\pi^{\pm}$ and p+$\overline{p}$, as seen in Figure 2.14. A very similar mass ordering in $v_2(p_T)$ for different hadrons that was observed for p+Pb at $\sqrt{s_{NN}}$ = 5.02 TeV in Figure 2.11, was also observed for d+Au and ^{3}He+Au at $\sqrt{s_{NN}}$ = 200 GeV. In the low p_T region, p_T < 1.5 GeV, the v_2 for $\pi^{\pm}$ is greater than the v_2 for p+$\overline{p}$. An interesting note here is that the low p_T region only goes up to 1.5 GeV/c, whereas the p+Pb dataset shows a low p_T mass ordering region of up to 2 GeV/c. The reason for this is probably due to the difference in center of mass energy, and larger radial flow at the higher energy.

It is necessary to note that throughout all of these measurements in small systems, a skepticism to the interpretation that the measurements are hydrodynamic flow has persisted. There are alternative explanations to the apparent flow measured in small systems which do not involve the creation of a medium. Examples of these alternative examples explanations include:

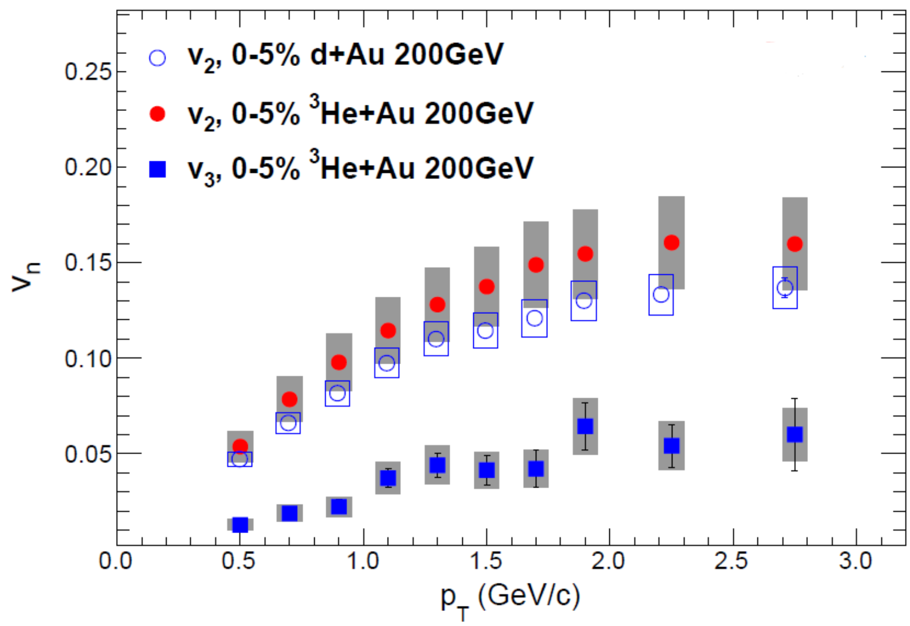

Figure 2.13: $v_n(p_T)$ measured for d+Au and ^{3}He+Au at $\sqrt{s_{NN}}$ = 200 GeV for 0-5% central events. v_2 was measured for both systems and v_3 was measured for ^{3}He+Au. The grey boxes correspond to systematic uncertainties [7].

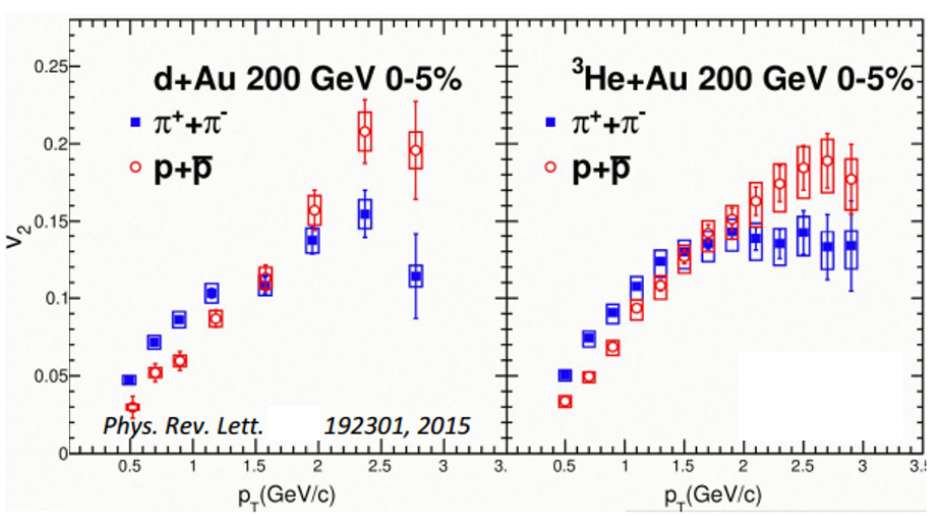

Figure 2.14: $v_2(p_T)$ for d+Au and ^{3}He+Au at $\sqrt{s_{NN}}$ = 200 GeV 0-5% centrality events for $\pi^{\pm}$ and $p+\bar{p}$ separately. The boxes correspond to the systematic uncertainty [7].

initial state effects from glasma diagrams [19], color recombination [43], and partonic scattering in transport models [16].In order to further the discussion on the distinction between a medium and a non-medium explanation, three different small collision systems, each with unique initial conditions, were run at RHIC. Those three systems are d+Au, ^{3}He+Au, and finally p+Au, with intrinsic elliptical, triangular, and circular geometric initial conditions. The constraints that a set of measurements from all three systems would place upon explanatory models would help distinguish which theory best describes small systems. This thesis is the completion of that set of three measurements, by measuring v_2 in the p+Au dataset.

Chapter 3

Experiment Setup

3.1 RHIC

The Relativistic Heavy Ion Collider (RHIC) is a superconducting charged hadron collider located at Brookhaven National Labs (BNL) in Upton, NY, United States. RHIC is capable of accelerating heavy ions such as Au (gold) or Cu (copper) nuclei to energies of $\sim$100 GeV per nucleon. RHIC is also capable of accelerating lighter ions such as protons, deuteron, and helium to $\sim$100 GeV per nucleon and $\sim$250 GeV per proton, in the case of p+p. The machine has been demonstrated the ability to reliably create the so called QGP (Quark Gluon Plasma) matter.

There are two major detector experiments currently operating in interaction regions around the RHIC ring: PHENIX (Pioneering High Energy Nuclear Interaction eXperiment) and STAR (Solenoidal Tracker at RHIC). Figure 3.1 shows the locations of the experiments and the accelerator chain. A typical schedule for RHIC is to operate the accelerator for five and a half months every year in what is called a "Run." There have been 16 Runs so far but the relevant Run for this thesis was the 15th Run taken in 2015 which ran proton colliding with gold ions (p+Au) $\sqrt{s_{NN}} = 200$ GeV for part of its running. Specific details about this dataset are found in Section 3.2.9.

The RHIC ring is at the end of a chain of smaller accelerators that are used to "feed" the ions into the RHIC ring, where they are accelerated (or decelerated in some circumstances) to the desired collision energy. For heavy ions such as Au, the process of production and acceleration is listed in detail below [50].

(1) A pulsed sputter Au ion source generates negative ions in the Tandem Van De Graaff.

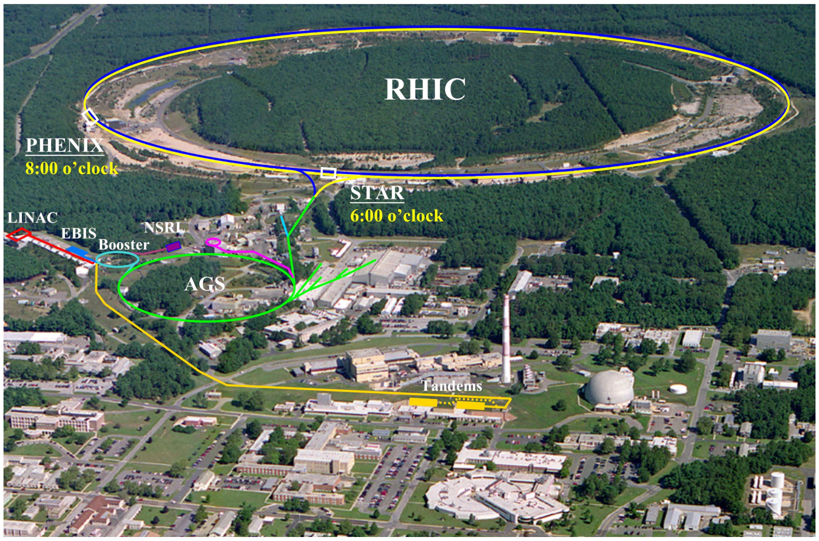

Figure 3.1: A helicopter's view of the accelerator chain in BNL starting at the Tandems (in gold) and ending at the RHIC ring (in blue and yellow for the two counter-circulating beams). STAR and PHENIX can be seen at two of the interaction regions. The ring is 2.38 miles in circumference [55].

(2) The ions are passed through an electron stripping foil to achieve a positive $+12\ e$ charge and accelerated to $\sim$1 MeV per nucleon.

(3) The ions pass through bending magnets and another foil to further strip electrons and filter charge, yielding to a positive $+32\ e$ charge state.

(4) The ions are sent to the Booster Synchrotron, which accelerates them to 95 MeV per nucleon and leaves them at a positive $+77\ e$ charge.

(5) The ions enter the Alternating Gradient Synchrotron (AGS) in bunches of 24 around the ring. The ions are debunched and rebunched into four bunches and then accelerated to 10.8 GeV per nucleon.

(6) The bunches then exit the AGS one at a time, where their Au ions are stripped of their two remaining electrons, yielding a final charge state of positive $+79\ e$. Finally, the bunches are transferred to their respective buckets in RHIC .

For protons, the process instead begins at the Linear Accelerator (LINAC) facility. The protons are then sent through the chain of accelerators in a similar way to the heavy ions until reaching RHIC in either a polarized or unpolarized spin state.

Once the ions have reached RHIC, they will enter one of two independent rings, blue or yellow, each circulating in an opposite direction. The ions in the rings are deflected and focused by 1,740 superconducting magnets using niobium-titanium conductors. Once the ions are focused and accelerated to the desired parameters around the RHIC, the ions are deflected into the six interaction regions where the blue and yellow rings intersect to produce collisions. It is at these interaction regions where the major experiments have set up their detectors, with STAR at the 6 o'clock position and PHENIX at the 8 o'clock position.

The period of time that collisions continue is known as a "fill," and the average length of a fill is eight hours. As the fill wears on, the collision rate substantially decreases as the density of ions in the machine decreases. Once the collision rate has been reduced sufficiently, it is more efficient to start the fill over at a higher collision rate.

3.2 PHENIX

PHENIX, the Pioneering High Energy Nuclear Interaction eXperiment, came online in 2000 along with RHIC and is located at the 8 o'clock interaction region along the RHIC ring. PHENIX is one of the two major RHIC experiments along with STAR, the Solenoidal Tracker At RHIC. The PHENIX detector philosophy differs from STAR in that PHENIX has a small acceptance but very good PID (particle identification) capabilities and very high rate capabilities.

PHENIX's detectors throughout the years include the Drift Chamber (DC), the Pad Chambers (PC), the Ring Imaging Cherenkov (RICH) Detector, the Hadron Blind Detector (HBD), the Time Expansion Chamber (TEC), the Time of Flight (TOF), the Electromagnetic Calorimeter (EMCAL), the Muon Tracker (MuTr), the Muon Identifier (MuID), the Muon Piston Calorimeter (MPC), the Muon Piston Calorimeter Extension (MPC-EX), the Beam-Beam Counter (BBC), the Zero Degree Calorimeter (ZDC), the Forward Calorimeter (FCAL), the Multiplicity and Vertex Detector (MVD), the Reaction Plane Detector (RPD), the Resistive Plate Chambers (RPC), the

Silicon Vertex Detector (VTX), and the Forward Silicon Vertex Detector (FVTX). Figure 3.2 depicts the approximate size and position of each of the detectors that are installed in PHENIX as of 2015.

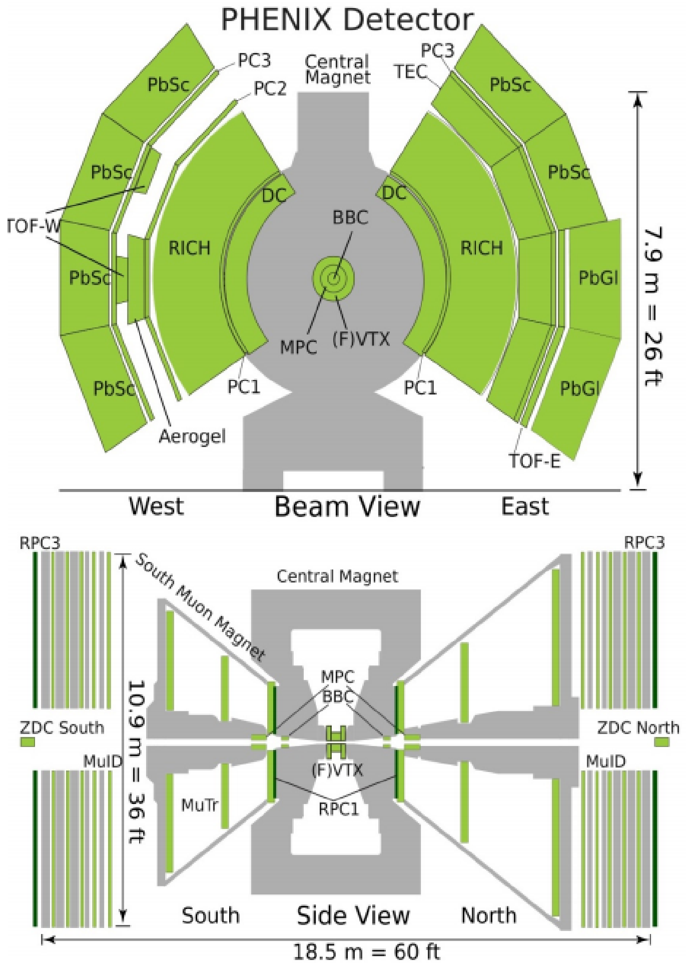

Figure 3.2: A cross section diagram of the PHENIX detector from the incoming beam's perspective (top) and a cross section diagram of the PHENIX detector from the side (bottom). The central arm detectors are not shown in the bottom diagram [21].

For this thesis, the relevant detectors in 2015 are the DC, PC, RICH, BBC, and FVTX. The DC, PC, and RICH are located in the mid-rapidity region relative to the collisions and are a part of what are referred to as the Central Arms (CA) and the BBC and FVTX that are located in the forward (and backward) rapidity region relative to the collisions are a part of what is referred to as the (Forward Arms) [22].

PHENIX makes use of the three powerful magnets in order to bend charged particles' trajectories: the Central Magnet (CM), the North Muon Magnet (MMN), and the South Muon Magnet (MMS).

PHENIX has a state-of-the art Data Acquisition System (DAQ) which is capable of writing 400 MB/s of information to disk. More details about the PHENIX DAQ are found in Section 3.2.8.

For reference, Figure 3.3 depicts the PHENIX coordinate system relative to the RHIC ring. References to the cardinal directions or x, y, or z are defined in relation to this figure.

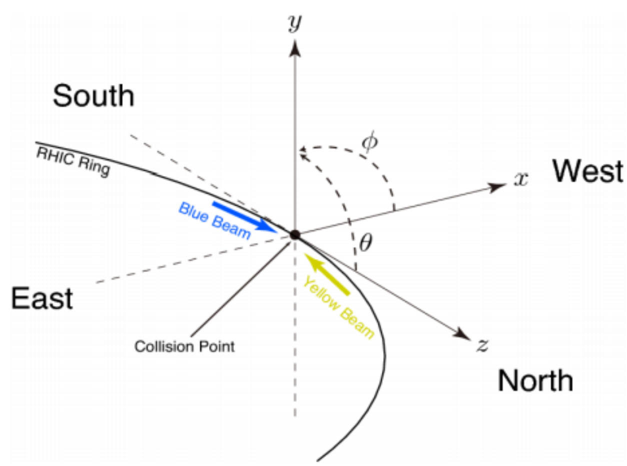

Figure 3.3: The PHENIX coordinate system. The origin is in the middle of the PHENIX detector at the collision point. North and south are parallel to beam axis. East and west are transverse to the beam axis. Central detectors have a west and an east arm on either side of the beam. Forward detectors have a north and a south arm relative to the origin.

3.2.1 PHENIX Magnet System

The CM has two circular coils which can be configured in the same direction (++ or $--$) of the opposite direction ($+-$). The magnets can also be run in the "zero-field" configuration which is used for alignment purposes. Figure 3.4 shows the magnetic field lines and strength produced by the PHENIX magnets. The magnetic field lines at mid-rapidity, $|Z| < 0.3$m on the plot, have a peak strength of $\sim$0.9 T near the beam pipe and extend out to R $\approx$ 2 m, just before the DC.

The right panel of Figure 3.4 depicts the magnetic field strength as a function of distance from the center of PHENIX. For any of the possible CM magnet configurations, the magnetic field strength is very small for $r > 2$ m.

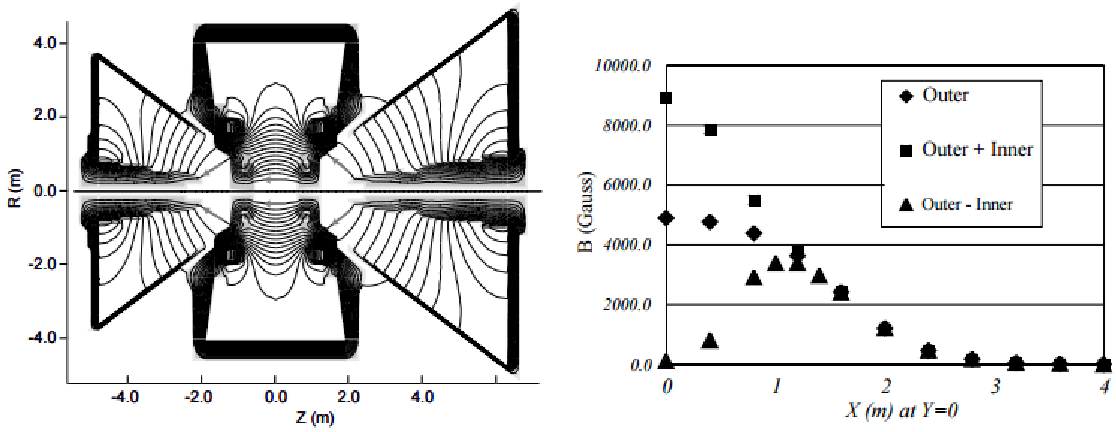

Figure 3.4: PHENIX magnetic field lines from the MMS, CM, and MMN, (left) and the total magnetic field strength from the CM vs the radial distance from the center of PHENIX at $\phi = 0$ X (right) [12].

3.2.2 Beam Beam Counter

The BBC is a forward detector used to determine the event start time, vertex, centrality, and event plane. The BBC is composed of two mirror image arrays, a South and a North Arm, that surround the beam pipe 144 cm on opposite sides of the nominal collision point just behind the Central Magnet, covering $3.0 < |\eta| < 3.9$ and 2π radians in azimuth. Each BBC arm is made of 64 elements each composed of a 3-cm length quartz Cherenkov radiator connected to a 2.5 cm diameter Hamamatsu R6178 mesh dynode PMT (photomultiplier tube), as shown in Figure 3.5. The outer and inner diameters of the BBC, with respect to the beam axis, are 30 cm and 10 cm, respectively.

The BBC is used to mark the event start time for the entire PHENIX detector by averaging the emitted particles arrival time at each BBC arm. The timing difference between each arm

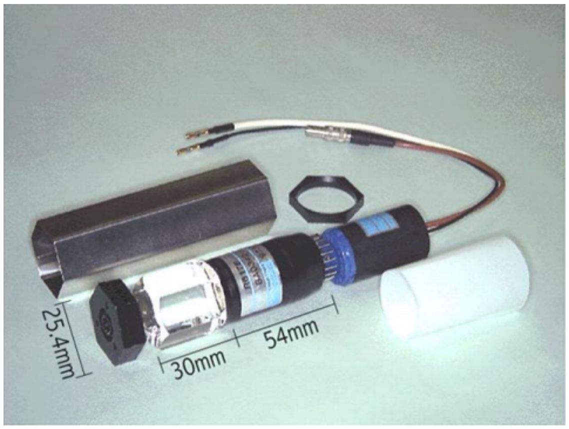

Figure 3.5: Photographs of the BBC detector. The left is of a single detector element consisting of a quartz radiator and a PMT. The right is of one of the BBC arms, consisting of 64 detector elements [22].

provides an estimate of the collision's z-vertex by

$$z = c\frac{T_S - T_N}{2}, \tag{3.1}$$

where T_S, T_N are the particle's average arrival times for each arm and c is the speed of light.

For p+Au collisions at $\sqrt{s_{NN}}$ = 200 GeV, the BBC has a timing resolution of t $\sim$40 ps and a corresponding z-vertex resolution of $\sim$1.0–2.0 cm, depending on the event charged particle multiplicity. A coarser estimate of the vertex is used during triggering, to select events of interest. Specific details about triggers are in Section 3.2.8.

The BBC also provides the centrality classification, as described in Chapter 2, Section 2.1.1, of a collision event in PHENIX. Details of how BBC data is used to compute the centrality are given later in this Chapter in Section 3.2.10.

3.2.3 Forward Vertex Detector

The FVTX is a PHENIX detector upgrade that became operational in 2012 for taking physics data. The FVTX provides charged particle tracking, collision vertex determination, and event plane determination [21]. The FVTX consists of two identical endcaps covering a combined pseudorapidity range of $1 < |\eta| < 3$ and full azimuth coverage. Each endcap has four stations of silicon mini-strip sensors with a pitch of 75 μm arranged in the radial direction around the beam pipe. The basic unit of construction is a wedge that has silicon strip sensors and associated read-out chips. The inner most layer (on each side) of the FVTX has a smaller radius. Figure 3.6 is a photograph of the FVTX disks and an engineering drawing of the FVTX and its support structure. The FVTX is used in this thesis to calculate the event plane.

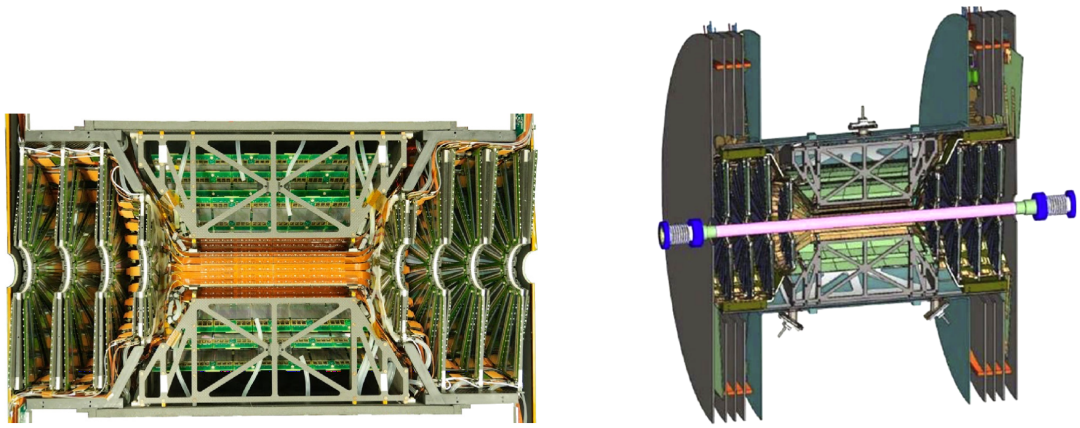

Figure 3.6: A photograph of half of the FVTX. In the cutaway, one sees the half disks on either end of the picture (left) and a schematic of the FVTX at a slightly different angle (right). The FVTX is only 20 cm in the z direction from the PHENIX coordinate system origin (the center of each picture) [21].

3.2.4 Drift Chamber

The DC consists of two gas multi-wire proportional chambers, one located in each arm. The DC is used to measure particle trajectories in the r-ϕ plane. The DC is located ~2 m from the z-axis, placing it in a very small residual magnetic field from the CM. Apart from the VTX, the DC is the first detector encountered by a particle produced at mid-rapidity.

As a charged particle passes through the DC volume, the gases are ionized to create free electrons. These electrons cause a chain reaction of ionizations which are measured by an anode wire. The DC is designed in such a way that the drift velocities of the elections are predicable enough to relate time and position together.

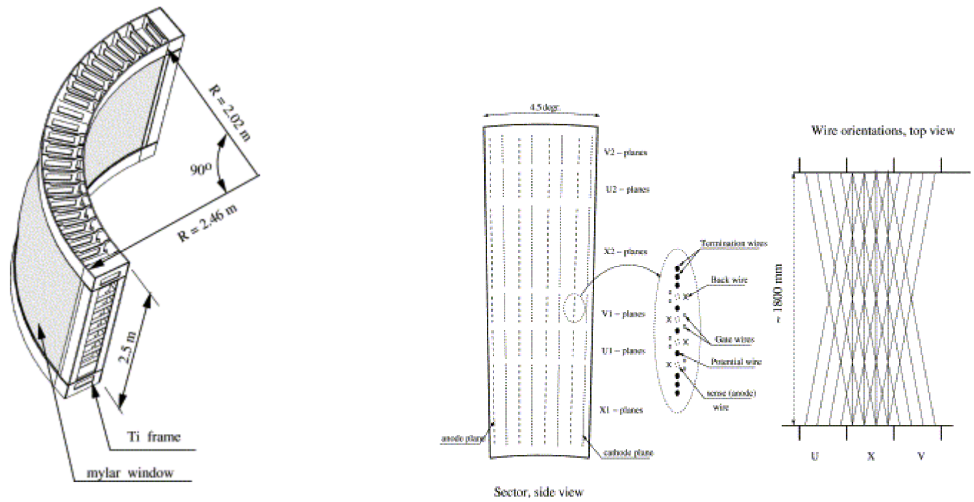

Figure 3.7: A diagram of the DC titanium frame which encloses the detector (left) and a diagram of the X, U, and V wires in the DC (right) [22].

Each identical DC arm is cylindrical in design and covers 2.5 m along the beam direction and is 0.4 m deep (in radius) as seen in the left panel in Figure 3.7. A gas mixture of 50% Argon and 50% Ethane is used in each arm of the DC. Each arm is divided into 20 equal sectors covering 4.5 degrees in ϕ. Each sector contains six types of wire modules stacked radially and labeled X1, U1, V1, X2, U2, V2, respectively, from the inside out. The X wires run parallel to the beam to perform precise ϕ measurements while the U and V wires are set at small angles of about six degrees relative to the X wires to provide information about the z position of the track. A diagram of the wire layout in each sector is shown in the right panel in Figure 3.7. In total, the DC consists of about 6,500 anode wires with 13,000 readout channels. The resolution for a single wire is 165 μm in r-ϕ, a single wire efficiency better than 99%, and a spatial resolution of 2 mm in the z direction.

3.2.5 Pad Chambers

The PCs are multi-wire proportional chambers consisting of three separate layers of detectors measuring precise hit positions in the PHENIX tracking system. The innermost layer, PC1, is located in both the East and West arms immediately outside the DC, providing a measurement of the x, y, z position at the back plane of the DC. The second layer, PC2, is located behind the RICH in the West arm only. The outer layer, PC3, is in both arms and provides a second space point on the straight line trajectories of the tracks through the detector, outside of the CM magnetic field as shown in Figure 3.4. PC1 hits are used as an input to the pattern recognition to reduce the track background.

3.2.6 Ring Imaging Cherenkov Detector

The RICH detector is located immediately behind the PC1 and provides the primary electron identification for PHENIX. The RICH consists of two identical detectors in the CA. Each detector contains 48 mirror panels which focus Cherenkov light onto PMTs. The RICH is filled with radiator gas, is CO_2, for the p+Au running. The RICH provides e/π (electron to pion) discrimination below the π Cherenkov threshold of $\sim$4 GeV/c. Figure 3.8 shows the energy over momentum E/p distribution in Au+Au $\sqrt{s_{NN}} = 200$ GeV collisions. The E comes from the EMCAL and the p comes from the DC tracks. When RICH hits are required in conjunction with DC tracks, a clear electron signal peak can be seen at $E/p = 1.0$, as expected for electrons deposited their full energy in the EMCAL.

3.2.7 Electromagnetic Calorimeter

The EMCAL is the outermost subsystem in the central arms and is designed primarily to measure the energies and positions of photons and electrons. It also plays a key role in particle identification, as well as providing triggering on rare event or interest. Two different EMCAL designs were utilized with 6 sectors based on a lead-scintillator design and 2 sectors based on a lead-glass design. The two different designs were chosen deliberately as each provides advantages and disadvantages; for instance the lead glass has a better energy resolution, while the lead scintillator has better linearity and timing. The EMCAL is not used in this analysis.

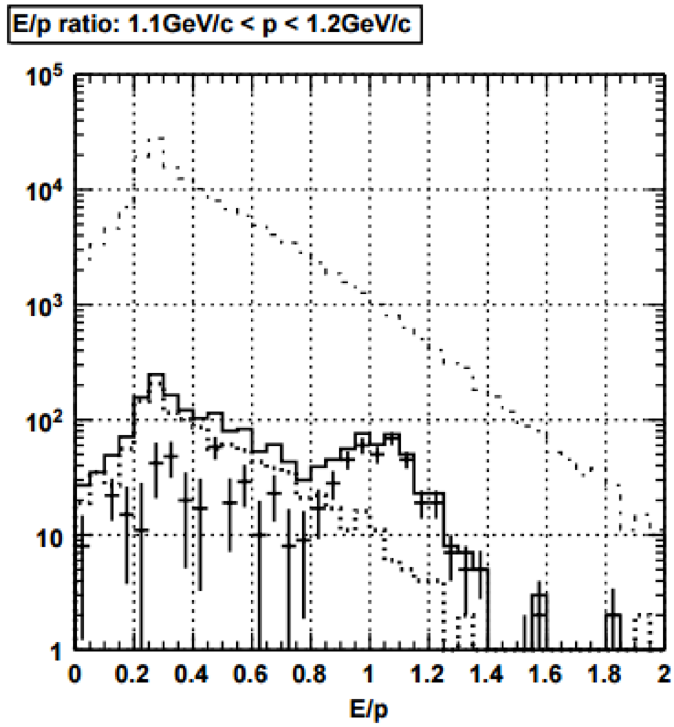

Figure 3.8: Ratio of energy to momentum for all Drift Chamber tracks (dashed-dotted line), and tracks associated with RICH hits (solid line) in Au+Au $\sqrt{s_{NN}} = 200$ GeV collisions. The p range is 1.1 – 1.2 GeV/c [9].

3.2.8 PHENIX Data Acquisition System

PHENIX makes use of a fast DAQ to manage the transfer and collation of hundreds of kB of event data (per event) from over two dozen independent detector subsystems at a rate of over 6 kHz. This amounts to writing to disk hundreds of MB/s, a data writing rate which the PHENIX DAQ consistently achieves for months of constant use.

The collection of a Granule Timing Module (GTM), Front End Modules (FEM), and a Data Collection Modules (DCM) is known as a “granule” and is the minimal combination of DAQ hardware sufficient for data production, as shown in Figure 3.2.8.1. The output data of each detector subsystem is managed by a granule. Pipelined Field Programmable Gate Arrays (FPGA) with carefully controlled dead time are used to calculate the trigger decisions. The FPGAs are fed information from the experiment. Once the FPGAs compute the trigger decision, the trigger signals are monitored by the GTM. If the trigger decision is positive, the GTMs instruct the FEMs to release their data from their buffers and send them to the DCM of their granules. If the decision is negative, the FEMs are instructed to dump the data. Once the FEM is instructed to send its data downstream, it goes to the DCM and then is sent to the Event Builder (EvB).

3.2.8.1 Triggering

PHENIX runs 32 distinct triggers simultaneously. Each of the triggers has a scale down number to control the relative bandwidth each trigger receives. To understand the PHENIX triggers, it is useful to learn about the beam clock.

The PHENIX trigger is tied to the clock of the blue beam, one of the two counter circulating rings of which RHIC is comprised. The clock rate is fixed at 9.38 MHz and is tied to the rate at which RHIC overlaps bunches of ions in the interaction regions. Every time a bunch of ions from the blue ring overlap with a bunch of ions from the yellow ring, there is a blue clock trigger. This clock is stable by necessity of the precision required to run a complex accelerator like RHIC.

The trigger that is used in this analysis is the minimum bias trigger. As the name suggests, the trigger seeks to mark the detection of an ion collision while reducing to a minimum the bias to the type of the collision. To achieve this, data from the BBC are used. Although what constitutes a minimum observation varies with collision species, the BBC minimum bias trigger is generally defined as >0 PMTs in each arm above threshold. Not only is this condition a good indication that a ion collision occurred, it is also the minimum information necessary to calculate the collision vertex position using the BBC. The vertex information is important because it is used to select collisions which occur in the narrow range of acceptance of the current PHENIX detector configuration. This range is -10 cm $< z <$ 10 cm. For completeness, PHENIX takes BBC minimum bias triggers with z vertex cuts of 30 cm, 10 cm, and with no vertex cut. The collection of all these triggers is what is considered to be the PHENIX minimum bias trigger.

In Run 15, a high multiplicity trigger was implemented to enhance event statistics for events producing the largest number of particles (i.e. the most central, violent collisions). This trigger was given a large fraction of the bandwidth and consisted of requiring at least 35 out of 64 PMTs in the south arm (Au-going direction) of the BBC. More details about this trigger are located in Section 3.2.9.

Table 3.1: An example 2015 p+Au at $\sqrt{s_{NN}}$ = 200 GeV trigger configuration and parameters. A trigger's scale down number reduces its rate by 1/(1+scale down).

$Trigger\,Name$	$Scale\,down$	$Trigger\,rate$	$Vertex\,cut$	$Part\,of\,minimumbias$
$Clock$	196077	$45Hz$	N/A	no
$BBC(>0\,PMTs)\,narrowvtx$	100	$695Hz$	$10cm$	yes
$BBC(>0\,PMTs)$	2083	$88Hz$	$30cm$	yes
$BBC(>0\,PMTs)\,novertex$	3959	$94Hz$	$no\,cut$	yes
$BBC(>35\,PMTs)$	1	$1640Hz$	$10cm$	no

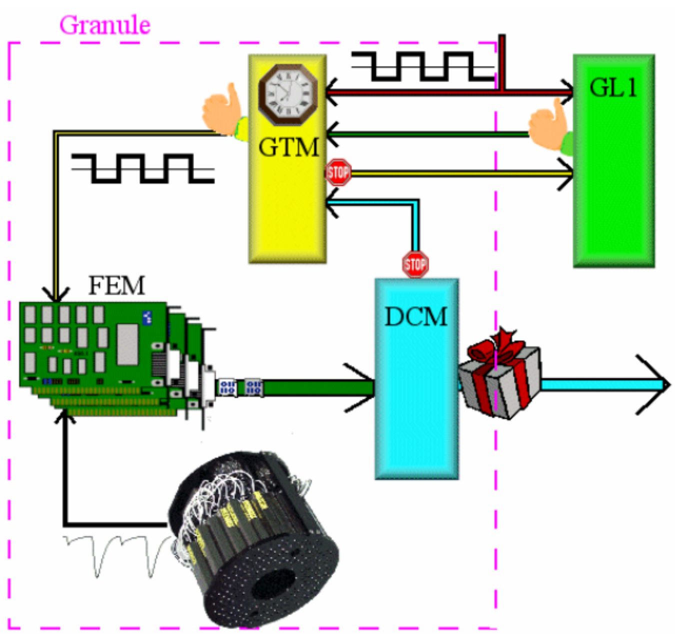

Figure 3.9: Diagram of a granule. Granules are the building blocks of the PHENIX DAQ. Each detector subsystem has at least one granule.

3.2.8.2 Event Builder

Following the PHENIX DAQ data path, after a positive trigger decision has been sent to each of the granules, the granules' data packets are sent from that granule's FEM to the DCM and then to the event builder. It is the event builder's job to associate each granule's data packet from the same collision event into one bundle of data known as an event. The event builder consists of Sub Event Buffers (SEB), Assembly Trigger Processors (ATP), an Event Builder Controller (EBC), and a Gigabit Ethernet Switch for the communication management. The EvB transfers the data to long-term storage at the RHIC Computing Facility. Figure 3.10 shows a diagram for how these components are connected.

Granules send the data packets to the specific SEB assigned to that granule. The EBC receives global trigger information and assigns each ATP a specific collision event. The ATP then requests the data from all of the SEBs for the specific event assigned to it by the EBC. Once the ATP is successful, it writes the assembled event to disk and the EBC instructs the SEBs to flush the buffer for that event.

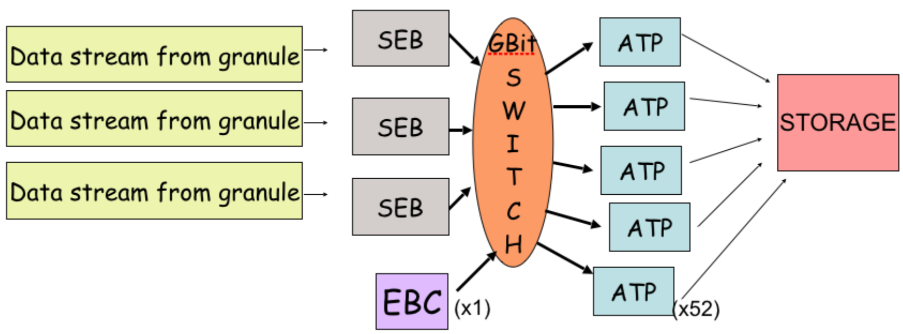

Figure 3.10: Diagram of the event builder.

3.2.9 Run 15

Run 15 is the RHIC running period in the year 2015, which marks the fifteenth in consecutive years of RHIC running since the year 2000. Run 15 began in January 2015 and ended in June of 2015. There were approximately eleven weeks of research viable, polarized p+p collisions at $\sqrt{s}$ = 200 GeV, approximately five weeks of research viable polarized p+Au collisions at $\sqrt{s_{NN}}$ = 200 GeV, and approximately one week of research viable p+Al collisions $\sqrt{s_{NN}}$ = 200 GeV. Of interest to this thesis are the p+p and p+Au datasets.

Table 3.2: Some relevant RHIC parameters from Run 15.

Collision Species	p+p	p+Au	units
Total Particle Energy	100.2	103.9 + 100.0	GeV/nucleon
Ions per Bunch	225	225 + 1.6	number $\times 10^9$
Number of Bunches	111	111	number
Luminosity Average Per Fill	63×10^{30}	45×10^{28}	$cm^{-2}s^{-1}$
Total Delivered Luminosity	382	1.27	pb^{-1}
Average Fill Lifetime	8	7	hours

In addition to providing the minimum bias as trigger for Run 15, the BBC was used to implement a high-multiplicity trigger in order to enhance the amount of the top 5% highest multiplicity events. The high-multiplicity trigger requires 35 of the 64 BBC south arm. PMTs to be above threshold in a given event to be satisfied. The relevant BBC arm for p+Au is the south arm since that is the Au-going direction so the multiplicity is much higher in the south arm. The central trigger enhancement can be seen in Figure 3.11.

3.2.9.1 Beam Collision Geometry

For the 2015 p+Au collisions at $\sqrt{s_{NN}}$ = 200 GeV running, The RHIC's blue and yellow beams were not in perfect accordance to the PHENIX coordinate system. This was manifested in two separate ways. First of all, the collision vertex is significantly offset from the z-axis to which all of the PHENIX detectors are aligned. This is a typical situation in PHENIX datasets but it must be addressed. The other effect, and the more significant of the two, comes from the fact that the beams are colliding at an angle of 3.6 milli-radians in the x-z plane, as illustrated in Figure 3.12.

The reason for this is because of the accelerator ring magnet requirements for running p+Au at $\sqrt{s_{NN}}$ = 200 GeV at RHIC. It is highly desirable to have the beams at equal energy per nucleon, and since the proton and the Au have different Z/A ratios, the magnets require different settings to control the beams. The final delta x magnet constrains both beams and moves them to cross at the interaction region in the middle of PHENIX. The beam angle is needed to offset the beams in the delta x magnet field [2].

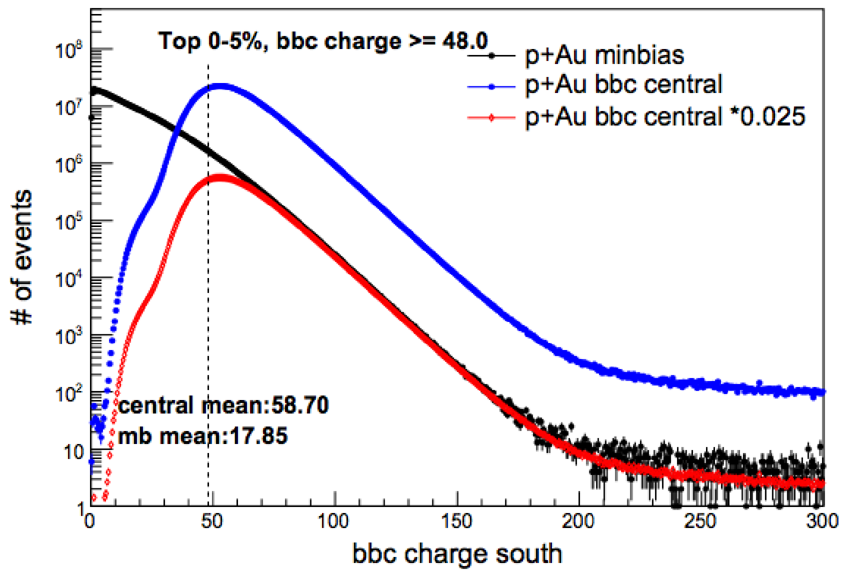

Figure 3.11: The distribution of BBC charges in p+Au at $\sqrt{s_{NN}}$ 200 GeV events for different triggers. The black curve is the distribution of charges for the minimum bias trigger. The blue and red curves are the distributions of charges for the high multiplicity trigger. The red curve being scaled by a factor of 1/40 to show agreement with the black curve. The definition of the top 5% more central events are BBC south charges >= 48.0. The plot shows the large enhancement of the number of 0-5% centrality events that are gained using the high multiplicity trigger compared to the number of 0-5% centrality from the minimum bias trigger alone.

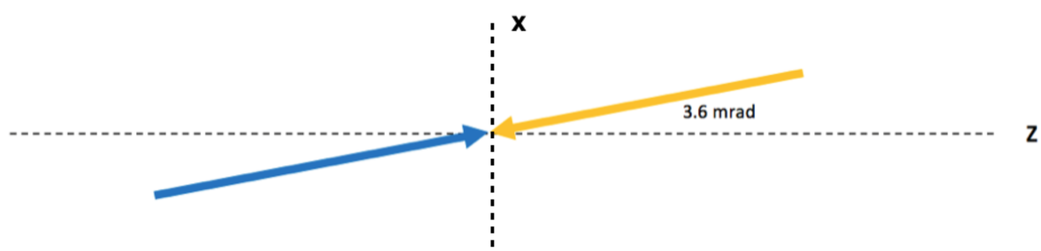

Figure 3.12: A vector diagram illustrating the yellow and blue beam angle confirmation relative to the PHENIX coordinate system.

The collision vertex in x and y is known as the beam center. The beam center varies over the course of data taking but its values on average are $(x, y) = (0.206, 0.065)(cm)$. The distribution of z-vertices from collision events can be see in Figure 3.13. Due to the fact that the beams are colliding at an angle in the x-z plane, the x-component of the beam center will have a z-vertex dependence with a slope of -0.0036 cm of x per 1 cm of z. Apart from how the beam angle effects the beam center values, it also violates the expectation of a uniform ϕ distribution of particles with respect to PHENIX detectors. PHENIX detectors are designed and aligned, with respect to the PHENIX coordinate system, with the expectation of geometric symmetry. A significant beam collision angle with respect to PHENIX detectors would be equivalent to PHENIX detectors being tilted which would violate geometric symmetry. The physics analysis described in this thesis is sensitive to these beam geometry effects. A discussion on how to account for these effects will be in Chapter 4.

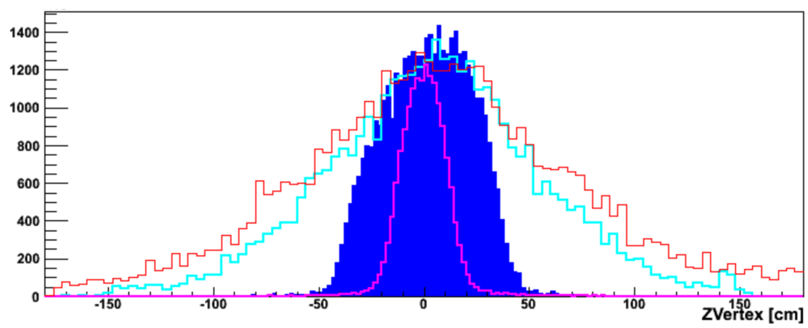

Figure 3.13: The BBC z-vertex distribution in a typical p+Au run for different triggers a described in Table 3.1. The teal curve is the BBC(>0 PMTs) novertex trigger, the blue is the BBC(>0 PMTs), and the magneta is the BBC(>0 PMTs) narrowvertex.

3.2.10 Centrality Determination

The centrality determination is done by adding up all BBC South (BBCs) (Au-going direction) PMT charges for every event and then splitting up that distribution into equivalent centrality bins. This procedure, which is the same used for d+Au, as documented in ref [5], is used to associate a centrality bin with number of binary collisions from Monte Carlo Glauber (MC-Glauber), as discussed in Chapter 2 Section 2.3.1.1. An example of such MC-Glauber event for d+Au is seen in Figure 3.14.

In this procedure, the total BBC charge is assumed to be proportional to the number of

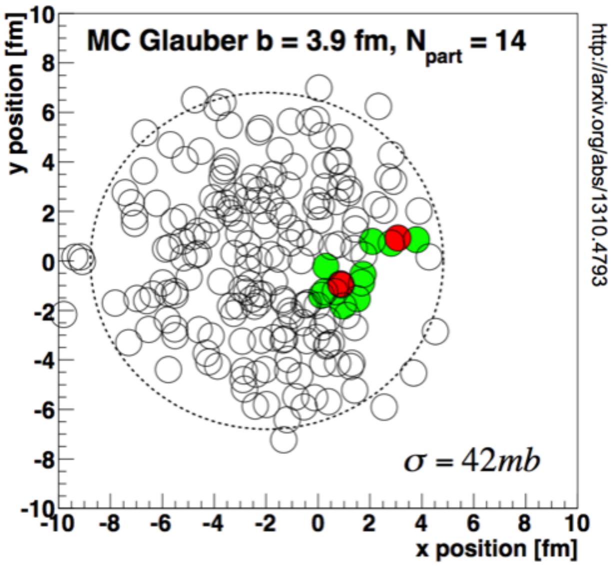

Figure 3.14: A Monte Carlo Glauber d+Au event display. Each circle is a nucleon and filled circles are nucleons with at least one collision. The red nucleons are from the projectile (deuteron) and the green nucleons are participants from the target (gold) [5].

binary collisions in a p+Au collision. Fluctuations are described probabilistically via the Negative Binomial Distribution (NBD) as defined:

$$\mathrm{NBD}(x;\mu,\kappa) = \left(1+\frac{\mu}{\kappa}\right)\frac{(\kappa+x-1)!}{x!(\kappa-1)!}\left(\frac{\mu}{\mu+\kappa}\right)^x \tag{3.2}$$

where μ and κ are the mean and positive exponent parameters. The NBD was chosen for this situation due to the linear scaling of the NBD parameters, i.e. randomly sampling from nNBD(μ,κ) becomes NBD($n\mu$,$n\kappa$). We fold the MC-Glauber with the NBD such that the charge distribution is described as

$$P(x) = \sum_{n=1}^{N_{COL}\max} \mathrm{Gl}(n) \times \mathrm{NBD}(x;n\mu;n\kappa), \tag{3.3}$$

where x is the BBCs charge and Gl(n) is the event normalized Glauber distribution [5]. The two parameters μ and κ are fit to the experimental BBCs charge distribution, as shown in Figure 3.15. This figure shows good agreement between the data and the MC-Glauber + NBD fit. The best fit NBD parameters are $\mu = 3.14$, $\kappa = 0.47$.

There is a deviation at small BBCs charge because the minimum bias trigger is inefficient due to the fact that a PMT must be hit in both the BBC South and North. The bottom panel of Figure 3.15 is the ratio of the data to the theory curve shows that the agreement is good at a charge of 10 and greater. This ratio is fit to determine the minimum bias trigger efficiency as it “turns on.” This fit has good agreement with the turn-on curve which can be integrated to determine that the minimum bias trigger is 84% ± 4% efficient. By combining the theoretically determined p+Au cross section with the 84% trigger efficiency, we determine the the total inelastic p+Au cross section $\sigma = 1.76$ barn. Thus, centrality is defined as a percentage of the total inelastic cross section.

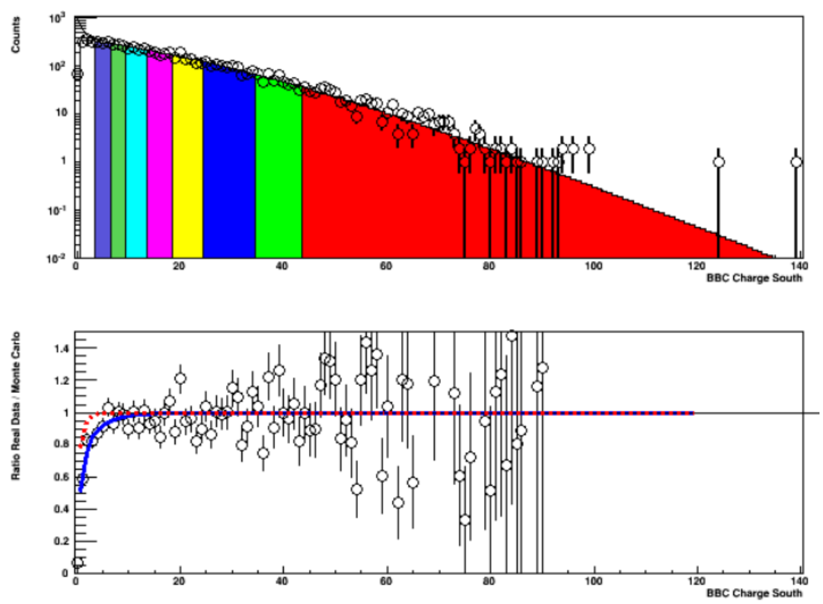

Figure 3.15: Real data for BBCs charge shown as open circles and MC-Glauber + NBD (top). The colors correspond to the various percentiles relative to the total inelastic p+Au cross section, from right to left: 0–5%, 5–10%, 10–20%, 20–30%, 30–40%, 40–50%, 50–60%, 60-70%, and 70-84%. The blue and red curves correspond to the minimum bias trigger efficiency in all inelastic collisions and inelastic collisions producing a particle at mid-rapidity, respectively (bottom).

Chapter 4

Analysis

This chapter contains an extensive discussion of the data analysis techniques in the physics measurement. First we describe the building blocks of the v_2 measurement, then we examine the event plane analysis techniques and the sources systematic uncertainty.

4.1 The Building Blocks of the Measurement

Prior to any analysis, the raw data collected by various PHENIX subsystems must be reconstructed into well-defined software objects encapsulating the physical properties of the particles that traversed the detector. Although we have already discussed the subsystems used in this analysis in Chapter 3, this section provides in-depth information on central arm tracks, FVTX clusters, and BBC photomultiplier tubes (PMTs), and the physics variables they contain. Figure 4.1 displays the coordinate system for PHENIX and the particle parameters that are in relation to it.

4.1.1 Central Arm Tracks

Central Arm (CA) tracks are the representation of charged particles emitted from the heavy ion collision, which are detected by detectors in the PHENIX central arms. There are two central arms, each one covering an acceptance of $\eta < |0.35|$ and $\frac{\pi}{2}$ in pseudorapidity and azimuth, respectively. The relevant detectors for this analysis include the Drift Chamber (DC), the Pad Chambers (PC) and the Ring Imaging Cerenkov (RICH) detector. As discussed in Chapter 3, the DC provides momentum information; the PC provide track quality metrics; and the RICH provides

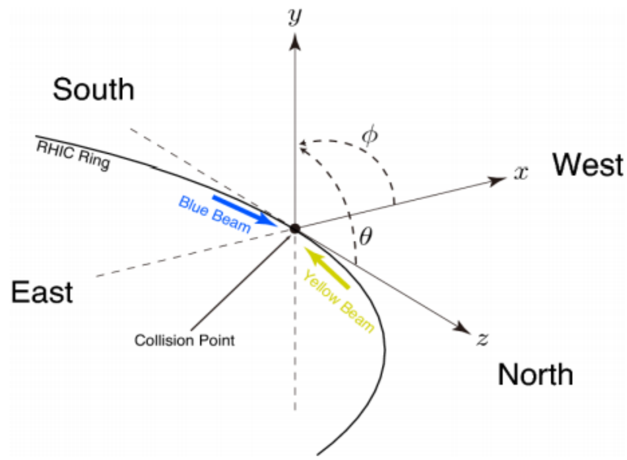

Figure 4.1: Reference coordinate system for the PHENIX detector. The origin is set at the collision point, around which the detector is centered. The beam runs parallel to the (longitudinal) $z-$axis, where the direction of positive z is defined as **north**. The **east** and **west** directions are defined as perpendicular to the longitudinal direction, where the direction of positive x is defined as west.

electron identification.

The main physical parameter of CA tracks is the momentum vector $\vec{p} = (p_x, p_y, p_z)$ of the particles, defined at the collision vertex. This analysis uses tracks with momentum $0.02 < |p_T| < 3.5$ GeV/c, a p_T range where the momentum resolution is good, as shown in the left panel of Figure 4.2. The right panel of Figure 4.2 shows the p_T distribution of CA tracks up to 10 GeV/c: a smooth linearly falling distribution on a log scale with a small number of fake tracks at high p_T. The azimuthal angle and pseudorapidity of the track are calculated from the components of its momentum vector, as follows:

$$\phi = \arctan(\frac{p_y}{p_x}), \tag{4.1}$$

$$\eta = ArcSinH(\frac{p_z}{p_T}). \tag{4.2}$$

In addition to momentum, CA tracks provide a number of other parameters that can be used to ensure the quality of tracks and isolate a sample corresponding to charged hadrons. These include zed in the DC, dϕ and dz in the PC, $n0$ in the RICH, and the general track quality calculated from DC and PC information. These variables are defined as follows:

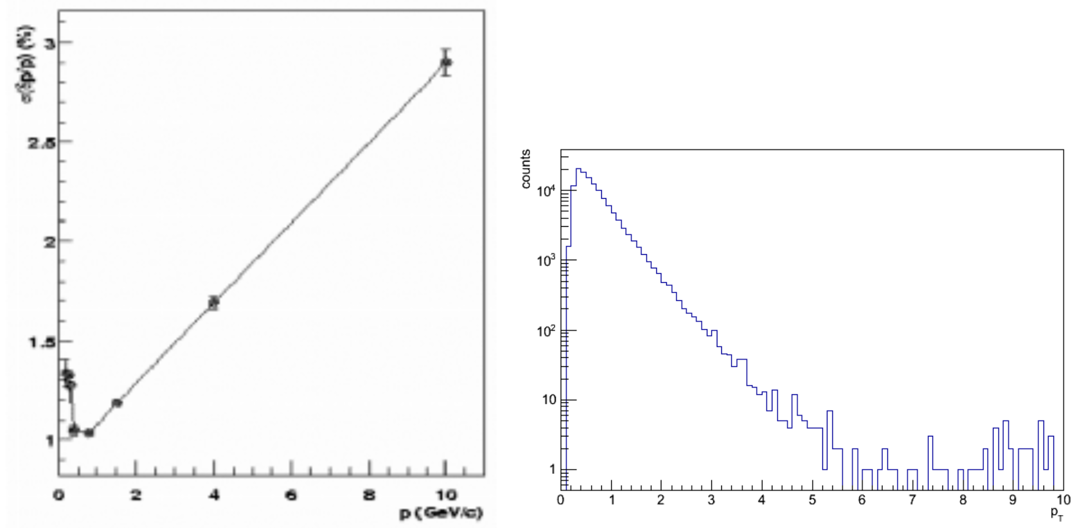

Figure 4.2: Momentum resolution σ_p/p as a function of the reconstructed track momentum, p for simulated single-particle events [1] (left) and the transverse momentum p_T distribution of CA tracks in p+Au events at $\sqrt{s_{NN}}$ = 200 GeV. High p_T tracks (p_T > 5 GeV/c)observed correspond to unsubtracted background (right).

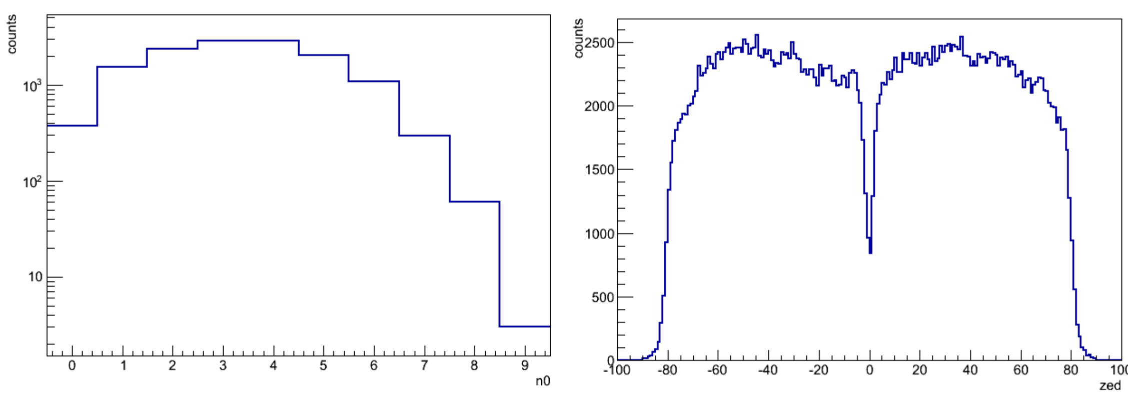

Figure 4.3: The distribution of (left) $n0$, i.e., the number of PMTs fired in the RICH, and (right) zed, i.e., the longitudinal position of tracks in the DC, for CA tracks in 0-5% central p+Au events at $\sqrt{s_{NN}}$ = 200 GeV. The structure observed in the zed distribution corresponds to a gap in the detector acceptance.

- The zed variable corresponds to the longitudinal position of the track in the DC, as shown in Fig. 4.3 (right panel)

- The dϕ and dz variables quantify the distance between a track projection and its associated hits in the PC. In order to make standard cuts on these variables, their distribution must be calibrated to a standard Gaussian in a procedure known as sigmalization, described in subsection 4.1.1.1

- The $n0$ variable, used for electron identification, corresponds to the the number of PMTs fired in the RICH that match the DC track projection, as shown in Fig. 4.3
- The track quality category, which is based on the PC1 and DC wire hits used as well as CD wire momentum information, defined in Tables 4.1 and 4.2

Table 4.1: Quality categorization of CA tracks, as a function of PC1 and DC wire hits. The quality parameters used in this analysis are 31 and 63.

Quality	PC1 found	PC1 unique	UV found	UV unique
17,18,19	1	0	0	0
21,22,23	1	0	1	0
29,30,31	1	0	1	1
49,50,51	1	1	1	0
61,62,63	1	1	1	1

Table 4.2: Quality categorization of CA tracks, as a function of DC wire momentum information. The quality parameters used in this analysis are 31 and 63.

Quality	X1 used	X2 used
17,21,29,49,61	1	0
18,22,30,50,62	0	1
19,23,31,51,63	1	1

The quality cuts Table 4.3 summarizes the CA track cuts used in this analysis to reduce the track background.

4.1.1.1 Sigmalization of PC Variables

The goal of PC variables dϕ and dz is to provide criteria to determine if the ϕ orientation and z-direction of the track match between the third layer of the PC and the DC. The sigmalization

Table 4.3: CA Track cuts for each relevant variable and their units.

variable	cuts	units
p	$0.02 < p < 10.0$	GeV/c
zed	$\|zed\|$ <75	cm
PC3 dϕ	$\|d\phi\|$ <2.0	radians $\times 10^9$
PC3 dz	$\|dz\|$ <2.0	cm
n0	n0<=0	count
quality	63 or 31	N/A

is done in the minimum bias sample and is valid for all other centrality selections. We did the sigmalization procedure for tracks in different transverse momentum bins, separately in the east and west arms, and for positive and negative particles. The dϕ and dz distributions were fitted with a double-Gaussian function and then the parameters were interpolated as a function of p_T . Fig. 4.1.1.1 a) shows a fit to the sigmalized dϕ distribution, and Fig. 4.1.1.1 b) shows a fit to the sigmalized dz distribution for tracks with $1.0 < p_T < 1.1$ (GeV/c) in both the west and east arms as well as both positively and negatively charged particles. Then we fit the signal Gaussian mean and sigma to a polynomial function. Once these variables had been sigmalized, we selected only the tracks within a $\pm 2\sigma$ cut.

4.1.2 FVTX Clusters

The FVTX consists of four silicon layers in the north and south directions, covering an acceptance of $1 < |\eta| < 3$ and spanning the full azimuth. FVTX clusters correspond to the spatial location where charged particles hit one of the silicon layers. Each cluster is expected to correspond to a single charged particle in the case of p+Au collisions, because of the low multiplicity relative to Au+Au collisions. These clusters have a spatial resolution in r and ϕ of 50 μm and 0.14 radians, and have an RMS along the z-direction that corresponds to the width of an FVTX layer, of $\frac{200}{\sqrt{12}}$ μm [21]. Due to the p+Au collision system's inherent asymmetry, the majority of particles are produced in Au-going (i.e., south) direction. Taking into account this asymmetry, only the clusters from the south arm are used for calculations in this analysis. In a typical 0–5% centrality event,

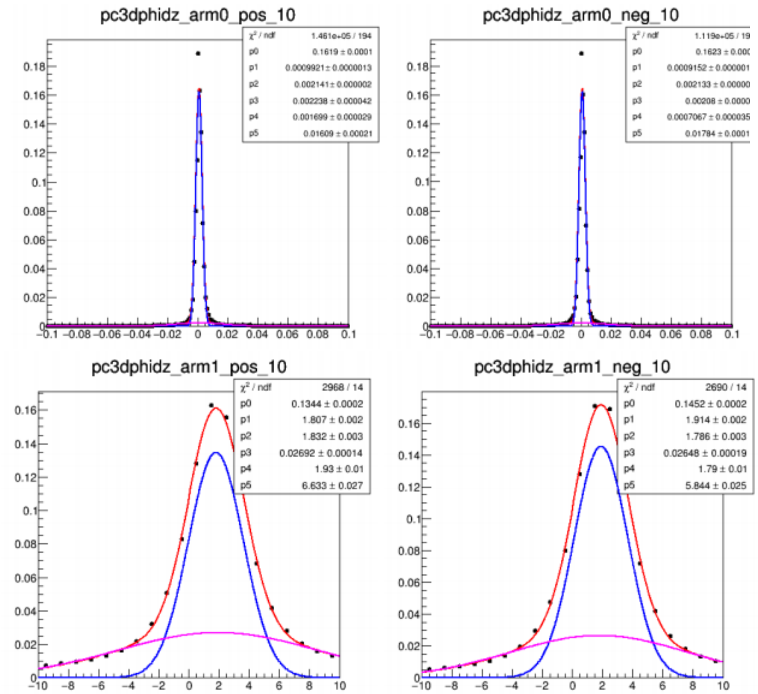

Figure 4.4: The top plots show the PC3 matching dϕ fit in range $1.0 < pT < 1.1$ (GeV/c). The blue and pink lines are single Gaussian fits to the signal and background, respectively, which are combined in the red line. The bottom plots show the result of the dz sigmalization, done in the same way as for dϕ.

there are on average 1500 FVTX clusters in the south arm alone. Average hit distributions are shown in Figure 4.5.

4.1.3 BBC PMTs

The BBC provides information on the position, time of arrival, and number of charged particles that hit the BBC's quartz radiator material. The BBC acceptance is $3.1 < |\eta| < 3.9$ and spans the full azimuth. The resolution of the detector in x and y is 5 cm, corresponding to the diameter of a BBC PMT. In addition to spatial information, the BBC provides charge information, calibrated so that a value of 1.0 corresponds to a single charged particle hitting the detector (i.e. one minimum ionizing particle traversing the quartz). Figure 4.6 shows the layout of the PMTs for the BBC. As discussed in section **??**, the information regarding arrival time and particle charge

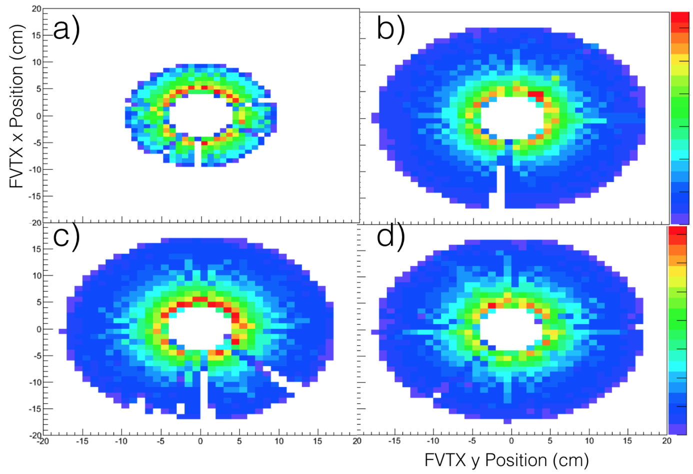

Figure 4.5: Distribution of FVTX clusters in x and y for layers 1, 2, 3, and 4 for panels a), b), c), and d), respectively. The color scale corresponds to the number of counts.

can be used to calculate the z-vertex of the collision.

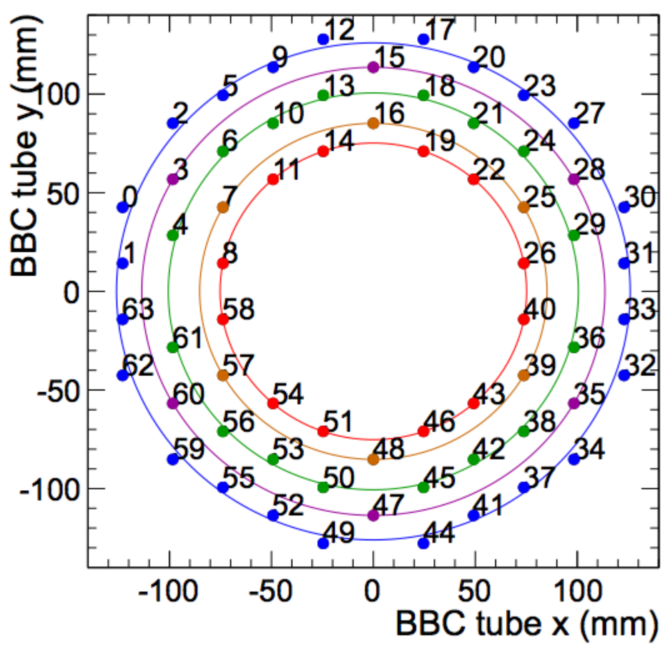

Figure 4.6: Diagram showing the positions of the PMTs for the BBC-south detector. Rings shown with the same color indicate PMTs at an approximate common radius.

4.2 The Event Plane Method

Some details of the event plane were given in Chapter 2 Section 2.2.4. The goal of this thesis is to measure v_2, which is related to collective behavior as evidenced by correlations among particles. These correlations exist relative to the orientation of the collision. The event plane method measures the azimuthal anisotropy in final state particles. The event plane method uses final state particles to calculate the event plane angle from the data. A different set of final state particles are used to define the event plane in the FVTX or BBC and measure the v_2 in the CA.

An event plane angle is defined for each harmonic, and is denoted as Ψ_n where n is the harmonic number. The definition for Ψ_n is related to the calculation of the Q-vector. For an event with N particles, define the flow vector $\vec{Q}$ as follows:

$$Q_x = \sum_{i=1}^{N}(w_i * \cos(n * \phi_i)) \tag{4.3}$$

$$Q_y = \sum_{i=1}^{N}(w_i * \sin(n * \phi_i)) \tag{4.4}$$

$$Q_w = \sum_{i=1}^{N}(w_i) \tag{4.5}$$

where i is the ith particle in the event, ϕ_i is the azimuthal angle of the particle, w_i is the weight factor, and n is the harmonic number. We define the nth order event plane as $\Psi_n = \arctan\left(\frac{Q_y}{Q_x}\right)$.

Once the event plane has been calculated, the flow harmonics (v_n) are defined as

$$v_n = \frac{\langle\langle\cos(n(\phi - \Psi_n))\rangle\rangle}{Res(\Psi_n)}, \tag{4.6}$$

where $\langle\langle\rangle\rangle$ indicates that $\cos(2\phi - \psi)$ is averaged over all particles in the same event, and the resulting v_2 must be averaged over many events [44]. Note, the event plane angle and the Q-vector are defined at the event level.

As discussed in Chapter 2, Section 2.2.4, the event plane angle is a measurement which attempts to correspond to the physical participant plane angle. Thus, the event plane is an imperfect representation of the reaction plane and thus needs to be corrected. This correction is known as the event plane resolution $Res(\Psi_n)$, and is calculated using the 3-subevent method. It is important to note the the set of particles used to calculate Ψ_n and ϕ must be different in order to avoid autocorrelations. This is usually done by imposing a large η gap (usually at least a half of a unit of pseudorapidity)between the two particle sets.

For this analysis, the event plane is calculated separately for each of the forward detectors mentioned above, i.e., the BBC and the FVTX. We only use the south (Au-going) side of each detector, referred to here as the BBCS and the FVTXS. For the FVTXS, the Q-vector is calculated in each event as

$$Q_x = \sum_{i=1}^{N_{\text{cluster}}} (\cos(n\phi_i)) \tag{4.7}$$

$$Q_y = \sum_{i=1}^{N_{\text{cluster}}} (\sin(n\phi_i)) \tag{4.8}$$

$$\phi_i = \arctan\left(\frac{y^i_{\text{cluster}}}{x^i_{\text{cluster}}}\right) \tag{4.9}$$

where N_{cluster} is the number FVTXS clusters in that event and $Clus^i$ are the x and y components of the ith FVTXS Cluster in that event. At this point, this Q-vector is calculated with no cluster dependent weight factor because each cluster is taken to be the representation of one particle.

For the BBCS, the Q-vector is calculated in each event as

$$Q_x = \sum_{i=1}^{N_{\text{PMT}}} (w_i \cos(n\phi_i)) \tag{4.10}$$

$$Q_y = \sum_{i=1}^{N_{\text{PMT}}} (w_i \sin(n\phi_i)) \tag{4.11}$$

$$Q_w = \sum_{i=1}^{N_{\text{PMT}}} (w_i) \tag{4.12}$$

$$\phi_i = \arctan\left(\frac{y^i_{\text{PMT}}}{x^i_{\text{PMT}}}\right) \tag{4.13}$$

where w_i is the scaled charge collected on the PMT and N_{PMT} is the number of PMTs that fired (above threshold) in each event.

Finally, the v_n are calculated using a combination of the BBCS or FVTX Q-vectors and the

CA tracks as

$$v_n = \frac{\left\langle\left\langle \cos(n(\phi^{CA} - \Psi_n^{BBCS,FVTXS}))\right\rangle\right\rangle}{Res(\Psi_n^{BBCS,FVTXS})}. \tag{4.14}$$

In this analysis, we are concerned only with measuring the second-order harmonic v_2.

4.2.1 Event Plane Resolution Calculation

As mentioned above, the event plane resolution is calculated using the standard 3-subevent method [44]. The strategy of this method is to measure Ψ_2 with three different detectors in the same event, and then algebraically . The event plane resolution is defined as

$$Res(\Psi_2^A) = \sqrt{\frac{\left\langle\cos(2(\Psi_2^A - \Psi_2^B))\right\rangle\left\langle\cos(2(\Psi_2^A - \Psi_2^C))\right\rangle}{\left\langle\cos(2(\Psi_2^B - \Psi_2^C))\right\rangle}}, \tag{4.15}$$

where A,B, and C are three detectors measuring the same event. Here, the term "subevent" refers to the specific subset of particles measured by a given detector [44].

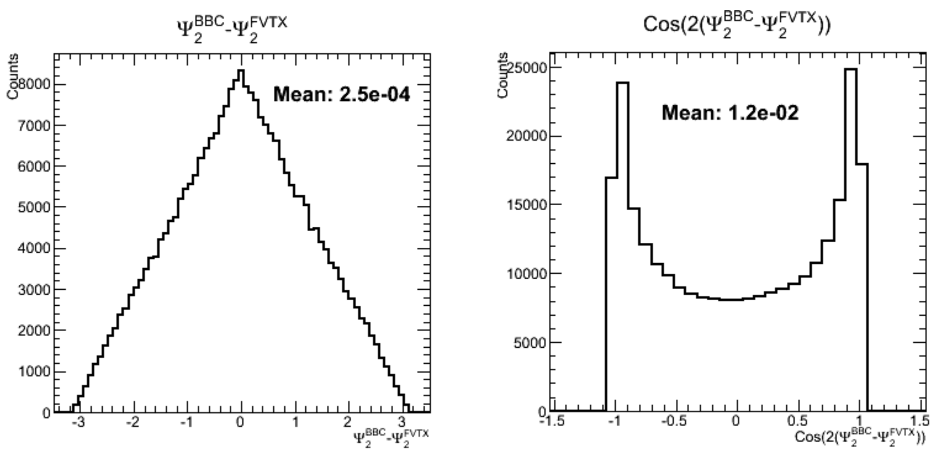

Figure 4.7: Intermediate steps involved in calculating the event resolution. Raw difference between the event plane angles for two different detectors (left). This distribution is triangular because it is the result the cross-correlation of two nearly uniform distributions, Ψ_2^{FVTXS} and Ψ_2^{BBCS}. The cosine of two times the difference between the two event plane angles. The average of this distribution is used in Equation 4.15 (right).

In this analysis, the three detectors used to provide the required three subevents are the FVTX-south, the BBC-south, and the CA, which span pseudorapidity acceptances of $-3 < \eta < -1$, $-3.9 < \eta < 3.1$, and $|\eta| < 0.35$, respectively. Figure 4.9 shows the event-by-event relative difference of Ψ_2^{BBCS} and Ψ_2^{FVTXS}. Unlike the BBCS and the FVTXS, the CA detector does not have full azimuthal acceptance coverage. Therefore, the event plane angle cannot be reliably calculated with this detector for events whose event plane points outside of the acceptance. In order to solve this problem, we calculate the event plane resolution using a different, yet mathematically equivalent formulation that does not make use of Ψ_{CA}, as given below:

$$Res(\Psi_n^A) = \sqrt{\frac{\langle\langle\cos(n(\Psi_n^A - \phi^{CA}))\rangle\rangle\, \langle\cos(n(\Psi_n^A - \Psi_n^C))\rangle}{\langle\langle\cos(n(\phi^{CA} - \Psi_n^C))\rangle\rangle}}, \tag{4.16}$$

where there is a double average over each CA track and each event.

Table 4.4: The event plane angle resolutions for the FVTXS and the BBCS for the second and third order harmonics.

Detector	$n = 2$	$n = 3$
FVTXS	0.216	0.010
BBCS	0.052	0.010

4.2.2 Event Plane Flattening Calibration

In order for the event plane to be useful in making a v_n measurement, the event plane angle must be calibrated such that its distribution is uniform. For the event plane method, a physical assumption is made that the true distribution of Ψ_n angles will be uniform since physically there is no preferred orientation of the collision. If the measured Ψ_n distribution is not flat, we attribute that behavior to variations in the efficiency of detecting charged particles as a function of ϕ. Thus, the event plane calibration procedure seeks to correct for these non-uniformities in acceptance, and restore the Ψ_n distribution to the physical expectation of uniformity. We employ a procedure to re-center and flatten the measured non-uniform Ψ_n distribution.

Figure 4.2.2 shows and example Ψ_2 distributions for the BBCS at the different stages of the calibration. The raw Ψ_2 (shown in red) has a significant deviation from uniformity which needs to be corrected. The flattening calibration attempts to correct for this lack of uniformity by shifting the Ψ_2 value of each individual event by an amount corresponding to the deviation of the overall distribution for all events. Although this procedure results in a uniform Ψ_2 distribution, applying too large of a correction arising from an exceedingly distorted initial distribution can lead to systematic effects on the v_2 measurement, which will be discussed in the next section. Therefore, it is important to address any systematic effects that would affect the uniformity of the Ψ_2 distribution.

The flattening calibration requires two steps to completely flatten the Ψ_n distribution. The first step of the calibration is to re-center the mean of the raw Ψ_n distribution to be at 0.0 radians and to resize the RMS. The second step is to Fourier transform the re-centered distribution and use the transformation to shift the Ψ_n values to a uniform distribution. With flattening, each Ψ_n is transformed to $\Psi_n + \Delta\Psi_n$. $\Delta\Psi_n$ is defined as

$$\Delta\Psi_n = \sum_{i=1}^{N} \left(\frac{2}{i} \left(\sin(i\Psi) F_i^{\cos}(f(\Psi_n)) - \cos(i\Psi) F_i^{\sin}(f(\Psi_n)) \right) \right), \tag{4.17}$$

where N is the number of components, $F_i^{\cos}(f(x))$ is the ith component of the cosine Fourier transform of $f(x)$, and $f(\Psi_n)$ is the Ψ_n distribution. For this analysis, N =12 is a sufficient number of components to flatten the Ψ_n distribution. The re-centering and flattening calibration is done in separate 30 z-vertex bins since the detector acceptance in ϕ will vary with z-vertex.

4.3 East West v_2 Discrepancy

As discussed in the previous section, distortions in the raw Ψ_2 distribution can cause distortions in the measurement of v_2. In this section, we discuss how the beam alignment effects the raw $\Psi - 2$ distribution and how it can be corrected for.

As shown in Fig 4.9, v_2 is different when measured using tracks in the west (-1 $< \phi <$ 1) and east arm (2 $< \phi <$ 4) of the CA. This is a systematic effect explained by the colliding beams not being parallel to the longitudinal axis of PHENIX. When examining beam alignment effects on the v_2 measurement, we can quantify the east-west v_2 asymmetry by calculating R_{v_2} which is calculated by:

$$R_{v_2} = \frac{\sum_{p_T} v_2^{\text{east}}(p_T)}{\sum_{p_T} v_2^{\text{west}}(p_T)}. \tag{4.18}$$

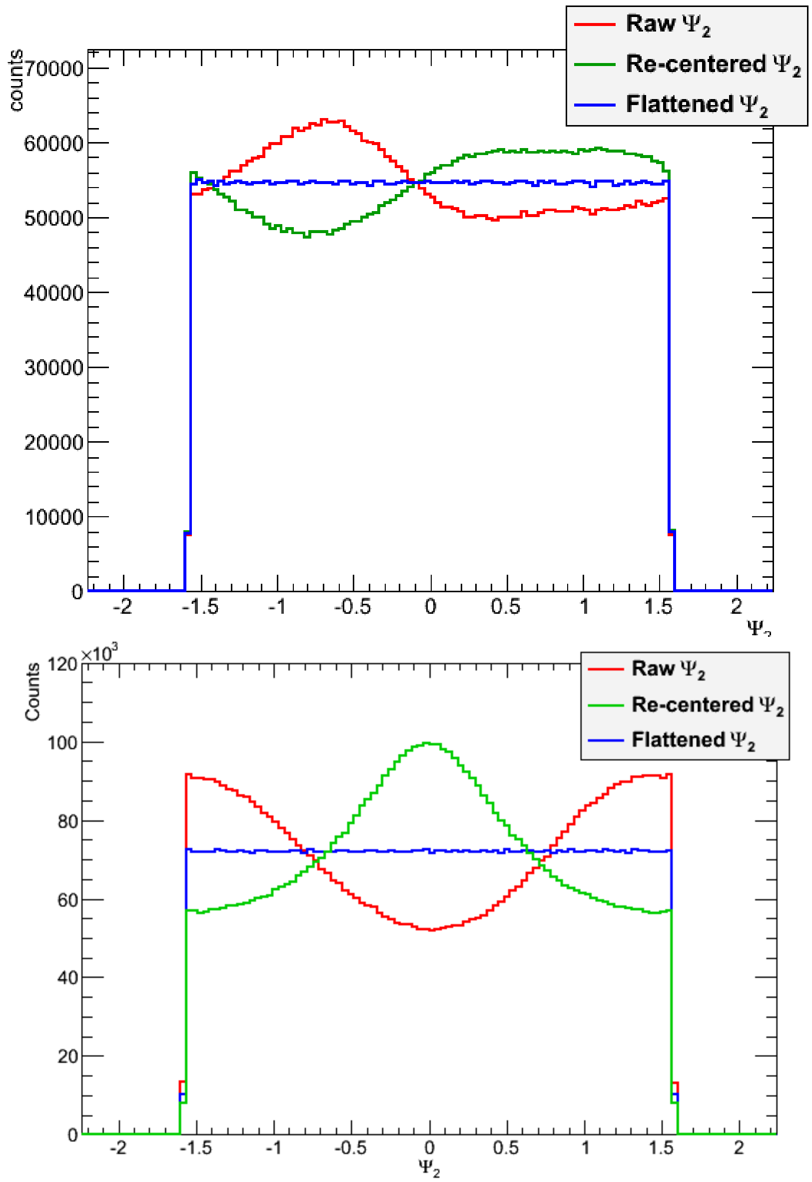

Figure 4.8: This is the Ψ_2 distribution projected over all z-vertex bins at different steps during the calibration. The top is from the FVTX south and the bottom is from the BBC south. The range of the Ψ_2 resolution is from -$\frac{\pi}{2}$ to $\frac{\pi}{2}$ because of the periodicity. The raw (in red) Ψ_2 distribution has a sinusoidal shape. The re-centered (in green) Ψ_2 distribution moves the mean. The flattened (in blue) Ψ_2 distribution spreads out the counts so that there is uniformity. Each calibration step preserves the integral.

In Figure 4.11, $R_{v_2^{\mathrm{FVTXS}}}$ can be extracted by taking the ratio of the numbers in the legend of the upper right plot and $R_{v_2^{\mathrm{BBCS}}}$ can be extracted the same way for the numbers in the bottom left plot's legend. The $R_{v_2^{\mathrm{FVTXS}}} = 1.61$ while the $R_{v_2^{\mathrm{BBCS}}} = 0.43$, indicating large east west asymmetry

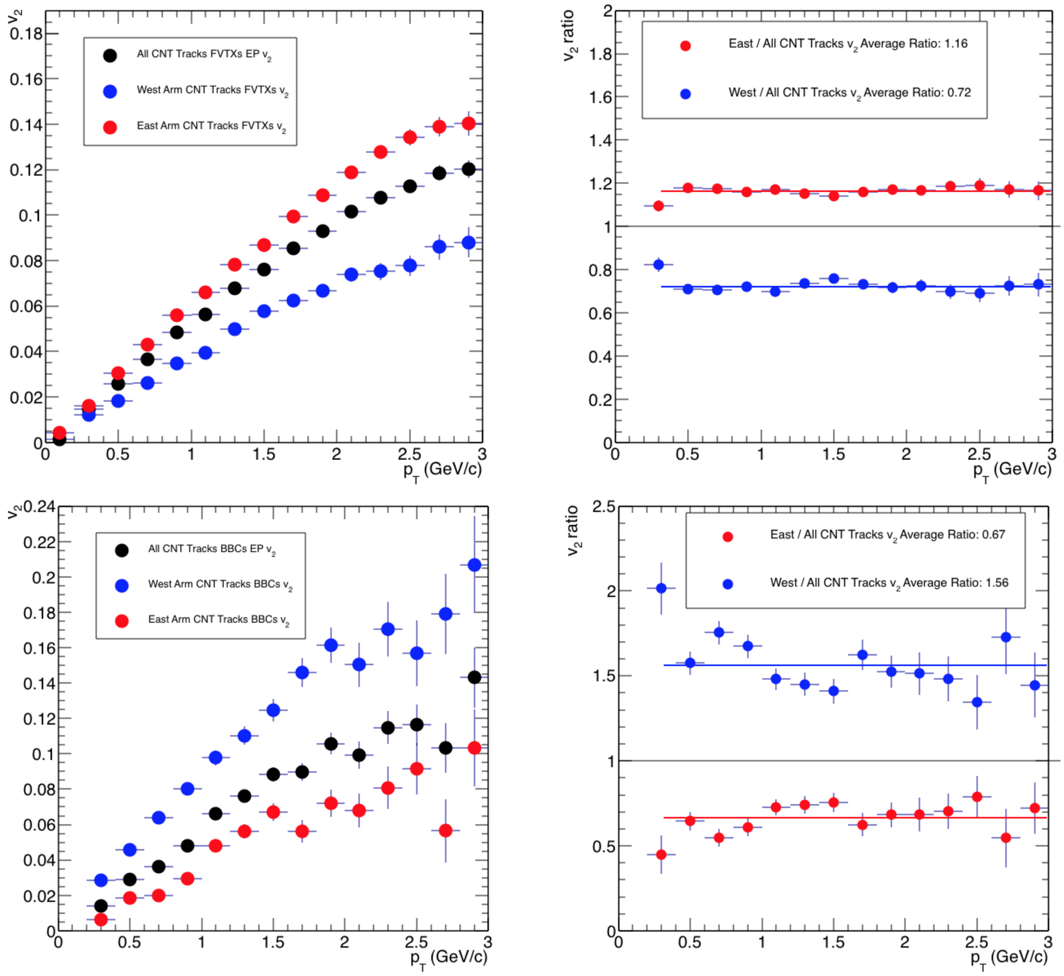

Figure 4.9: First attempt at measuring $v_2(p_T)$ with the event plane as calculated with the FVTXS (top left) and the BBCS (bottom left) in the p+Au at $\sqrt{s_{NN}} = 200$ GeV dataset, using the default resolution as shown in Table 4.4. The black points show v_2 measured using all CA tracks. The blue and red points show v_2 measured using only tracks in the west and east arms, respectively. The ratios are fit with a constant, whose value is shown in the legend.

in both measurements, although the $R_{v_2^{\mathrm{BBCS}}}$ is bigger. It is interesting to note that the splitting of the east and west v_2 measurements goes in opposite directions for the BBCS as compared to the FVTXS. To understand where the discrepancy in these v_2 measurements comes from, we examine the effects of the beam alignment on the v_2 measurement.

4.4 Correcting for the Effects of Beam Alignment

As discussed in Chapter 3, Section 3.2.9.1, due to a necessity of running p+Au at $\sqrt{s_{NN}}$ = 200 GeV at RHIC, the beam geometry was no in accordance with the PHENIX coordinate system. First of all, the collision vertex is significantly offset from the z-axis to which all of the PHENIX detectors are aligned. The other beam geometry effect, and the more significant of the two effects, comes from the fact that the beams are colliding at an angle of 3.6 milli-Radians in the x-z plane as show in Fig 4.10 [2]. The reason a non-ideal beam geometry creates an east west v2 measurement difference is because of the assumption that the ideal event plane angle is azimuthally isotropic during the event plane flattening calibration. In the translated and rotated frame where the beams are aligned with the z-axis the event plane distribution would be uniform, but in the lab frame the event plane distribution in ϕ would have regions of enhancement and reduction. The event plane flattening calibration algorithm restores a non-uniform distribution to a uniform one; however, if the true event plane distribution is non-uniform then forcing the measured distribution to be uniform produces a systematic offset.

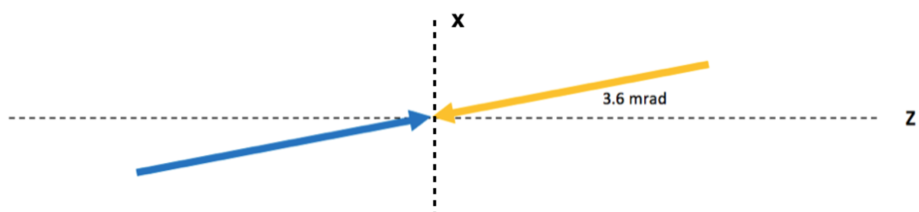

Figure 4.10: Diagram illustrating the angle at which the yellow and blue beams collide relative to the longitudinal $z-$axis of the detector. The yellow beam corresponds to the Au (south-going) beam, and blue corresponds to the proton (north-going) beam. Due to a necessity of running p+Au collisions at $\sqrt{s_{NN}}$ = 200 GeV at RHIC, the beams collide at an angle of 3.6 mrad.

We correct for the offset of the collision vertex by shifting the origin of the PHENIX global coordinate system to the true collision vertex. To correct for the effect of the beam angle, we apply a global rotation of the PHENIX coordinate to align its longitudinal axis with that of the beams.

In practice, these transformations are accomplished by individually applying a global rotation and translation to every CA track, FVTX cluster, and BBC PMT.

As shown in Fig 4.11, applying these corrections prior to calculating v_2 reduces the magnitude of the east-west discrepancy. The new $R_{v_2^{\mathrm{FVTXS}}} = 1.43$, and $R_{v_2^{\mathrm{BBCS}}} = 0.66$, are reduced from the east-west difference measured without any corrections. However, even after rotating the PHENIX global coordinate system to be in alignment with the beam axis, Ψ_2 is, there is a residual effect from the beam rotation which still effects the v_2 measurement.

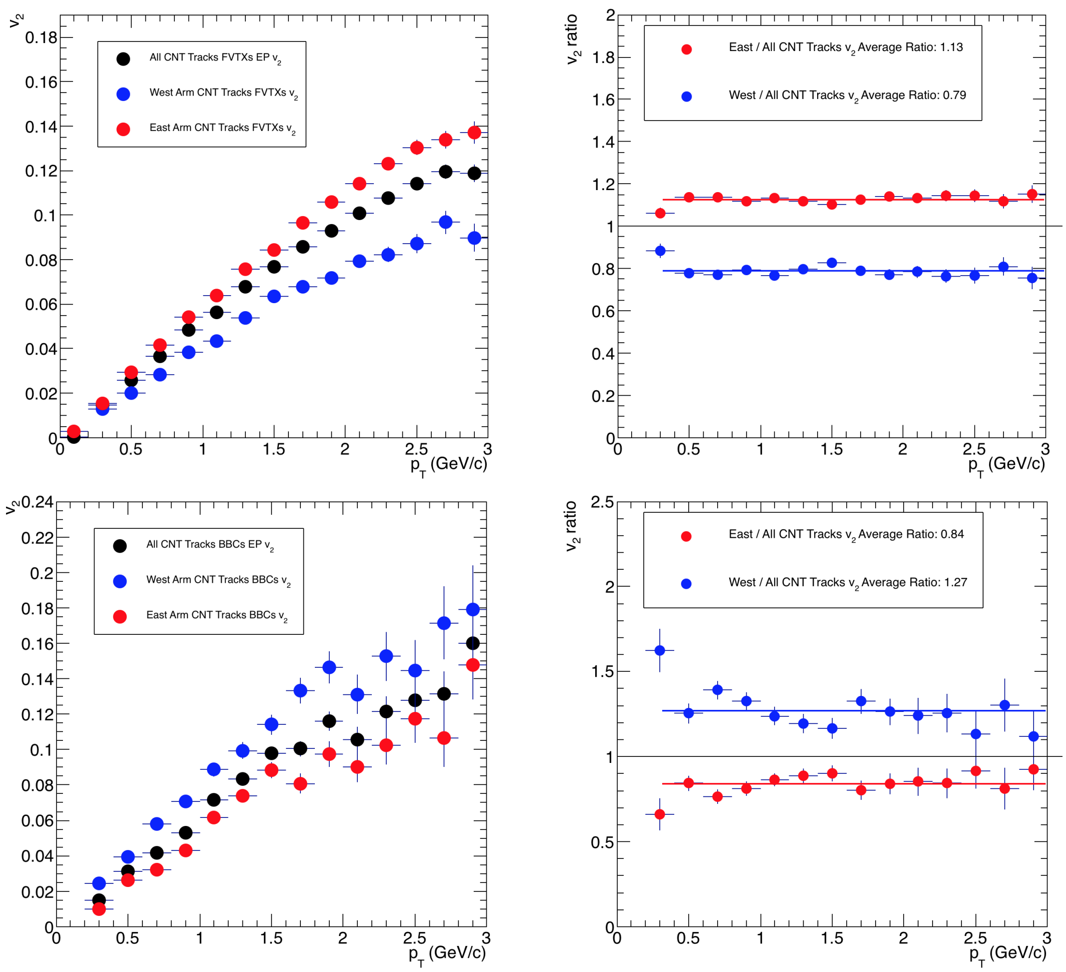

Figure 4.11: A corrected measurement of v_2 as a function of p_T with the FVTXS (top two panels) and the BBCS (bottom two panels) event plane for the p+Au $\sqrt{s_{NN}} = 200$ GeV dataset. The default resolution as shown in Table 4.4 is used. The plotting conventions are the same as described in the caption of Fig 4.9.

To explain this effect, consider a cylindrical disk with a hole in the middle, centered about the z-axis (in analogy to the shape of the FVTX and the BBC), as shown in the left plot of Fig 4.12. In this geometry, all points along a ring of constant radius are at the same pseudorapidity. However, if one were to tilt that disk, the pseudorapidity of points along that ring would be ϕ dependent. The tilt of the disk changes its pseudorapidity acceptance and its extent. Now consider that it is not the disk that is tilted but rather the beam orientation that is tilted. The previous statements about the effect on the η range being ϕ dependent still apply.

The combination of the η acceptance changing and the η distribution of charged particles not being flat means that the average number of charged particles going through the disk would be systematically ϕ dependent, as illustrated in Fig 4.12 (right). If the average charged particle distribution is not uniform in ϕ, the event plane distribution will not be either. This results in the flattening procedure creating systematic effects such as the east-west v_2 asymmetry.

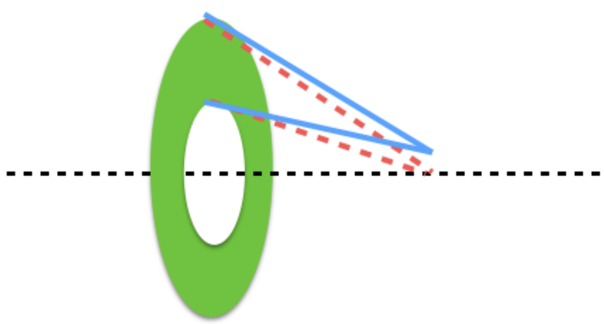

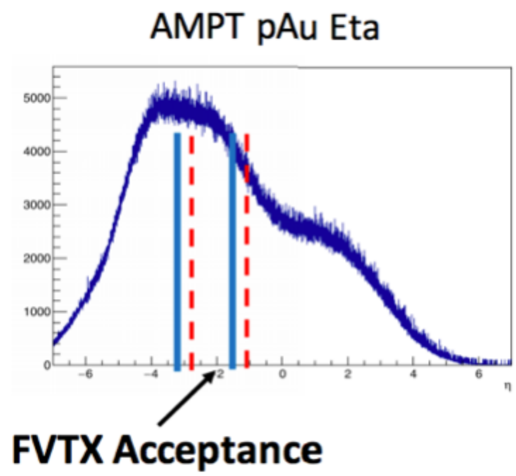

Figure 4.12: (left) Cartoon diagram illustrating η acceptance shift due to a beam offset in one of the FVTXS layers. (right) Pseudorapidity distribution of charged particles from the AMPT Monte Carlo generator for p+Au $\sqrt{s_{NN}} = 200$ GeV, showing the shift in η acceptance.

In order to correct for this effect, an additional weight factor is introduced for FVTX clusters and BBC PMTs during the event plane calculation. This factor is such that hits in ϕ regions with systematically fewer particles are given a larger weight, and correspondingly, hits in ϕ regions with systematically more particles are weighted less. The introduction of this weighting as defined below does not formally change the event plane calculation, as a weight factor is already implemented in its construction. The modified weight factor is:

$$w_i = w_i^D F(\phi, z_{\text{vertex}}) \tag{4.19}$$

where w_i^D is the default weighting associated with the detector element, and $F(\phi, z_{\text{vertex}})$ is the multiplicative weighting to correct for the beam geometry. $F(\phi, z_{\text{vertex}})$ is dependent on z_{vertex}, in addition to ϕ, because η is dependent on the collision vertex.

4.4.1 Analytic Correction Method

One can analytically calculate this ϕ dependent weight factor using the geometry of the FVTXS and BBCS as well as using the η distribution of charged particles. Unfortunately, the η distribution of charged particles in p+Au $\sqrt{s_{NN}} = 200$ GeV has not been measured by an experiment, so we must rely on models that cannot be fully checked. We can simulate 0-2 impact parameter p+Au at $\sqrt{s_{NN}} = 200$ GeV events in AMPT and determine the simulated $dN_{ch}/d\eta$ as shown in the right panel of Figure 4.12.

The left panel of Figure 4.13 shows the ϕ dependence of the η acceptance with a beam angle (solid line) and without a beam angle (dotted line). By taking the ratio of the η acceptance after with a beam angle to the η acceptance without a beam angle for each ϕ angle we calculate the correction factor shown in the right panel of Figure 4.13. This correction factor is the multiplicative weight factor w_i as defined in the last section.

4.4.2 FVTX Inverse Phi Weighting

Another way to determine the weight factor is to use a data driven method of measuring the extent that each ϕ region in a detector has systematically more or less particles. Then an inverse weighting based on this measurement is applied to the ϕ regions to correct the detector's ϕ distribution to uniformity.

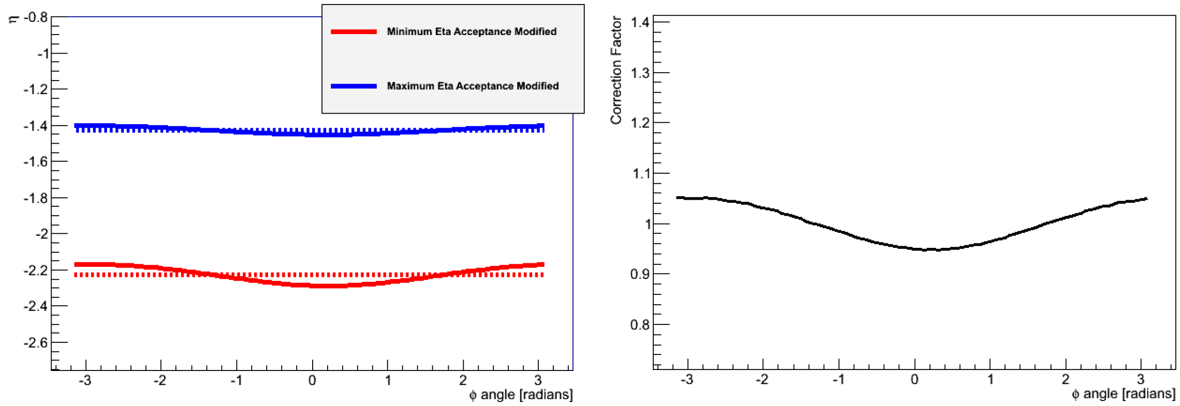

Figure 4.13: The modification of the η acceptance as a function of ϕ for the FVTX first layer (left) and the calculated correction factor from this modification (right).

For the FVTX implementation of this, first the rotation and offset correction are applied. Then, the weight factor is determined by plotting all hits in a cylindrical disk detector vs ϕ, normalizing this distribution to one, and then inverting it. Applying this weight factor to the data will produce uniform hit distributions in ϕ in the detectors in which it is applied. This will, in turn, make the event plane distribution more uniform when measured in those detectors, thus correcting for the effect. The added benefit of using this method is that it also corrects for hot and cold ϕ regions in the detector. In order to get rid of significant hot or cold ϕ regions, ϕ regions with weight factors greater than 1.5 or less than 0.5 are set to 0.0. This correction is done for each FVTX layer, in z-vertex bins, and on a run-by-run basis. The multiplicative weight function $F(\phi, z_{\text{vertex}})$ for the FVTX disks is defined as

$$F(\phi, z_{\text{vertex}}, layer) = \frac{\langle N_{\text{cluster}}(z_{\text{vertex}}, layer)\rangle}{N_{\text{cluster}}(\phi, z_{\text{vertex}}, layer)}, \tag{4.20}$$

where $N_{\text{cluster}}(\phi, z_{\text{vertex}}, layer)$ is the number of FVTX clusters as a function of ϕ, z_{vertex}, and FVTX layer and $\langle N_{\text{cluster}}(z_{\text{vertex}}, layer)\rangle$ is the ϕ average of the number of clusters. The weighting can be seen in Fig 4.14. A comparison between the FVTX weighting and the analytic correction is shown. The good agreement indicates the validity of the weighting.

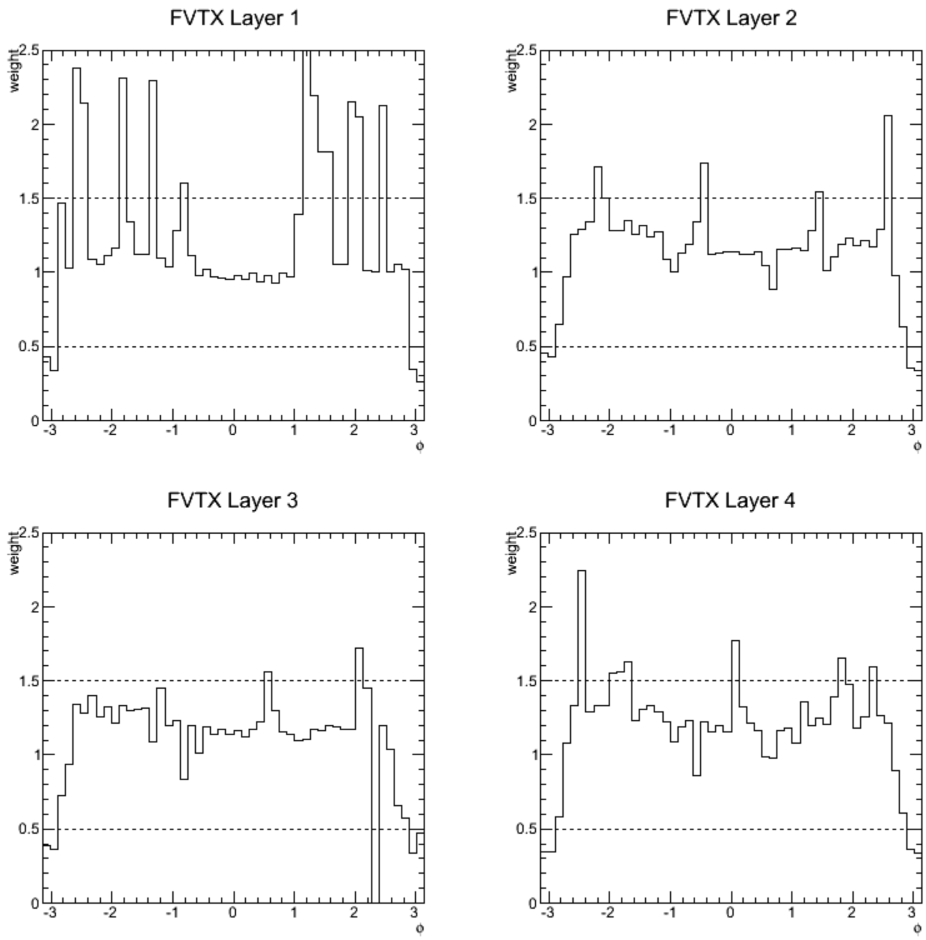

Figure 4.14: These four panels show the FVTX ϕ dependent cluster weighting when calculating the FVTX event plane for each layer separately for events with a collision vertex in z is around 0. There are some ϕ regions where weight factor is outside of the dotted line bounds. This indicates that either there was a severe deficit or excess of clusters measured in the region. Later, we will examine the effect of keeping these regions or cutting them out on the v_2 measurement.

4.4.3 BBC Charge Weighting

For the BBC, we used another data driven method to correct for the non-uniform particle distribution. Using the distribution of particles in the BBC from the 2015 p+p $\sqrt{s} = 200$ dataset as a baseline, we applied an inverse weighting much like the method described in the previous section. In the p+p dataset, there was no issue with beams colliding at an angle and the average charge across all 64 PMTs in the BBCS is uniform. In this method, the multiplicative weight function

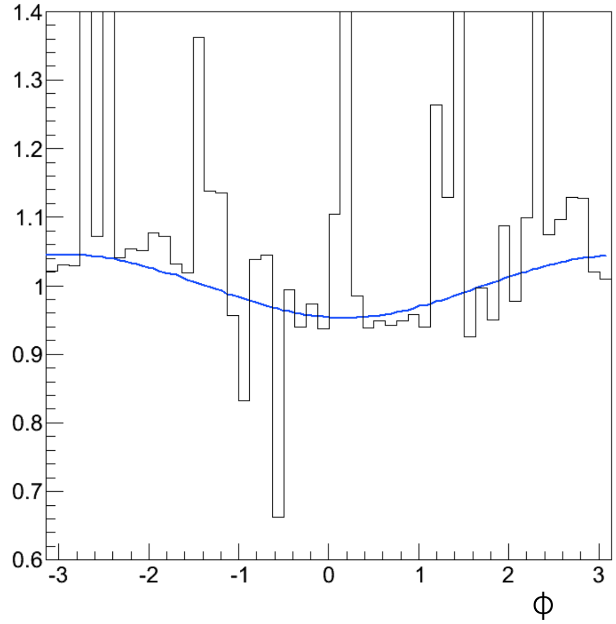

Figure 4.15: The black is the FVTX weighting and the blue is the analytic weighting. They have good agreement.

$F(PMT, z_{\text{vertex}})$ for the BBCS is defined as:

$$F(PMT, z_{\text{vertex}}) = \frac{\left\langle N^{p+p}_{Charge}(z_{\text{vertex}}) \right\rangle}{\left\langle N^{p+\text{Au}}_{Charge}(PMT, z_{\text{vertex}}) \right\rangle}, \tag{4.21}$$

where $< N^{p+p, p+\text{Au}}_{Charge}(PMT, z_{\text{vertex}}) >$ is the event averaged charge as a function of PMT and z_{vertex} for the p+p and p+Au datasets respectively. This weight function is shown in Fig 4.16 and is applied directly to the event plane calculation using Eqns 4.19 and 4.13. Although the weight function could be defined as a function of ϕ like in the FVTX case, the positions of the PMTs in the BBC are fixed and it is more direct to take the ratio between PMTs.

One effect of using this weighting method is that it will make the distribution of particles in the BBC in ϕ and η uniform. This can be illustrated by looking at Fig 4.17. It is apparent that the p+p average charge is much more uniform than the p+Au average charge as a function of ϕ and ring. After applying the p+p/p+Au ratio weighting, which is essentially dividing the left plot by the right plot in Fig 4.17, the PMT charges in ring 1 for the p+Au dataset will be deweighted so that their corrected average charge will be uniform in ϕ, and in agreement with the average charge

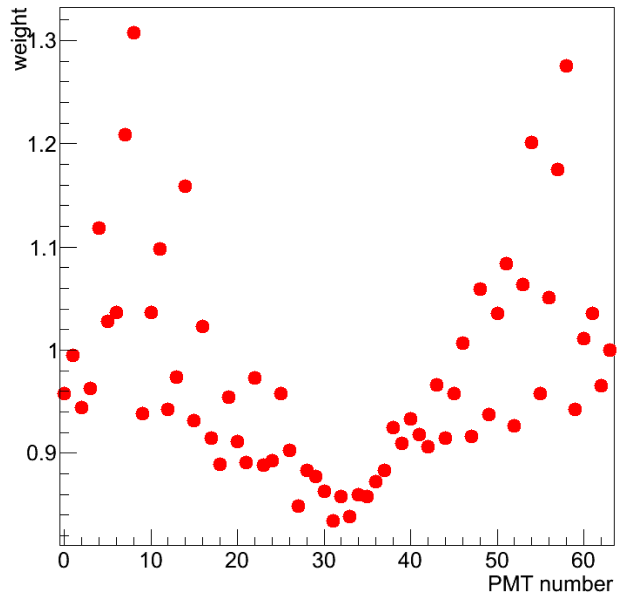

Figure 4.16: Shown here is BBC the multiplicative weight factor F used when calculating the modified event plane for events where the collision vertex in z is around 0. The y-axis is the weight factor and the x-axis is the PMT number for the BBCS (there are 64 total in the BBCS).

for the other rings. If all the BBC rings have the same average charge, this means that the average charge as a function of η for the BBC will be approximately uniform. This is one reason why this method (p+p/p+Au ratio weighting) is preferred for the BBC, because the variations in the average charge between the rings are normalized. One could apply the FVTX method of inverse ϕ weighting by inverting the right plot of Fig 4.17 to find the weight function. However, although using only the p+Au dataset would normalize the average charge as a function of ϕ, it would not normalize the charge as a function of η. Both methods applied to the data are shown in the next section but the p+p/p+Au ratio method does better.

4.4.4 Applying Weighting to v2

The previously discussed corrections are applied when calculating the raw Ψ_2^{FVTXS} used in the v_2 measurement. Shown in Figure 4.18 is the correction summary for the FVTXS v_2 measurement where $R_{v_2^{\mathrm{FVTXS}}}$ is the y-axis. The first column, which corresponds to $R_{v_2^{\mathrm{FVTXS}}}$ calculated using

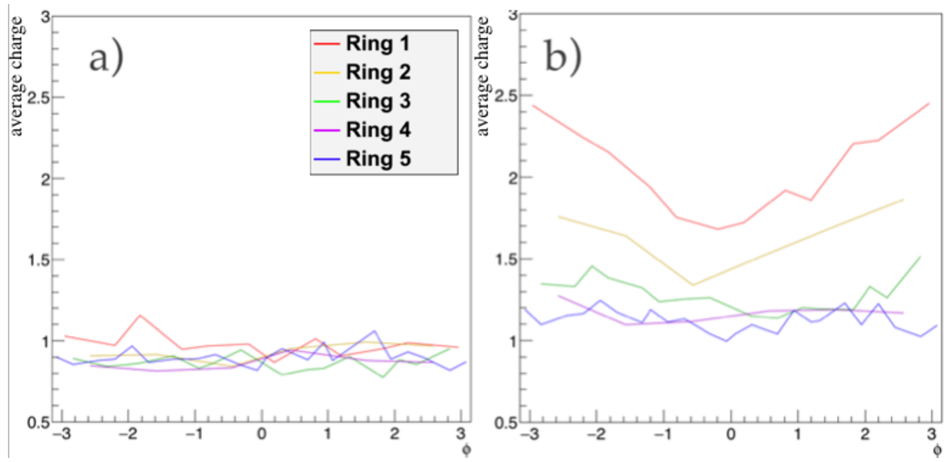

Figure 4.17: These plots depict the average PMT charge per event versus ϕ in the a) the p+p $\sqrt{s}$ = 200 GeV and b) p+Au $\sqrt{s_{NN}}$ = 200 GeV. The PMTs are separated by color, which corresponds to the rings of approximate common radius as shown in Fig 4.6. The left plot shows near uniformity as a function of ϕ and ring. However, the right plot shows a significant deviation from uniformity especially for the innermost rings (rings 1 and 2). In addition to the ϕ variation for the right plot, the innermost rings have the largest average charge when compared to the other rings. This is in part due to the fact the innermost rings cover the a slightly larger η range. However, the innermost rings in the left plot also cover the largest η range and do not exhibit this separation in rings.

FVTXS layers 1, 2, and 4, with layer 3 being excluded, is explained shortly. The black, red, blue, and green points correspond to no weighting, analytic weighting, inverse ϕ weighting, and inverse ϕ weighting with cuts, respectively. Compared to the $R_{v_2^{\mathrm{FVTXS}}}$ calculated with no weighting, $R_{v_2^{\mathrm{FVTXS}}}$ calculated with each of the corrections brings the ratio quantity much closer to 1.0, indicating the weighting techniques are working. In order to better understand the effect of the corrections, $R_{v_2^{\mathrm{FVTXS}}}$ is measured separately with each FVTXS layer. The rationale for this exclusion is due to FVTXS layer 3's unusual behavior in relation to the other FVTXS layers. As we go from layer 1 to layer 4, the $R_{v_2^{\mathrm{FVTXS}}}$ generally is trending downward except for layer 3. Although the reason for this was never definitively determined, it is likely there is something wrong with the layer data due to electronic or detector problems. Thus, the measurement of v_2^{FVTXS} is calculated without any clusters in the third layer.

Similarly, Figure 4.19 is the correction summary for the BBCS v_2 measurement where $R_{v_2^{\mathrm{BBCS}}}$ is the y-axis. The first column corresponds to $R_{v_2^{\mathrm{BBCS}}}$ calculated using all five BBCS rings. Com-

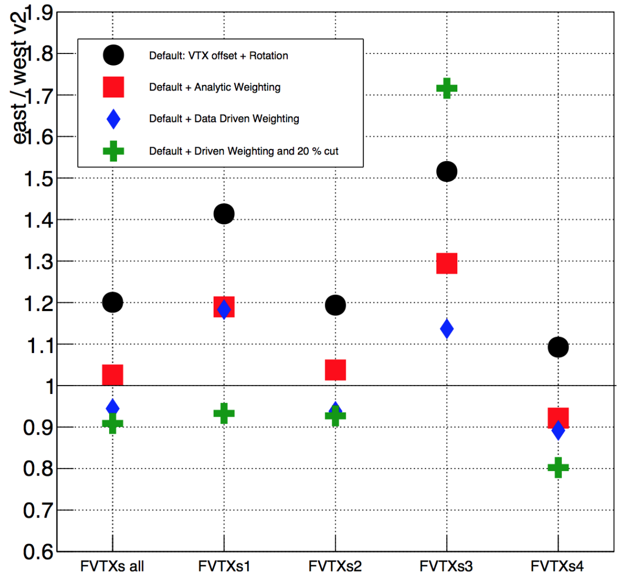

FVTXs All using layers 1, 2, and 4

Figure 4.18: Plotted is the FVTXS correction summary where the y-axis is the east/west v_2 ratio and the x-axis is the different subset of clusters used to calculate the v_2. The black markers correspond to the default corrections. The red boxes correspond to the corrections with the analytic weighting shown in Fig 4.13. The blue diamonds are the FVTX inverse ϕ weighting as shown is section 4.4.2. Finally, the green crosses correspond to the same as the blue diamonds except an additional hot-cold filter of 20% was applied. The first column is using all the FVTXS layers except for the 3rd layer (explained in the text). So the first columns should be approximately the average of columns 2, 3, and 5. Columns 2 through 5 show the ratio calculated from clusters only in that layer.

pared to the $R_{v_2^{\mathrm{BBCS}}}$ when calculated with no weighting, $R_{v_2^{\mathrm{BBCS}}}$ when calculated with the data driven and p+p/p+Au ratio weighting is modestly closer to 1.0. By looking at $R_{v_2^{\mathrm{BBCS}}}$ calculated with PMTs in individual BBCS rings for the weighted points, $R_{v_2^{\mathrm{BBCS}}}$ is generally trending downward as a function of ring number. Applying the weighting corrections to $R_{v_2^{\mathrm{BBCS}}}$ calculated by ring 1, the innermost ring, over-corrects $R_{v_2^{\mathrm{BBCS}}}$. This may be explained by the fact that ring 1 covers the largest η acceptance range, causing the correction to be inconsistent. The reason why ring 1 is not excluded from the inclusive v_2 calculation, like FVTXS layer 3 excluded, is because there is no reasonable justification to exclude it other than its over-corrected $R_{v_2^{\mathrm{BBCS}}}$ values. While FVTXS layer 3 breaks the trend of $R_{v_2^{\mathrm{FVTXS}}}$ decreasing, BBCS ring 1 follows the $R_{v_2^{\mathrm{BBCS}}}$ ring trend.

Fig 4.20 shows the $v_2(p_T)$ with the inverse ϕ weighting and 20 % cut from Figure 4.18. This

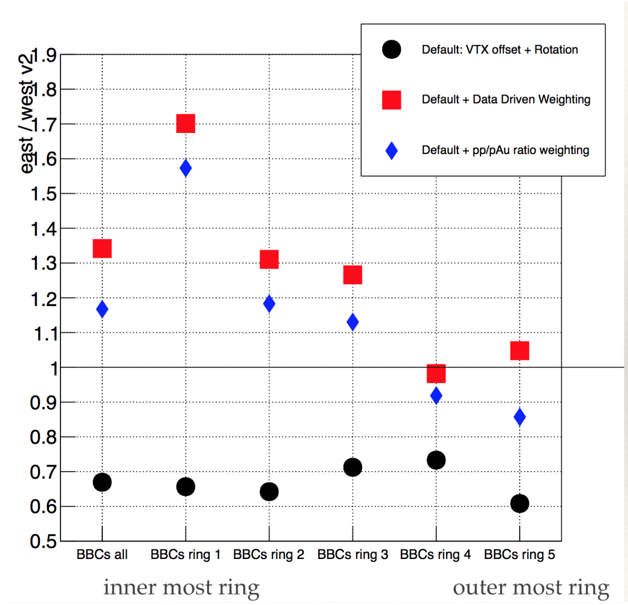

Figure 4.19: Plotted is the BBC correction summary where the y-axis is the east/west v_2 ratio and the x-axis is the different subset of PMTs used to calculate the v_2. The black markers correspond to the default corrections. The red boxes correspond to the corrections with the analytic weighting shown in Fig 4.13. Finally, the blue diamonds correspond to the BBC inverse ϕ charge weighting as shown is section 4.4.3. The first column is the quantity calculated from all PMTs. Columns 2 through 6 are using PMTs from certain rings as defined in Fig 4.6. Ring 1 is the hardest to correct. The first column should approximately be the average of all the other columns.

figure also shows $v_2(p_T)$ with the pp/pAu ratio weighting from Fig 4.19. Although the east and west v_2^{BBCS} measurements do not collapse together like the east and west v_2^{FVTXS} measurements, the result is good enough to be incorporated in our systematics uncertainties. Due to the fact that $R_{v_2^{\mathrm{FVTXS}}}$ is corrected to within $\pm 10\%$ and the fact that $v_2^{\mathrm{FVTXS}}(p_T)$ has smaller a statistical uncertainty, the primary $v_2(p_T)$ measurement is done using the FVTXS.

In order to estimate the contribution of this systematic uncertainty, we assume the true v_2 value is absolutely bounded between the separate east and west measurements and we assume that the probability distribution for v_2 is uniformly distributed between the upper and lower bounds. Thus, we calculate the point-by-point absolute value of v_2^{east} minus the v_2^{west} divided by $\sqrt{12}$, which is the RMS of an uniform distribution. By using the best corrected BBCS v_2 measurement in this calculation, we assign a value of 5% for this systematic uncertainty.

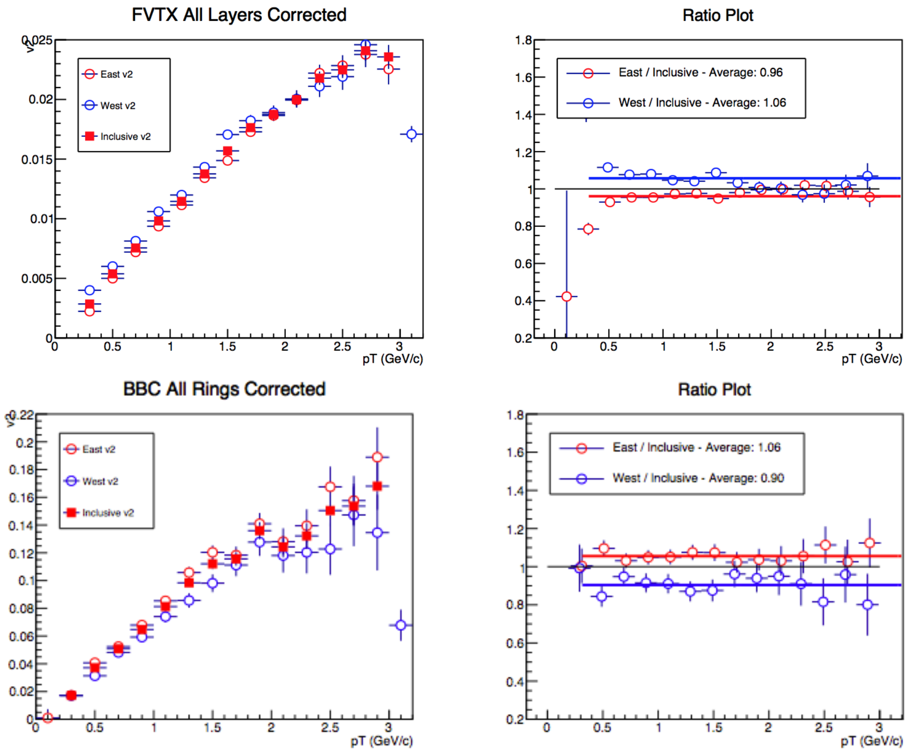

Figure 4.20: FVTXS v_2 event plane measurement corrected with inverse ϕ weighting and 20 % cut with FVTXS layer 3 is excluded (top) and BBCS v_2 event plane measurement corrected with p+p/p+Au ratio weighting (bottom).

4.5 Other Sources of Systematic Uncertainty

4.5.1 Effect of Event Pile-Up

Pile-up events occur when there are two or more collisions within the same bunch crossing. Pile-up events are an issue for this analysis because they:

(1) are erroneously included into the 0-5% centrality selection due to two smaller collisions looking like a larger collision,

(2) and reduce the value of v_2 because the event plane angle from one collision will be different than the event plane angle in the other collision, such that correlations calculated by using particles produced from the two collisions are random and will dilute the real correlations, thereby reducing the flow signal.

In order to filter pile-up events we look at the distribution of BBC PMT timing values as seen in Fig 4.21. A normal event is strongly peaked at 0 while a pile-up event has a broad distribution and may not be centered at 0. We developed an algorithm to efficiently filter pile-up events by analyzing the BBC PMT timing value distribution event by event. When the v_2 values are compared with and without the filter, a difference of 4% is seen.

Pile-up events occur at a rate of 8% in 0-5% central p+Au collisions. Low-luminosity and high-luminosity subsets of the data were analyzed, and the systematic uncertainty was determined to be $^{+4\%}_{-0\%}$, since the v_2 was found to decrease in the events that contain a pile-up

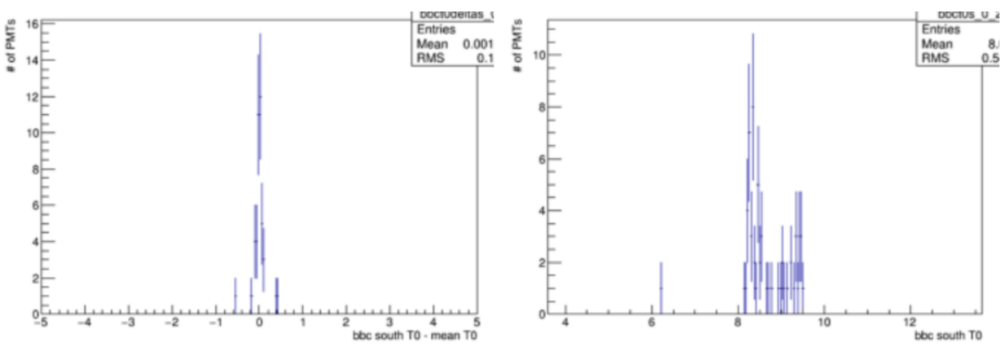

Figure 4.21: The distribution of BBC PMT timing values. The x-axis is the difference between the southern BBC PMT t_0 - the mean t_0 in the south. An example of a normal event (left) and an example pile-up event (right), are shown.

4.5.2 Event-Plane Detectors

We expect that the value of v_2 should be consistent when measured in different detectors, after applying corrections. Any remaining difference of v_2 measured independently in the FVTXS and BBCS indicates a source of systematic uncertainty. The difference is calculated after applying corrections to beam alignment v_2, as shown in Figure 4.22. The right panel of the figure shows the average difference to be around 0.97. Thus, the systematic uncertainty estimated is $\pm 3\%$.

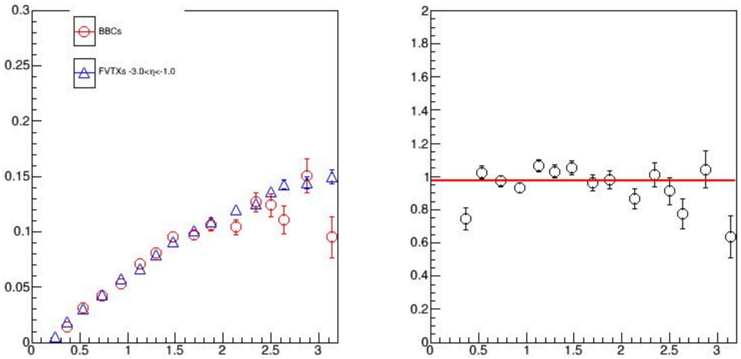

Figure 4.22: $v_2(p_T)$ measured separately in the BBCS and the FVTXS after beam alignment corrections (left) and the ratio of v_2^{FVTXS} to v_2^{BBCS} (right). The red line is the average of the ratio across p_T.

4.5.3 Track Background

The set of tracks that are used in this analysis come from central arm tracks which are known to have a track background of 2.0%. The track background from photonic conversions and weak decays, and mis-reconstructed tracks, which we estimate at 2% relative to v_2 by varying the windows in the PC3 matching variables from 3σ to 2σ;

4.5.4 Effects of Non-Flow

As discussed in Chapter 2, non-flow is a catch-all term used to categorize all types of long-range angular correlations which do not arise from hydrodynamic flow and are not related to the initial collision geometry. Non-flow constitutes a significant background to our measurement. There are several known sources of non-flow:

(1) hard scattering events producing dijets

(2) initial state correlations between target and projectile

(3) decay chains of exotic particles

(4) momentum conservation.

Fig 4.23 shows the characteristic two-particle correlations arising from non-flow associated with dijets. The near-side peak at (0,0) is from the cone of particles in a single jet all at a similar location in η and ϕ. The away-side ridge around $\phi = \pi$ originates from particles pairs, where each particle belongs to a different jet. The two jets are completely back-to-back in $\Delta\phi$, but have a spread in $\Delta\eta$. This correlation function yields a substantial c_2 very similar to that from the hydrodynamic flow signal we are seeking. In order to minimize the contribution of dijet events, the standard flow analysis procedure is to select regions outside of the red dotted lines seen in Fig 4.23 ($|\Delta\eta| > \eta_{min}$, where η_{min} is usually of order 1.0 unit of pseudorapidity).

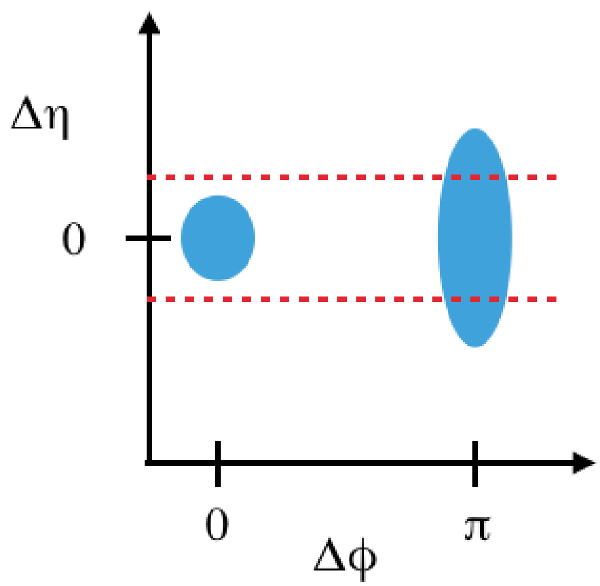

Figure 4.23: Plotted here is the 2D profile of a correlation function in $\Delta\eta\Delta\phi$ space of a dijet event. The area in red dotted lines represent the exclusion zone in $\Delta\eta$, such that the measurement is made only using data from outside of the exclusion zone to reduce non-flow contributions.

In order to estimate the degree of presence of non-flow, we can measure the c_2 from p+p events which should be devoid of any hydrodynamic flow but should have many of the sources of non-flow present. In order to compare p+p with p+Au, we must scale-up the p+p quantity by the dilution factor defined in eq 4.22. The scaled down reference c_2 is shown as blue squares in Fig. 4.24, panel (a). The ratio of c_2 in the scaled-down p+p reference to that in p+Au is shown in panel (b).

From this ratio, as calculated in Equation 4.22, it can be seen that the relative correlation strength in p+Au from elementary processes is at most 23% at the highest p_T. Since this procedure constitutes an approximation to quantify the non-flow correlation strength, it is not subtracted from the total signal, instead it is treated as a source of systematic uncertainty. Even though the p+Au and the p+p baseline data were collected in different years, such that potential changes in detector performance could affect our results, it was verified that using p+p data from various run periods has an effect of at most 3% on the calculated non-flow contribution. The non-flow correlations which enhance the v_2, whose contribution we estimate from Figure 4.24, assigning a p_T-dependent asymmetric uncertainty with a maximum value of $^{+0}_{-23}$%

$$c_2^{\mathrm{pAu\ elementary}}(p_T) \simeq c_2^{p+p}(p_T)\frac{\left(\sum Q^{\mathrm{BBC\text{-}S}}\right)_{p+p}}{\left(\sum Q^{\mathrm{BBC\text{-}S}}\right)_{\mathrm{pAu}}}. \tag{4.22}$$

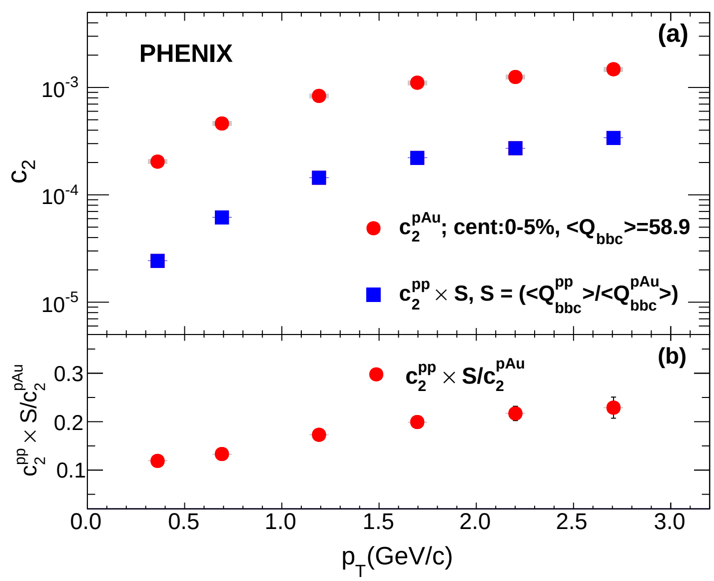

Figure 4.24: (a) The second order harmonic coefficients $c_2(p_T)$ for long range angular correlations in 0%–5% p+Au collisions, as well as for minimum bias p+p collisions. The latter are scaled down by the factor $\left(\sum Q^{\mathrm{BBC\text{-}S}}\right)_{p+p} / \left(\sum Q^{\mathrm{BBC\text{-}S}}\right)_{\mathrm{pAu}}$. (b) The ratio of the two harmonics is plotted with the corresponding statistical errors.

4.6 Systematic Uncertainties Summary

Table 4.6 summarizes the sources of systematic uncertainty for the v_2 measurement. Each of these systematic uncertainties are categorized by type:

(1) point-to-point uncorrelated between p_T bins,

(2) point-to-point correlated between p_T bins,

(3) overall normalization uncertainty in which all points are scaled by the same multiplicative factor.

We total the five sources of systematic uncertainty, by adding them in quadrature. The total systematic uncertainty varies from $^{+7.2}_{-13.4}\%$ at low p_T to $^{+7.3}_{-23.8}\%$ at high p_T. Now that the systematic uncertainties have been estimated, we show the v_2 physics result in the next Chapter 5.

Table 4.5: Systematic uncertainties given as a percent of the v_2 measurement. Note that the non-flow contribution is p_T dependent and the value here quoted corresponds to the highest measured p_T.

Source	Systematic Uncertainty	Type
Track Background	2.0%	1
Event Pile-up	$^{+4}_{-0}\%$	2
Non-Flow	$^{+0}_{-23}\%$	2
Beam Angle	5.0%	3
Event Plane Detectors	3%	3

Chapter 5

Results and Discussion

The v_2 measurement for p+Au at $\sqrt{s_{NN}}$ = 200 GeV 0–5% centrality completes the set of flow measurements in the small systems available at RHIC: p+Au, d+Au, and ^{3}He+Au. The goal of this set of measurements is to determine the effect of varying initial collision conditions on the resulting flow.

5.1 v_2 Measurement

The resulting v_2 measurement for p+Au at $\sqrt{s_{NN}}$ = 200 GeV 0–5% centrality is shown in Figure 5.1. The systematic uncertainty varies from $^{+7.2}_{-13.4}$% at low p_T to $^{+7.3}_{-23.8}$% at high p_T, where the asymmetric uncertainty is dominated by by non-flow. The fact that the non-flow dominates the systematic uncertainty warrents further discussion on the the treatment of non-flow.

5.1.1 Non-flow Contribution

As was discussed in Section 4.4.2, the non-flow systematic uncertainty can instead be thought of as a systematic error that can be corrected for in our measurement. To further explore this non-flow effect, Figure 5.2 shows what the p+Au measurement looks like by subtracting the non-flow effect rather than treating it as an uncertainty. Due to non-flow being the dominant source of systematic uncertainty, the corrected p+Au points are nearly at the bottom of the systematic uncertainty boxes of the uncorrected points. The substantial changes this correction makes to the p+Au points, especially at high p_T, must be put in context of the field of heavy ion physics. This

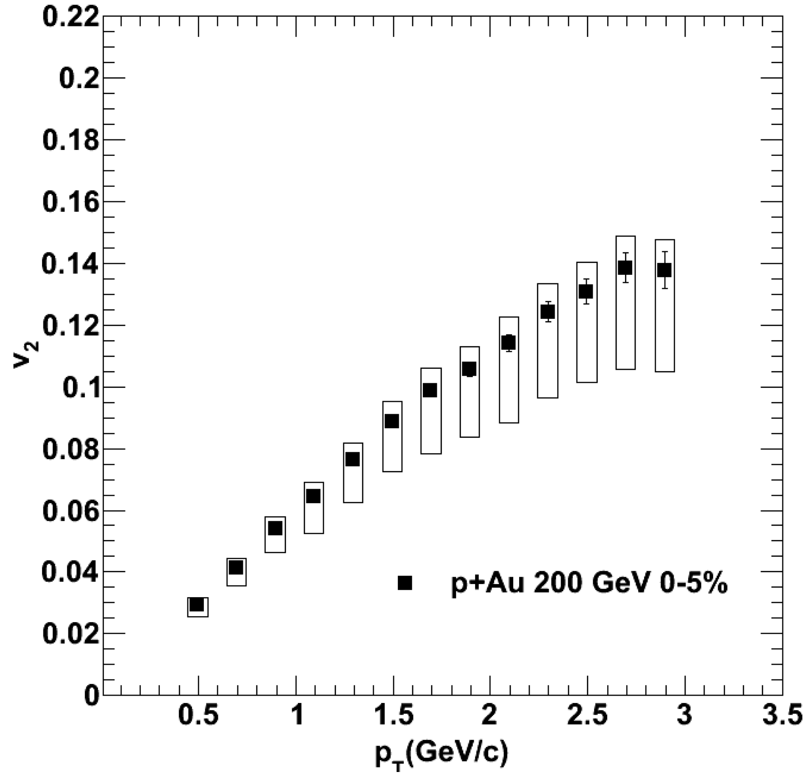

Figure 5.1: The v_2 measurement of p+Au at $\sqrt{s_{NN}}$ = 200 GeV 0–5% centrality.

procedure to estimate the contribution of elementary processes to the measured v_2 signal is an attempt at an accurate approximation. Although the non-flow approximation used in this thesis has its merits, there is currently no consensus in the field regarding how to properly quantify how much of the v_2 corresponds to "flow" and how much corresponds to "non-flow." Other experimental collaborations making flow measurements, such as STAR, ATLAS, and ALICE, treat non-flow in different ways **to add refs**. Therefore, we chose to explicitly state our methodology to estimate this non-flow and to treat it as a systematic effect that raises the measured v_2.

5.2 Comparison with Other Species at $\sqrt{s_{NN}}$ = 200 GeV 0–5% Centrality

The substantial v_2 in p+Au at $\sqrt{s_{NN}}$ = 200 GeV is interesting in itself but the significance of the measurement is best understood by comparing it to other small collision system results,

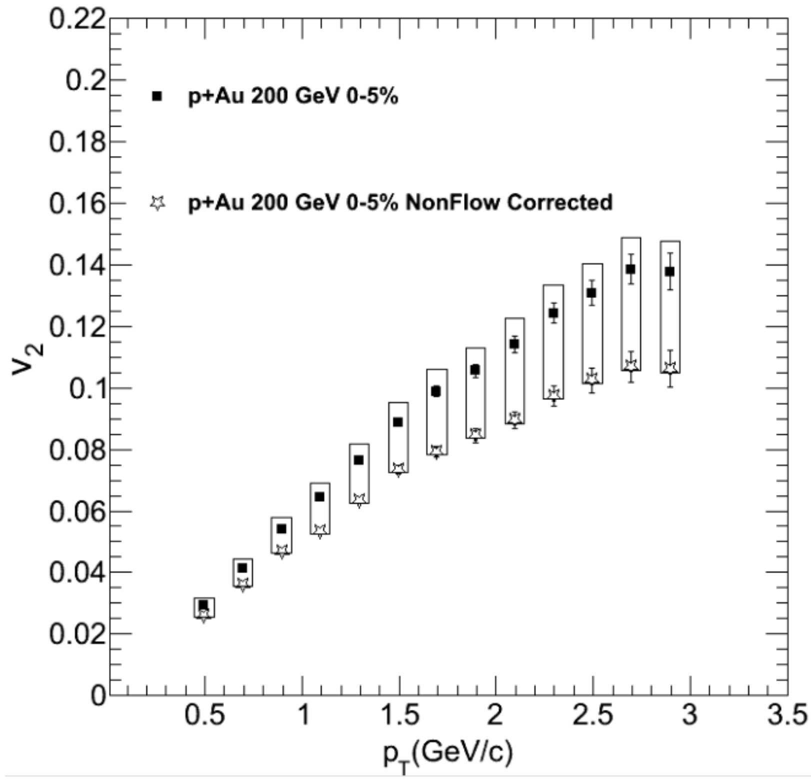

Figure 5.2: The v_2 measurement of p+Au at $\sqrt{s_{NN}} = 200$ GeV 0–5% centrality with the statistical and systematic errors corresponding to the bars and the boxes respectively. The stars are the same p+Au points but with the non-flow estimate subtracted rather than treated as a systematic uncertainty.

specifically ^{3}He+Au [7] and d+Au [7] at the same $\sqrt{s_{NN}}$ energy. In order to properly make the strongest physics statement possible in this comparison, we attempt to hold as many variables constant across all three datasets. Table 5.1 compares the various relevant parameters for the three collision species. As shown in the table, the FVTXs was not used in the d+Au measurement unlike for the p+Au and ^{3}He+Au due to the fact that the FVTX was not installed in 2008 when the d+Au measurement was taken. The table also highlights the fact that $dN_{ch}/d\eta$, the η dependence of the charged particle multiplicity, has not been measured in p+Au $\sqrt{s_{NN}} = 200$ GeV, in contrast to ^{3}He+Au and d+Au. This fact is relavent because mid-rapidity $dN_{ch}/d\eta$ is an input to the SONIC model for the purposes of multiplicity matching, as discussed in the next section. Among the differences across the columns, the largest is the lack of a non-flow estimate for the d+Au dataset.

In the interest of measurement compatibility, and for the reason stated in the previous section, there is no non-flow correction applied to any of the datasets.

Table 5.1: Dataset Variables Comparison listed in order: center of mass energy per nucleon, centrality, mid-rapidity charged particle multiplicity per unit of psuedo-rapidity from [6], year, trigger (as defined in section 2.2.4) particle sample, trigger particle acceptance, event plane determination, Ψ_2 Resolution, condition of available non-flow estimate.

Variable	p+Au	d+Au	^{3}He+Au
$\sqrt{s_{NN}}$ (GeV)	200	200	200
Centrality	0–5%	0–5%	0–5%
Mid-rapidity $dN_{ch}/d\eta$	N/A	20.8 ± 1.5	26.3 ± 1.8
Year (collected)	2015	2008	2014
Trigger Particle Sample	Charged Hadrons	Charged Hadrons	Charged Hadrons
Trigger Particle Acceptance	$\|\eta\| < 0.35$	$\|\eta\| < 0.35$	$\|\eta\| < 0.35$
Event Plane	-3< η <-1 (FVTXs)	-3.7< η <-3.1 (MPCs)	-3< η <-1 (FVTXs)
Ψ_2 Resolution	0.171	0.14	0.274
Non-flow Estimate	yes	no	yes

Figure 5.3 shows the $v_2(p_T)$ measurements in the three systems. All three measurements exhibit substantial v_2 values that rise as a function of p_T with a similar shape. Within the error bars of each measurement, the ^{3}He+Au and d+Au measurements agree and the p+Au measurement is substantially lower. This effect is especially clear at low p_T, where bulk effects would be most dominant. In order to understand the significance of this set of measurements, comparison to standard theoretical models are useful.

5.3 Comparison with Theory

Figure 5.4 shows $v_2(p_T)$ for the three systems and $v_2(p_T)$ calculations for each system from the SONIC hydrodynamic model [28], which incorporates standard Monte Carlo Glauber initial conditions followed by viscous hydrodynamics with $\eta/s = 0.08$, and a transition to a hadronic cascade at $T = 170$ MeV[1] . It is notable that these calculations for each system are matched to the charged particle density at mid-rapidity, with the exact values for 0–5% centrality of 10.0, 20.0, and

[1] Note: please reference Chapter 2 for an in depth discussion about the theoretical models of SONIC, SuperSONIC, IP-Glasma, MC Glauber, and AMPT.

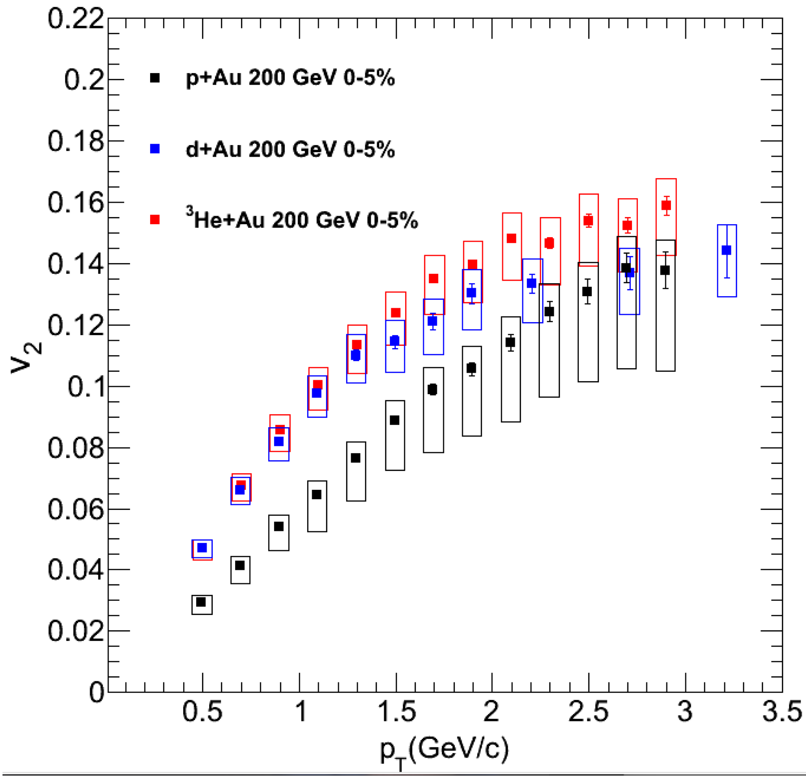

Figure 5.3: v_2 of charged hadrons within $|\eta| < 0.35$ in 0–5% p+Au compared to calculations using the SONIC model match to the same multiplicity as the data. The model calculations have good agreement with the center of the systematic uncertainty bars.

27.0, for p+Au, d+Au, and ^{3}He+Au collisions, respectively [28]. As mentioned above, the $dN_{cn}/d\eta$ has not been measured for p+Au, and the value of 10.0 was extrapolated from measurements in the other two systems [28]. The SONIC calculation includes both the geometry-related change in the initial conditions and the relative collision multiplicity for the three systems. In all these cases, a good agreement is seen within the systematic uncertainties between the data and the calculation. This agreement between data and hydrodynamic calculation alone strongly supports the notion of initial geometry coupled to the hydrodynamic evolution of the medium as a valid framework to understand small system collectivity.

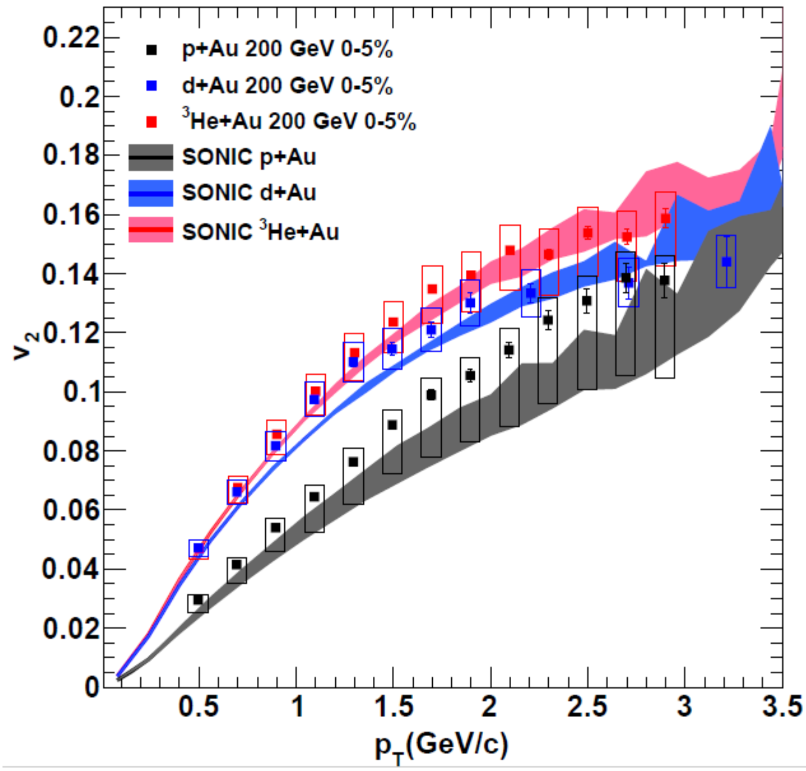

Figure 5.4: v_2 of charged hadrons within $|\eta| < 0.35$ in 0–5% p+Au, d+Au, and ^{3}He+Au central collisions, compared to hydrodynamic calculations using the SONIC model, matched to the same multiplicity as the data. Note that the data points shown include non-flow contributions, whose estimated magnitude is accounted for in the asymmetric systematic uncertainties.

5.3.1 Initial Conditions and Eccentricity

In order to better understand the comparison of the three systems, a deeper understand of the initial conditions is warranted. One critical quantity to characterize the initial collision symmetry is known as the eccentricity. As mentioned in Chapter 2, the second order eccentricity, ε_2, can be calculated from the distribution of the nucleons involved in the initial collision as:

$$\varepsilon_2 = \frac{\sqrt{\langle r^2 \cos(2\phi)\rangle^2 + \langle r^2 \sin(2\phi)\rangle^2}}{\langle r^2 \rangle}, \tag{5.1}$$

where r is the radial nucleon position relative to the centroid of the participants and ϕ is the azimuthal angle of the nucleons [11].

The significance of ε_2 is that v_2 should be proportional to ε_2 if the v_2 is primarily from elliptical flow. Table 5.2 shows ε_2 calculations from the MC Glauber and IP-Glasma models. The ε_2 values can be understood by looking the top three panels of Figure 5.5 which show the spatial distribution of the energy density of the collisions for the p+Au, d+Au, and ^{3}He+Au from left to right. It is note worthy that the eccentricities of d+Au and ^{3}He+Au collisions are largely based on relative nucleon orientation, where as the initial condition of p+Au is solely based on the shape of the lone proton projectile and any fluctuations in the target gold nucleus. Table 5.2 illustrates the uniqueness of the p+Au system by showing the diverging values of ε_2 which can be calculated by IP-Glasma and MC Glauber. Unlike MC Glauber, IP-Glasma generates very circular initial conditions for p+Au, which correspond to very small ε_2 values. For d+Au and ^{3}He+Au, the presence of multiple hot spots wash out differences in single nucleon initial conditions, and thus IP-Glasma and MC-Glauber agree at the 10% level.

While the top three panels of Figure 5.5 are example initial energy density distributions for the three systems, the bottom three panels are the system's energy density distributions after a medium has been formed and time evolved hydrodynamically. For the cases of d+Au and ^{3}He+Au, the initial hot spot orientation is translated into an inverted orientation. This is due to the fact that the medium is produced with the highest energy density at places where the expanding hotspots overlap. The expanding hotspots create a substantial final state elliptical flow with an event plane angle relative to the spatial orientation of the initial hotspots. For example, in the d+Au collision, the event plane vector is transverse to the line that connects the deuteron's nucleons.

Table 5.2: Initial eccentricity ε_2 of small systems at $\sqrt{s} = 200$ GeV for 0–5% centrality from Monte Carlo Glauber initial conditions smeared with a two-dimensional Gaussian of width $\sigma = 0.4$ fm, and IP-Glasma initial conditions.

	p+Au	d+Au	^{3}He+Au
Glauber $\langle\varepsilon_2\rangle$	0.23 ± 0.01	0.54 ± 0.04	0.50 ± 0.02
IP-Glasma $\langle\varepsilon_2\rangle$	0.10 ± 0.02	0.59 ± 0.01	0.55 ± 0.01

Figure 5.6 gives insight into the relation between initial collision eccentricities, as defined in

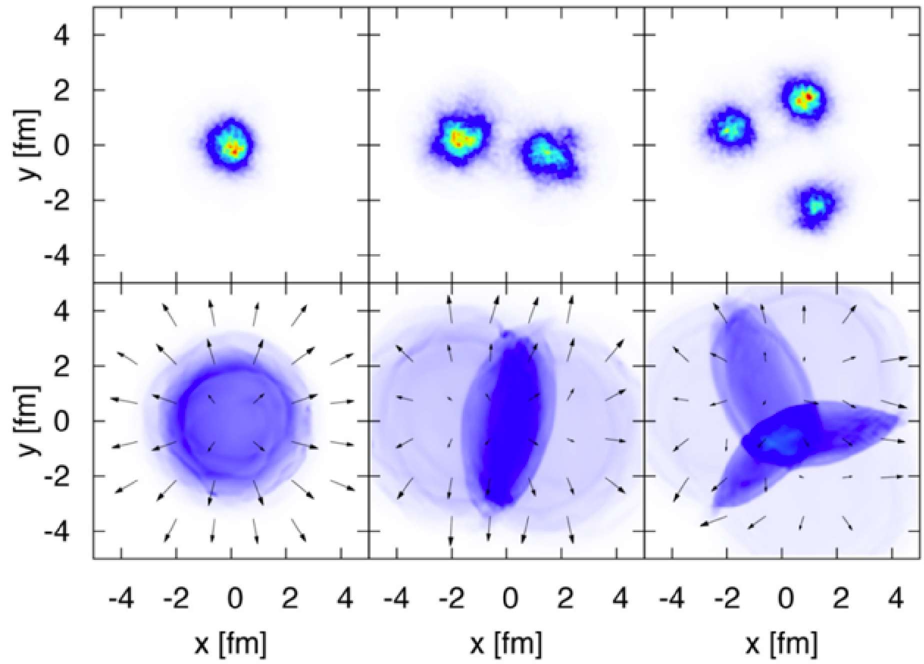

Figure 5.5: The top three panes show the transverse spatial locations of the initial hot spots of the three collision species, p+Au, d+Au, and ^{3}He+Au respetively. The bottom three plots show the resulting medium produced from the overlapping hot spots as well as the resulting particle momentum vector field as calculated from a hydrodynamic model, calculation details in [52]

Equation 5.1, as they are transformed into final state flow. The plot was produced by running many events for p+Au, d+Au, and ^{3}He+Au systems with different initial spatial distribution smearing (i.e. different ε_2). The final freeze-out hyper-surface of each event is then translated into a distribution of hadrons via the Cooper-Frye freeze-out technique [18]. Figure 5.6 shows the pion v_2 at p_T = 1.0 GeV/c divided by ε_2 as a function of ε_2 for each individual p+Au, d+Au, and ^{3}He+Au event. The figure shows a reasonably common scaling of v_2/ε_2 for all three systems with the d+Au and ^{3}He+Au simply extending to larger eccentricities. There are a small set of events with very large ε_2, but have a rather small final v_2. Examination of these events reveals them to be d+Au events where the two hot spots are so far apart that the hydrodynamic fluids never connect during the time evolution, as seen in the overlay in Figure 5.6, in order to produce nearly any elliptic flow. There are fewer ^{3}He+Au in this category, seen where two nucleons are very close and the third is quite far away, again having the same effect.

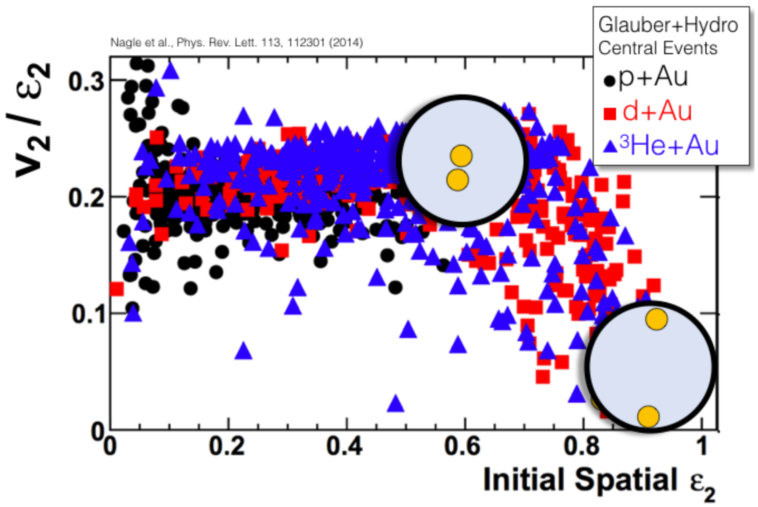

Figure 5.6: v_2/ε_2 versus ε_2 with the flow coefficient for pions evaluated at p_T = 1.0 GeV/c from p+Au, d+Au, and ^{3}He+Au central (b < 2 fm) events (which roughly corresponds to 0–5% centrality). The results are with input parameters η/s = $1/4\pi$ and initial Gaussian smearing σ = 0.4 fm and a freeze-out temperatures of T_F = 150 MeV. Diagrams of two possible d+Au initial configurations are overlayed on top of the plot. Increasing distance between the two d+Au nucleons correspond to a larger ε_2 [40].

To further explore the effect of initial conditions on our v_2 measurement, we divide the v_2 curves by their corresponding ε_2 from Table 5.2, attempting to establish a scaling relation between the two quantities. In ideal ($\eta/s = 0$) hydrodynamics with long livid systems v_2/ε_2 should be independent of ε_2. Figure 5.7 shows that the ratios do not collapse to a common value. As expected, this behavior is also reproduced by the SONIC calculation, because both data and calculation are divided by the same ε_2 values. The lack of scaling in the SONIC calculation can be understood from d+Au events where the neutron and proton from the deuteron projectile are far separated and create two hot spots upon impacting the Au nucleus, as seen in Figure 5.6. These events have a large ε_2, but can result in small v_2 if the two hot spots evolve separately, never combining within the hydrodynamic time evolution. This effect is present in the d+Au and ^{3}He+Au systems, and lowers the average v_2/ε_2 as detailed.

Although, MC Glauber and IP-Glasma are the established models for calculating initial

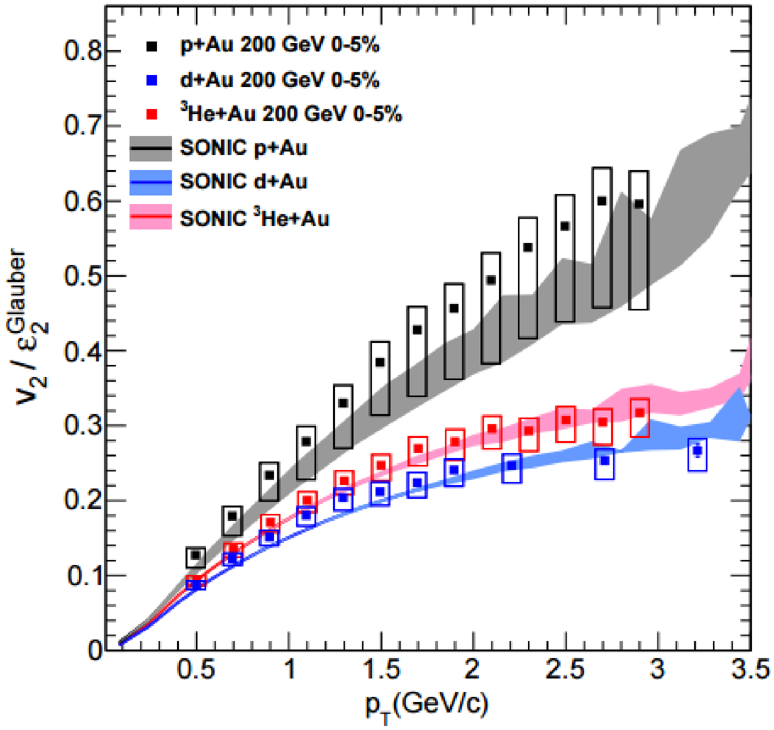

Figure 5.7: v_2 of charged hadrons within $|\eta| < 0.35$ in 0–5% p+Au, d+Au, and ^{3}He+Au central collisions, divided by their corresponding eccentricity ε_2 from Glauber calculations, compared to SONIC calculations of the same quantity. Note that the data points shown include non-flow contributions, whose estimated magnitude is accounted for in the asymmetric systematic uncertainties.

conditions in this context, new models for calculating the initial conditions are promising. A model for initial conditions which incorporates more degrees of freedom by extending the Monte Carlo Glauber approach to also incorporate collisions between constituent quarks, basically increasing the granularity of the simulation [20]. In the rightmost panel of Figure 5.8, the initial eccentricities ε_2 in p+Au, d+Au, and ^{3}He+Au obtained by incorporating constituent quarks, in addition to multiplicity fluctuations, are found to be $\varepsilon_2 = 0.42$, 0.54, and 0.54, respectively. This calculation assumes a Gaussian density distribution of low-x gluons around each constituent quark, of width $\sigma_g = 0.3$ fm. The ε_2 of d+Au and ^{3}He+Au systems show minimal sensitivity to the incorporation of constituent quarks and multiplicity fluctuations. However, p+Au has a substantially larger ε_2 than in the models shown in Table 5.2 when incorporating these effects. Another attempt at the calculation incorporating constituent quarks and multiplicity presents calculations in which case a lower $\varepsilon_2 = 0.34$ is obtained for p+Au [58]. This result shows that when compared to the Glauber ε_2 for p+Au in Table 5.2, quark-level degrees of freedom and multiplicity fluctuations may both play a significant role. In addition to the constituent MC Glauber, it is worth mentioning that an intriguing method for understanding the initial conditions in p+Au comes from fluctuations of the shape of the proton, as described in Ref. [53].

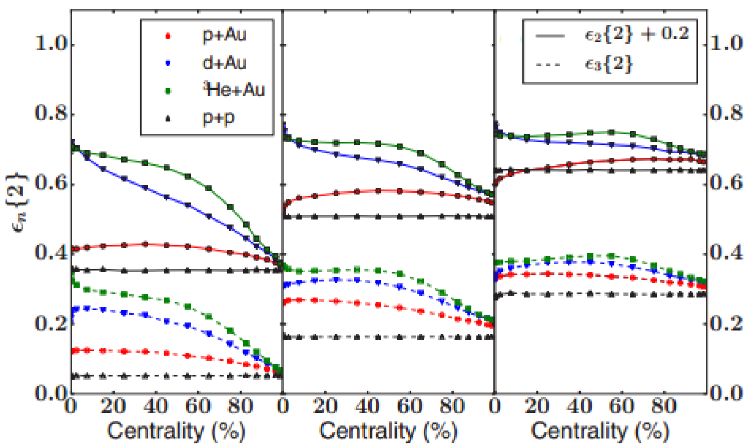

Figure 5.8: Centrality dependence of ε_2 calculated in a variety of small collision systems with a variety of models for collision detection [disklike (left), Gaussian (middle), quark-subdivided nucleons with $\sigma_g = 0.3$ fm (right)] [58].

5.3.2 Comparison to Alternative Models

Although hydrodynamic models like SONIC, which incorporate MC Glauber plus relativistic hydrodynamics, are the standard in which elliptical flow is understood in the field of heavy ions, it is important to test the consistency of other models with our data. Figure 5.9 depicts the measured $v_2(p_T)$ data curves with four different model comparisons. Theoretical predictions are available in the literature, most notably from hydrodynamics with Glauber initial conditions (SONIC [27] and SuperSONIC [49]), hydrodynamics with IP-Glasma initial conditions [52], and A-Multi-Phase-Transport Model (AMPT) [35]. The SuperSONIC model uses the same technique for initial conditions, hydrodynamic expansion, and hadronic cascade as SONIC, yet additionally incorporates pre-equilibrium dynamics with a calculation in the framework of the AdS/CFT correspondence [56].

As mentioned in Chapter 2, calculations using IP-Glasma initial conditions followed by viscous hydrodynamics have been successfully used to describe collectivity in A+A collisions, so it is reasonable to apply IP-Glasma to v_2 in small systems. For the model of IP-Glasma+Hydro, in the case of d+Au and ^{3}He+Au, a better agreement with data can be achieved by increasing the value of η/s or by including a hadronic cascade stage. However, doing so would lower the prediction for p+Au even further. This demonstrates that IP-Glasma does not generate the appropriate initial conditions to account for measured v_2 via hydrodynamic flow.

SONIC and SuperSONIC both agree well with the data of all three systems, although the agreement with the p+Au points only agrees within in the large systematic uncertainty bars. As mentioned above, the agreement of hydrodynamic models supports the idea of initial geometry as the driver of the v_2 signal. Additionally, the three different initial geometries provided by the datasets are useful in constraining the parameters in the SONIC and SuperSONIC models such as η/s, the transition temperature to a hadron cascade, and the Monte Carlo Glauber smearing of nucleon coordinates of $\sigma = 0.4$ fm.

Finally, AMPT, as described in Chapter 2, combines partonic and hadronic scattering in a single model. Central AMPT events with impact parameter $b < 2$ have a midrapidity $dN_{ch}/d\eta$ = 8.1, 14.8, and 20.7 for p+Au, d+Au, and ^{3}He+Au, respectively. AMPT uses the same Monte Carlo Glauber initial conditions used to characterize event geometry as in SONIC or SuperSONIC. However, AMPT makes use of the initial Glauber geometry information to compute v_2 relative to the participant plane [42]. AMPT yields results that agree reasonably well with the data below $p_T \approx 1$ GeV/c, yet under predict them at higher p_T. Although AMPT does not describe the data as well as SONIC, AMPT has successfully been applied to a variety of systems at RHIC and the LHC [37].

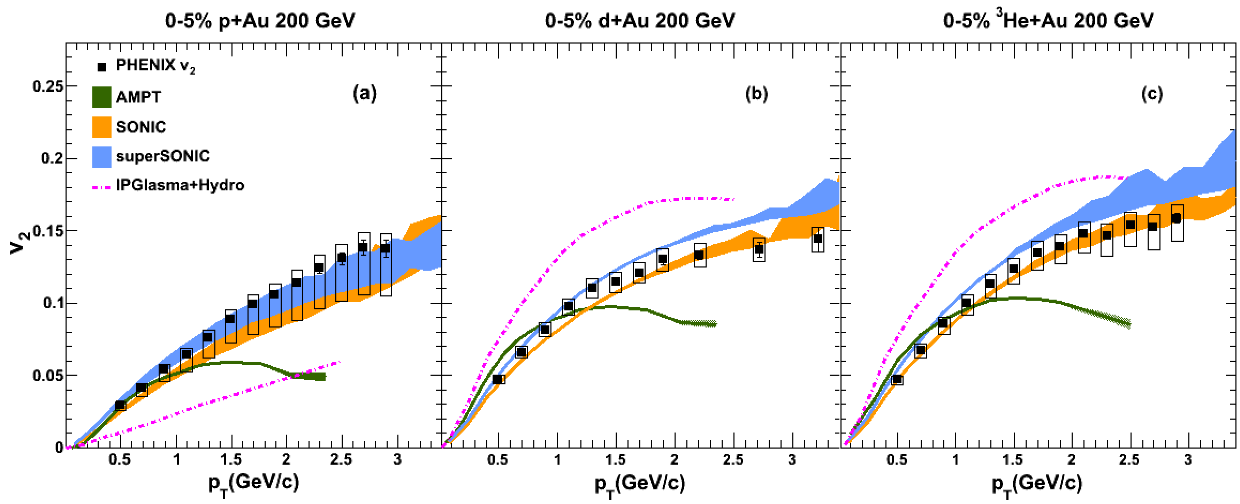

Figure 5.9: Transverse momentum dependence of v_2 in central 0–5% (a) p+Au, (b) d+Au, and (c) ^{3}He+Au collisions at $\sqrt{s_{NN}}$ = 200 GeV. Theoretical calculations from AMPT, SuperSONIC, and IP-Glasma+Hydro are shown in each panel. Note that the data points shown include non-flow contributions, whose estimated magnitude is accounted for in the asymmetric systematic uncertainties.

Chapter 6

Summary and Outlook

In this thesis, we have measured the elliptic flow in 0–5% centrality p+Au collisions at $\sqrt{s_{NN}}$ = 200 GeV. The elliptic flow is quantified by measuring the second-order flow coefficient v_2 defined as:

$$v_2 = \frac{\langle \cos 2(\phi - \Psi_2) \rangle}{\text{Resolution}(\Psi_2)}, \tag{6.1}$$

where ϕ is the azimuthal angle of charged hadrons at mid-rapidity, Ψ_2 is the second-order event plane determined at backwards rapidity (Au-going direction), and Resolution(Ψ_2) is the event plane resolution. This procedure is detailed in Chapter 4, Section 4.2.1.

The measurement of $v_2(p_T)$, as a function of transverse momentum, in 0–5% centrality p+Au at $\sqrt{s_{NN}}$ = 200 GeV collisions completes a set of measurements with engineered initial geometries at RHIC, including the p+Au, d+Au, and ^{3}He+Au as shown in Figure 6.1. Sources of systematic uncertainty have been described in detail in Chapter 4, Section 4.5, with the non-flow being the dominant source of systematic uncertainty. The measured $v_2(p_T)$ in p+Au at $\sqrt{s_{NN}}$ = 200 GeV is in agreement with Monte Carlo Glauber initial conditions plus relativistic hydrodynamics (SONIC), as also shown in Figure 6.1. The agreement of v_2 with a hydrodynamic model is an indication that the initial state geometry becomes transformed into a final state momentum anisotropy in 0–5% p+Au at $\sqrt{s_{NN}}$ = 200 GeV collisions.

In order to properly compare the v_2 of p+Au, d+Au, and ^{3}He+Au at $\sqrt{s_{NN}}$ = 200 GeV for each system, we have compared the average second-order eccentricity ε_2 of the initial collision, as defined in Chapter 5, Section 5.3.1. If the measured v_2 is primarily from hydrodynamic flow, i.e.

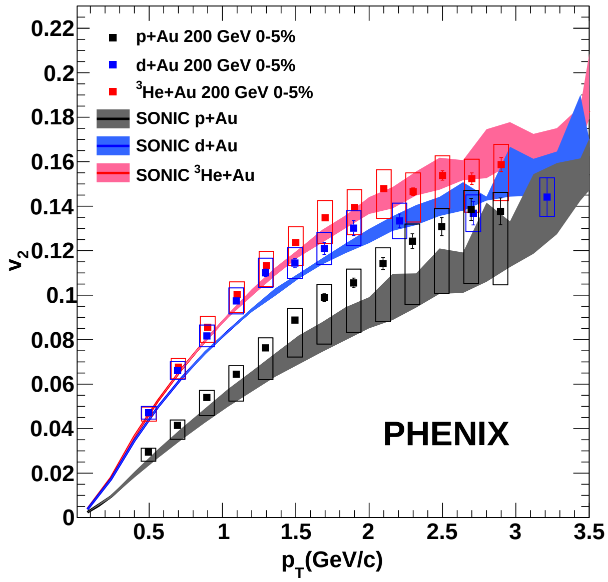

Figure 6.1: v_2 of charged hadrons within $|\eta| < 0.35$ in 0–5% centrality p+Au, d+Au, and ^{3}He+Au at $\sqrt{s_{NN}} = 200$ GeV, compared with hydrodynamic calculations using the SONIC model, matched to the same multiplicity as the data [28].

minimal levels of non-flow, then $v_2 \propto \varepsilon_2$. Thus, the Monte Carlo Glauber ε_2 for p+Au, d+Au, and ^{3}He+Au being 0.23, 0.54, and 0.50, respectively, implies the ordering of v_2 of the three systems should be $v_2^{d+\mathrm{Au}} \approx v_2^{^3\mathrm{He+Au}} > v_2^{p+\mathrm{Au}}$, which is what is observed in Figure 6.1.

Future work is being done in analyzing small collision systems recently run (in 2016) at RHIC: d+Au at $\sqrt{s_{NN}} = 200$, 62, 39, and 20 GeV. By measuring the elliptic flow in this d+Au beam energy scan, information on the effect of varying the initial temperature and the lifetime of the medium can be obtained. It is noteworthy that even at low $\sqrt{s_{NN}}$ for d+Au collisions, hydrodynamic simulations predict that the space-time volume of QGP is not negligible, as shown in Figure 6.2 [34]. In fact, the calculated space-time volume of the medium at $\sqrt{s_{NN}} = 20$ GeV is roughly half of the calculated space-time volume for $\sqrt{s_{NN}} = 200$ GeV, indicating that there is a reasonable expectation to see some evidence of a QGP medium forming in d+Au collisions event at $\sqrt{s_{NN}} = 20$ GeV.

Predications have been made of the v_2 for the various energies of the d+Au beam energy

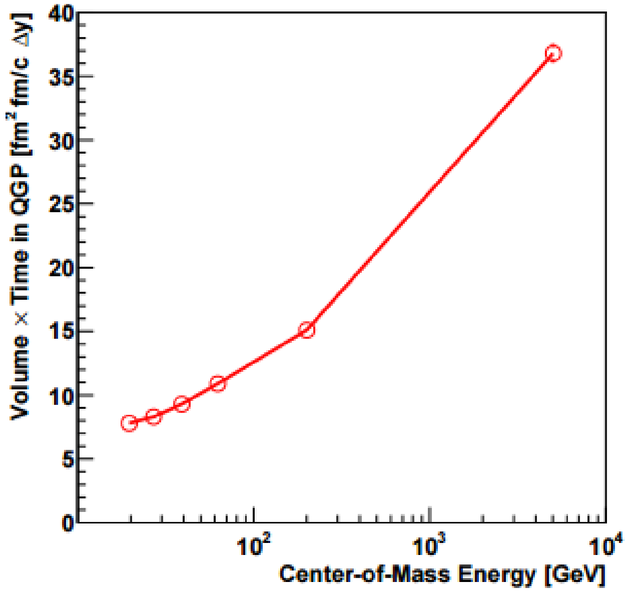

Figure 6.2: The total space-time volume as a function of $\sqrt{s_{NN}}$ in heavy ion collisions calculated by a hydrodynamic model [34].

scan by using the SONIC, superSONIC, and AMPT models; these models are described in Chapter 2. Figure 6.3 shows predictions for v_2 in the four different energy collsions. The SONIC and superSONIC models (the hydrodynamic models) both predict that there will be a sizable v_2 at all $\sqrt{s_{NN}}$ systems and that the v_2 will have a positive $\sqrt{s_{NN}}$ dependence across all p_T. AMPT, a non-hydrodynamic model, predicts a similarly large v_2 across the different energies with only a modest $\sqrt{s_{NN}}$ dependence for $p_T \approx 1.0$ GeV/c and less. The differences between the SONIC and superSONIC v_2 and the AMPT v_2 at $p_T > 1.0$ GeV/c is further explored in Ref. [34]. The future measurement of elliptic flow in the d+Au beam energy scan datasets, along with the measurement of the completion of the set of three measurements made in this thesis, furthers our understanding of the phenomena of QGP in small collision systems.

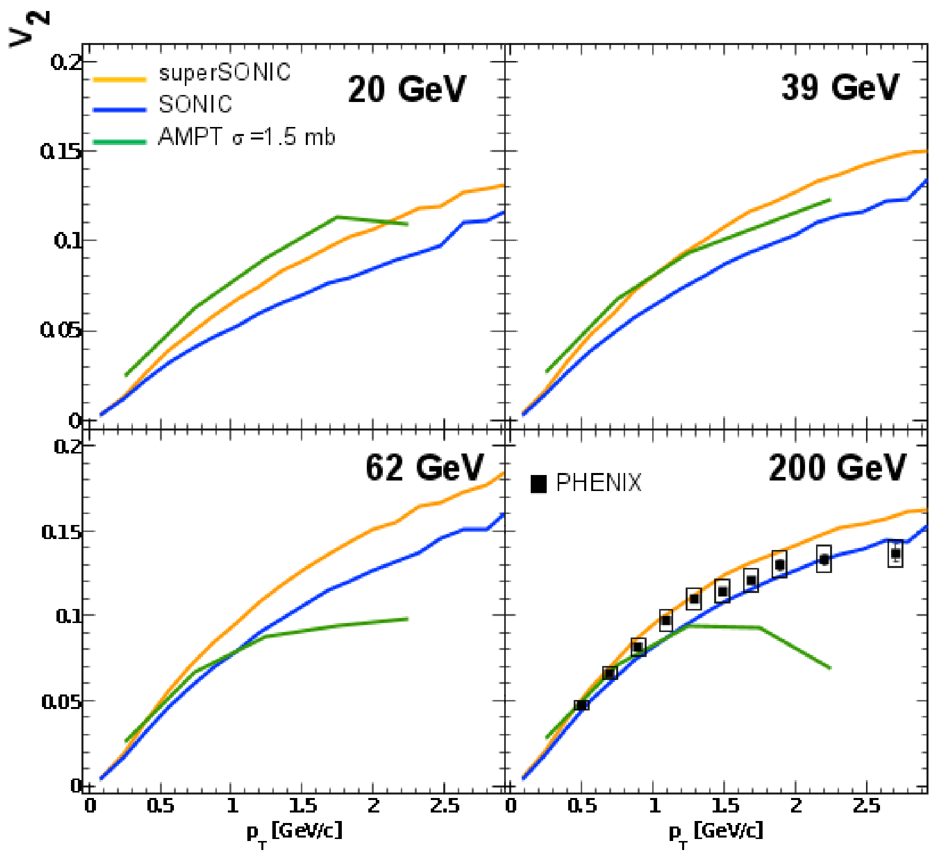

Figure 6.3: Calculations of $v_2(p_T)$ d+Au events at various $\sqrt{s_{NN}}$ (given on the upper right of each panel) for AMPT, SONIC, and SuperSONIC models. Note that there are data points in the lower right panel due to the fact that the v_2 in d+Au at $\sqrt{s_{NN}} = 200$ GeV has been measured previously by PHENIX from data taken in 2008 [34].

Bibliography

[1] Event reconstruction in the {PHENIX} central arm spectrometers. Nucl.Instrum.Meth, A482:491–512, 2002.

[2] Rhic operations with asymmetric collisions in 2015. 2015.

[3] Roel Aaij et al. Observation of $J/\psi p$ Resonances Consistent with Pentaquark States in $\Lambda_b^0 \to J/\psi K^- p$ Decays. Phys. Rev. Lett., 115:072001, 2015.

[4] K. Aamodt and et al. Harmonic decomposition of two particle angular correlations in pbpb collisions at. Physics Letters B, 708(35):249 – 264, 2012.

[5] F. D. et al Aaron. Inclusive deep inelastic scattering at high q2 with longitudinally polarised lepton beams at hera. Journal of High Energy Physics, 2012(9):61, 2012.

[6] A. Adare and et al. Centrality categorization for $R_{p(d)+A}$ in high-energy collisions. Phys. Rev. C, 90:034902, Sep 2014.

[7] A. Adare and et al. Transverse energy production and charged-particle multiplicity at midrapidity in various systems from $\sqrt{s_{NN}} = 7.7$ to 200 gev. Phys. Rev. C, 93:024901, Feb 2016.

[8] A. et al Adare. Measurements of elliptic and triangular flow in high-multiplicity ^{3}He + Au collisions at $\sqrt{s_{NN}} = 200$ GeV. Phys. Rev. Lett., 115:142301, Sep 2015.

[9] S. S. et al Adler. Absence of suppression in particle production at large transverse momentum in $\sqrt{s_{NN}} = 200$ GeV $d+$Au collisions. Phys. Rev. Lett., 91:072303, Aug 2003.

[10] M. Aizawa, Y. Akiba, R. Begay, J. Burward-Hoy, R.B. Chappell, C.Y. Chi, M. Chiu, T. Chujo, D.W. Crook, A. Danmura, K. Ebisu, M.S. Emery, K. Enosawa, S. Esumi, J. Ferrierra, A.D. Frawley, V. Griffin, H. Hamagaki, H. Hara, R.S. Hayano, H. Hayashi, T.K. Hemmick, M. Hibino, R. Higuchi, T. Hirano, R. Hoade, R. Hutter, M. Inaba, K. Jones, S. Kametani, S. Kato, M. Kennedy, J. Kikuchi, A. Kiyomichi, K. Koseki, M. Kurata-Nishimura, K. Kurita, Y. Kuroki, T. Matsumoto, Y. Miake, Y. Miyamoto, G.G. Moscone, Y. Nagasaka, S. Nishimura, M. Ono, K. Oyama, R. Raynis, T. Sakaguchi, S. Sakai, H. Sako, S. Salomone, S. Sato, K. Shigaki, T. Shimada, M. Suzuki-Nara, M. Tamai, Y. Tanaka, H. Tsuruoka, S. Urasawa, T. Ushiroda, J.W. Walker, S. Wang, A.L. Wintenberg, L.W. Wright, K. Yagi, Y. Yokota, and G.R. Young. {PHENIX} central arm particle {ID} detectors. Nuclear Instruments and Methods in Physics Research Section A: Accelerators, Spectrometers, Detectors and Associated Equipment, 499(23):508 – 520, 2003. The Relativistic Heavy Ion Collider Project: {RHIC} and its Detectors.

[11] Yasuyuki Akiba et al. The Hot QCD White Paper: Exploring the Phases of QCD at RHIC and the LHC. 2015.

[12] B. Alver and G. Roland. Collision-geometry fluctuations and triangular flow in heavy-ion collisions. Phys. Rev. C, 81:054905, May 2010.

[13] S.H. Aronson and et al. {PHENIX} magnet system. Nuclear Instruments and Methods in Physics Research Section A: Accelerators, Spectrometers, Detectors and Associated Equipment, 499(23):480 – 488, 2003. The Relativistic Heavy Ion Collider Project: {RHIC} and its Detectors.

[14] Eric Michael Belmont. Elliptic flow at forward rapidity in $\sqrt{s_{NN}} = 200$ GeV Au+Au collisions. PhD thesis, Vanderbelt, 2012.

[15] J. et al Beringer. Review of particle physics. Phys. Rev. D, 86:010001, Jul 2012.

[16] Siegfried Bethke. The 2009 world average of α. The European Physical Journal C, 64(4):689–703, 2009.

[17] Rajeev S. Bhalerao. Relativistic heavy-ion collisions. In Proceedings, 1st Asia-Europe-Pacific School of High-Energy Physics (AEPSHEP): Fukuoka, Japan, October pages 219–239, 2014.

[18] S.M. Bilenky and J. Hoek. Glashow-weinberg-salam theory of electroweak interactions and the neutral currents. Physics Reports, 90(2):73 – 157, 1982.

[19] Adam Bzdak and Guo-Liang Ma. Elliptic and triangular flow in p-pb and peripheral pb-pb collisions from parton scatterings. Phys. Rev. Lett., 113:252301, Dec 2014.

[20] M. Cheng, S. Ejiri, P. Hegde, F. Karsch, O. Kaczmarek, E. Laermann, R. D. Mawhinney, C. Miao, S. Mukherjee, P. Petreczky, C. Schmidt, and W. Soeldner. Equation of state for physical quark masses. Phys. Rev. D, 81:054504, Mar 2010.

[21] Fred Cooper and Graham Frye. Single-particle distribution in the hydrodynamic and statistical thermodynamic models of multiparticle production. Phys. Rev. D, 10:186–189, Jul 1974.

[22] Kevin Dusling and Raju Venugopalan. Azimuthal collimation of long range rapidity correlations by strong color fields in high multiplicity hadron-hadron collisions. Phys. Rev. Lett., 108:262001, Jun 2012.

[23] S. Eremin and S. Voloshin. Nucleon participants or quark participants? Phys. Rev. C, 67:064905, Jun 2003.

[24] C. Aidala et al. The {PHENIX} forward silicon vertex detector. Nuclear Instruments and Methods in Physics Research Section A: Accelerators, Spectrometers, Detectors and Associated Equipment, 755:44 – 61, 2014.

[25] K. Adcox et al. {PHENIX} detector overview. Nuclear Instruments and Methods in Physics Research Section A: Accelerators, Spectrometers, Detectors and Associated Equipment, 499(2?3):469 – 479, 2003. The Relativistic Heavy Ion Collider Project: {RHIC} and its Detectors.

[26] A Fedotov. Progress of high-energy electron cooling for rhic. 2007.

[27] Enrico Fermi. High energy nuclear events. Progress of Theoretical Physics, 5(4):570–583, 1950.

[28] A. D. Frawley. Cold Nuclear Matter Effects and Heavy Quark Production in PHENIX. Nucl. Phys., A910-911:123–130, 2013.

[29] Charles Gale, Sangyong Jeon, Björn Schenke, Prithwish Tribedy, and Raju Venugopalan. Event-by-event anisotropic flow in heavy-ion collisions from combined yang-mills and viscous fluid dynamics. Phys. Rev. Lett., 110:012302, Jan 2013.

[30] M. Habich, J. L. Nagle, and P. Romatschke. Particle spectra and hbt radii for simulated central nuclear collisions of. The European Physical Journal C, 75(1):15, 2015.

[31] M. Habich, J. L. Nagle, and P. Romatschke. Particle spectra and hbt radii for simulated central nuclear collisions of c+c, al+al, cu+cu, au+au, and pb+pb from sqrt(s)=62.4-2760 gev. The European Physical Journal C, 75(1):15, 2015.

[32] Ulrich W. Heinz. Towards the Little Bang Standard Model. J. Phys. Conf. Ser., 455:012044, 2013.

[33] Tetsufumi Hirano, Ulrich Heinz, Dmitri Kharzeev, Roy Lacey, and Yasushi Nara. Mass ordering of differential elliptic flow and its violation for ϕ mesons. Phys. Rev. C, 77:044909, Apr 2008.

[34] V. Khachatryan and et al. Evidence for collectivity in pp collisions at the {LHC}. Physics Letters B, 765:193 – 220, 2017.

[35] V. Khachatryan and etal. Observation of long-range, near-side angular correlations in proton-proton collisions at the lhc. Journal of High Energy Physics, 2010(9):91, 2010.

[36] Peter F. Kolb and Ulrich W. Heinz. Hydrodynamic description of ultrarelativistic heavy ion collisions. 2003.

[37] J. D. Orjuela Koop, R. Belmont, P. Yin, and J. L. Nagle. Exploring the beam-energy dependence of flow-like signatures in small-system $d+\mathrm{Au}$ collisions. Phys. Rev. C, 93:044910, Apr 2016.

[38] Zi-Wei Lin, Che Ming Ko, Bao-An Li, Bin Zhang, and Subrata Pal. Multiphase transport model for relativistic heavy ion collisions. Phys. Rev. C, 72:064901, Dec 2005.

[39] Matthew Luzum and Paul Romatschke. Conformal relativistic viscous hydrodynamics: Applications to rhic results at $\sqrt{s_{NN}} = 200$ gev. Phys. Rev. C, 78:034915, Sep 2008.

[40] Guo-Liang Ma and Zi-Wei Lin. Predictions for $\sqrt{s_{NN}} = 5.02$ tev pb + pb collisions from a multiphase transport model. Phys. Rev. C, 93:054911, May 2016.

[41] Stephen J. Sanders Michael L. Miller, Klaus Reygers and Peter Steinberg. Glauber modeling in high-energy nuclear collisions. Annual Review of Nuclear and Particle Science, 57:205–243, 2007.

[42] J. Scott Moreland, Jonah E. Bernhard, and Steffen A. Bass. Alternative ansatz to wounded nucleon and binary collision scaling in high-energy nuclear collisions. Phys. Rev. C, 92:011901, Jul 2015.

[43] J. L. Nagle, A. Adare, S. Beckman, T. Koblesky, J. Orjuela Koop, D. McGlinchey, P. Romatschke, J. Carlson, J. E. Lynn, and M. McCumber. Exploiting intrinsic triangular geometry in relativistic ^{3}He + Au collisions to disentangle medium properties. Phys. Rev. Lett., 113:112301, Sep 2014.

[44] Jean-Yves Ollitrault, Arthur M. Poskanzer, and Sergei A. Voloshin. Effect of flow fluctuations and nonflow on elliptic flow methods. Phys. Rev. C, 80:014904, Jul 2009.

[45] J. D. Orjuela Koop, A. Adare, D. McGlinchey, and J. L. Nagle. Azimuthal anisotropy relative to the participant plane from a multiphase transport model in central $p+$Au, $d+$Au, and ^{3}He$+$ Au collisions at $\sqrt{s_{NN}} = 200$ gev. Phys. Rev. C, 92:054903, Nov 2015.

[46] A. Ortiz Velasquez, P. Christiansen, E. Cuautle Flores, I. A. Maldonado Cervantes, and G. Paić. Color reconnection and flowlike patterns in *pp* collisions. Phys. Rev. Lett., 111:042001, Jul 2013.

[47] A. M. Poskanzer and S. A. Voloshin. Methods for analyzing anisotropic flow in relativistic nuclear collisions. Phys. Rev. C, 58:1671–1678, Sep 1998.

[48] Guang-You Qin. Anisotropic Flow and Jet Quenching in Relativistic Nuclear Collisions. Int. J. Mod. Phys., E24(02):1530001, 2015.

[49] Johann Rafelski. Connecting qgp-heavy ion physics to the early universe. Nuclear Physics B - Proceedings Supplements, 243:155 – 162, 2013.

[50] Johann Rafelski and Jeremiah Birrell. Traveling through the universe: Back in time to the quark-gluon plasma era. Journal of Physics: Conference Series, 509(1):012014, 2014.

[51] Eric Michael Richardson. Elliptic flow at forward rapidity in $\sqrt{s_{NN}} = 200$ GeV Au+Au collisions. PhD thesis, Maryland U., 2012.

[52] P. Romatschke. Light-heavy-ion collisions: a window into pre-equilibrium qcd dynamics? The European Physical Journal C, 75(7):305, 2015.

[53] T. Roser. Rhic performance. Nuclear Physics A, 698(1):23 – 28, 2002.

[54] Helmut Satz. The quark-gluon plasma a short introduction. Nuclear Physics A, 862:4 – 12, 2011.

[55] Björn Schenke, Prithwish Tribedy, and Raju Venugopalan. Fluctuating glasma initial conditions and flow in heavy ion collisions. Phys. Rev. Lett., 108:252301, Jun 2012.

[56] Bjrn Schenke and Raju Venugopalan. Collective effects in lightheavy ion collisions. Nuclear Physics A, 931:1039 – 1044, 2014. {QUARK} {MATTER} 2014XXIV {INTERNATIONAL} {CONFERENCE} {ON} {ULTRARELATIVISTIC} NUCLEUS-NUCLEUS {COLLISIONS}.

[57] Sren Schlichting and Bjrn Schenke. The shape of the proton at high energies. Physics Letters B, 739:313 – 319, 2014.

[58] Huichao Song. Hydrodynamic modelling for relativistic heavy-ion collisions at rhic and lhc. Pramana, 84(5):703–715, 2015.

[59] M. J. Tannenbaum. Highlights from BNL-RHIC. Subnucl. Ser., 50:347–367, 2014.

[60] Wilke van der Schee, Paul Romatschke, and Scott Pratt. Fully dynamical simulation of central nuclear collisions. Phys. Rev. Lett., 111:222302, Nov 2013.

[61] S. Voloshin and Y. Zhang. Flow study in relativistic nuclear collisions by fourier expansion of azimuthal particle distributions. Zeitschrift für Physik C Particles and Fields, 70(4):665–671, 1996.

[62] Kevin Welsh, Jordan Singer, and Ulrich Heinz. Initial-state fluctuations in collisions between light and heavy ions. Phys. Rev. C, 94:024919, Aug 2016.

[63] XIAO-MING XU. ORIGIN OF TEMPERATURE OF QUARK-GLUON PLASMA IN HEAVY ION COLLISIONS, pages 203–208. WORLD SCIENTIFIC, 2015.